Stony Brook University

Self-Organization of heteroepitaxial islands during crystal growth

A Dissertation Presented

by

Gajendra Pandey

to

The Graduate School

in Partial fulfillment of the

Requirements

for the Degree of

Doctor of Philosophy

in

Mechanical Engineering

Stony Brook University

December 2007

Stony Brook University

The Graduate School

Gajendra Pandey

We, the dissertation committee for the above candidate for the
Doctor of Philosophy degree,
hereby recommend acceptance of this dissertation.

Dr. Robert V. Kukta – Dissertation Advisor
Associate Professor, Mechanical Engineering

Dr. Chad S. Korach – Chairperson of defense
Assistant Professor, Mechanical Engineering

Dr. Imin Kao
Professor, Mechanical Engineering

Dr. Richard Gambino
Professor, Material Science and Engineering

This dissertation is accepted by the Graduate School.

Lawrence Martin
Dean of the Graduate School

Abstract of the Dissertation

Self-Organization of heteroepitaxial islands during crystal growth

by

Gajendra Pandey
Doctor of Philosophy

in

Mechanical Engineering
Stony Brook University
2007

Fabrication of regular nanostructures has been investigated for over a decade with modest progress. Although there are varieties of methods for fabricating nanostructures but very few of them are cost effective and less time consuming. One of the commonly used methods is to use the concept of self-organization which has drawn the attention of researchers over the past few years. The present work is focused on the fabrication of nanostructures by using self-organization for the arrangement of strained epitaxial islands deposited over a substrate. In isotropic conditions and on a defect free substrate, deposited islands repel each other and the results in the formation of hexagonal domains which meet at defects. The goal is to use the anisotropy to organize the islands such that the defects developed in the isotropic case are reduced. The focus is on in-plane anisotropies in surface stress and lattice mismatch between the film and substrate materials. Starting from a configuration where island sizes and position are random, evolution towards equilibrium through mass transport via condensation/evaporation is simulated. An efficient numerical method is obtained by reducing a model of square monolayer islands of finite size to point dipoles that interact through their elastic fields. Models for both the kinetics and energetics of the system are obtained by this reduction. It is found that the point source model is accurate for island separations larger than about 3 times the width of an island. Anisotropy introduces orientational preferences which enhance organization in cases of modest anisotropy and cause islands to form into zigzagged lines in cases of high anisotropy. To get control over the position of islands some defects in the form of dislocations are introduced into the substrate. It is found that the dislocations field modulates the elastic field of the system and hence induces the preferred locations for islands. The effect of selective area epitaxy is also studied. A square-shaped region was selected in this work. The islands interact with the elastic field of other islands and with itself and arrange into low energy or stable configuration. Through this analysis some preferred positions of islands is obtained.

Contents

List of Figures

ACKNOWLEDGEMENTS

I would like to express my deep sense of gratitude to my ever-cherished advisor Dr. Robert V. Kukta for his invaluable guidance and help throughout my PhD.

I cannot forget to thank my colleague Noah Machtay for his cooperation. I also wish to thank my friends Prashant Jha, Smarat Chadwa, Pranav Nawani, Anand Kashyap, Shashank Shrivastava and Ayush Jha who made my stay at Stony Brook a pleasant memory.

Finally I would like to express my gratitude to my parents, my wife and my dear brother who always encouraged me and cooperated with me at all stages of my life.

Gajendra Pandey

Chapter 1

Introduction

Self-assembly is a widely researched phenomenon for fabricating nano-scale devices. The idea behind this approach is to allow physical processes to spontaneously build a device. A particular form of self-assembly that is suitable for electronic and optoelectronic devices occurs when one crystalline material is deposited epitaxially onto another. Growth occurs epitaxially when the deposited material uses the lattice of the substrate as a template for growth, thus achieving a coherent interface between the two materials. In the case of a lattice mismatch between the film and the substrate materials, the constraint of epitaxy gives rise to residual stress. It is this stress that drives self-assembly in these systems. The basic self-assembled unit is a cluster of atoms on the substrate, called an island. Islands serve as building blocks for larger devices. For example, islands of uniform size and random position can be used in optical devices while systems with greater uniformity in island size as well as position are required for many applications in the electronics industry. Other devices require islands in a specific configuration, such as a square cell with islands at the corners for use in quantum dot cellular automata. The main challenge here is to obtain islands or quantum dots of desired size and organization. There are various methods available for positioning quantum dots. Some researched methods include the manipulation of surface stress, elastic

anisotropies, or defects to guide organization. Positioning of quantum dots can also be controlled by introducing a pattern onto the substrate by using lithography and ion-etching. The current investigation focuses on such methods for the organization of epitaxial islands grown on a substrate.

1.1 Fabrication processes of nanostructures

The ongoing trend towards miniaturization has resulted in the development of novel devices with exceptional characteristics and has established a large research effort towards further miniaturization and, in particular, for the development of reliable and cost-effective techniques to fabricate nanoscale structures. The quest for miniaturization has lead to tools such as the atomic force microscope (AFM) and the scanning tunneling microscope (STM). Combined with well-established fabrication processes such as electron beam lithography, these instruments allow us to deliberately manipulate and manufacture nanostructures on solid surface [1–3]. To provide the necessary background for understanding novel fabrication methods through self-assembly, direct methods for micro-and nano-fabrication are first discussed.

1.1.1 Direct methods for fabrication of nanostructures

In the fabrication process of nanostructures using lithography (as shown schematically in Figure 1.1), a resist film, polymethylmethacrylate (PMMA), is first spun onto a substrate (typically silicon). A high resolution electron beam lithography system is used to expose patterns in the PMMA. The exposed PMMA is developed in a cellosolve and methanol solution to form a resist template on the substrate. The PMMA template is then used to selectively etch nanostructures into the substrate. Besides etching, pattern can also be formed using either a lift-off or electroplating process. In a lift-off process, a metal film is first deposited onto the entire sample. The sample is then im-

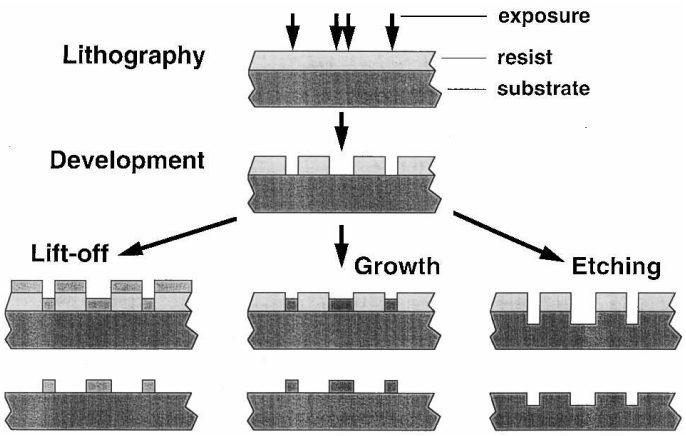

Figure 1.1: Schematic of a typical process for fabricating nanostructures using ut and related technologies reproduced from Chou *et al* [1].

mersed in acetone that dissolves the PMMA template and lifts off the metal on the PMMA surface, but not the metal on the substrate. In an electroplating process, a thin metal plating base is placed between the PMMA and the substrate, and the PMMA template is removed after plating.

Drodofsky *et al* [2] generated various two-dimensional patterns by using a technique called atom lithography. In atom lithography, nanometer-scale structures are generated on a surface by using optical elements for neutral atomic beams. In contrast to conventional fabrication methods, where a resist is exposed to radiation of charged particles or photons, atom lithography directly deposits the structure on the surface. With optical lithography, the resolution is limited by the wavelength of the light due to diffraction, however atom lithography has a potentially higher resolution as atoms with thermal kinetic energy typically have a de Broglie wavelength in the picometer range. Unfortunately, this method takes an exceptionally long time due to its serial nature.

A parallel technique is interference lithography. Nguyen *et al* [4] demonstrated interference lithography to fabricate large-area, two-dimensional arrays

of identical submicron metallic wires with high aspect ratios. These nanowire arrays are grown by electrodeposition into nanochannel glass (NCG). They controlled the geometric patterns and packing densities of the NCG-based arrays as well as the shapes, sizes, and aspect ratios of the individual wires to a high degree. Using NCG templates they have also fabricated metallic nanotubes by electroplating and electroless deposition onto the glass walls of the channels in the nanochannel glass wafers. Though the parallel lithography techniques takes shorter time than serial lithography technique but they still take exceptionally long time to fabricate the nanostructure.

The drawback of lithography techniques can be overcome by using a nanoimprinting technique, wherein a nano-patterned mold (fabricated via electron beam lithography) is pressed into a polymer film to transfer the nanostructures onto the substrate [5]. In the fabrication process used by Chou *et al* [5] a mold is pressed into a thin thermoplastic polymer film on a substrate that is heated above its glass transition temperature. Above that temperature the polymer behaves as a viscous liquid and can flow under a pressure, thereby conforming to the mold. The mold can be made of metals, dielectrics, or semiconductors. Figure 1.2 shows the SEM image of 25 nm diameter dots with a 120 nm period imprinted into a PMMA film. Chou and Krauss [6] have also fabricated nanoscale photodetectors, silicon quantum-dot, quantum-wire, and ring transistors by using nanoimprint lithography and have demonstrated structures on the order of 10 nm with vertical and smooth sidewalls. Though this process takes less time than lithographic methods, it is very expensive and the feature size imprinted is limited by the mold size. Clearly this method cannot be used to fabricate the mold. Another technique such as one previously discussed could be used. The cost of the mold is directly related to the cost of the fabrication process. Hence for this technique to be viable, a low cost method would be necessary for making molds, as molds with nanoscale fea-

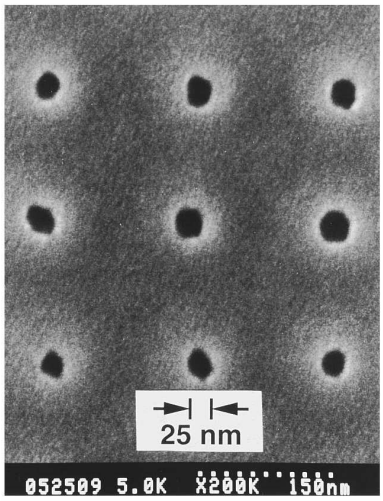

Figure 1.2: SEM micrograph by Chou *et al* [5]. A dot pattern imprinted into PMMA. The dots have a 25 nm diameter and 120 nm period.

tures would be prone to undergo morphology transformations, fracture, and other types of failure.

Another method to create nanostructures on a surface is based on modern scanning probe microscopy (SPM). In this technique nanostructures down to an atomic scale are achieved by using the SPM tip as a stylus to "write" nanoscale structures. Kent *et al* [7] investigated the growth of nanometer-scale iron deposits with a combination of Chemical Vapor Deposition (CVD) and STM techniques. They controlled depositions on either the substrate or the tip by varying the growth conditions and produced high aspect ratio iron filaments with diameters less than 10 nm and aspect ratios greater than 80. They also showed that either the amorphous or the crystalline material can be formed by varying the bias condition and precursor pressure. In their experiments, filaments are directly deposited on the apex of a silicon tip, which is part of a microfabricated silicon cantilever used in scanning force microscopy. Extensive work has been done over the last decade to develop nanostructures of different material combinations using this technique. Though this tech-

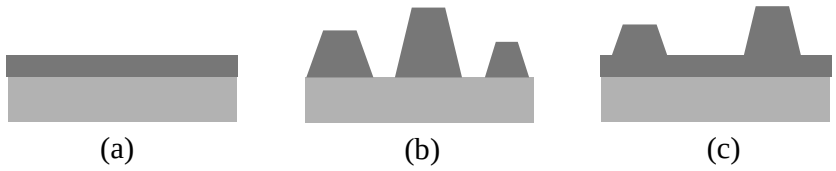

Figure 1.3: Classification of heteroepitaxial growth: (a) layer-by-layer growth (Frank-van der Merwe), (b) island growth (Volmer-Weber) and (c) layer-plus-island growth (Stranski-Krastanov).

nique is less expensive than other techniques, it is time consuming because of its serial nature.

1.1.2 Fabrication of nanostructures via self-assembly

An alternative to the above direct methods of fabricating nanoscale structures is to manipulate natural processes in order to self-assemble a device. Consider a film deposited epitaxially onto a substrate. In certain material systems, the film grows as isolated material clusters or quantum dots. If properly arranged these dots could be used to form a device or part of a device. Quantum dot arrays have gained widespread interest because of their application in electronic and optoelectronic devices.

An epitaxial film may grow in one of three different growth modes depending on various factors including temperature, deposition rate, the presence of impurities, the lattice-mismatch, and the interfacial energies. The growth modes are illustrated in Figure 1.3. They are Frank-van der Merve, wherein the film grows atomic layer by atomic layer, Volmer-Weber, wherein the film grows as islands directly atop the substrate, and Stranski-Krastanov, wherein layer-by-layer growth occurs for several monolayers to wet the substrate, followed by three-dimensional islands atop the wetting layer.

In lattice-matched systems, the growth mode is primarily governed by the interface and surface energies. If the sum of the film surface energy γ_f

and the interface energy γ_{fs} is lower than the energy of the substrate surface, $\gamma_f + \gamma_{fs} < \gamma_s$, the deposited material wets the substrate and there is no driving force for islands to form (the Frank-van der Merwe growth mode). If the wetting criterion is not satisfied then the flat wetting layer has a high energy cost and is not energetically favorable; the deposited material will agglomerate directly into islands (Volmer-Weber growth) [8].

If there is a difference in lattice constant between the film and the substrate materials then the system will be under strain due to the constraint of epitaxy. Strain plays an important role in determining the growth mode. In a lattice-mismatched system, the epitaxial film grows with a lattice spacing that is commensurate with that of the substrate. If the substrate surface is flat, a thin film of uniform thickness would be strained by the amount $\epsilon_0 = (a_s - a_f)/a_f$ where a_s and a_f are respectively the lattice spacings of the substrate and the undeformed film. For example at a temperature of 500^0C a uniform Ge thin film ($a_f = 5.66$Å) on a Si substrate ($a_s = 5.433$Å) would have a compressive strain of 4.2%. The strain energy of an islanded morphology is always lower than that of a flat strained film of the same volume. When the wetting criterion is satisfied, the surface energy of a flat film is lower than that of islanded morphology. The strain energy promotes island growth while the surface energy favors layer-by-layer growth. There is a competition between these two energy contributions. The deposited film material first grows in layer-by-layer fashion to reduce the surface energy. This also results in an increase in strain energy. After a certain critical film thickness is reached, the increase in strain energy exceeds the decrease in surface energy and a planar film becomes morphologically unstable. This instability increases in amplitude, eventually resulting in the formation of isolated islands or nanocrystals on the substrate, wherein strain is relaxed. Thus the SK growth mode occurs.

The method of pattern formation by self-organization offers less control

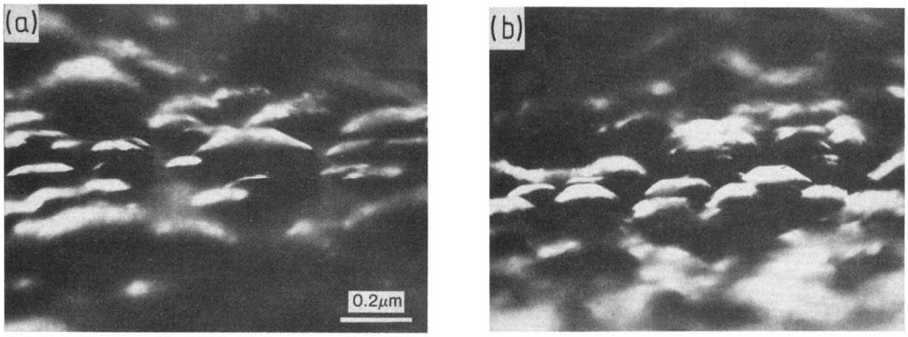

Figure 1.4: Reflection electron micrographs of Ge clusters on Si(111) carried out by Zinke *et al*: (a) after deposition of 9 ML of Ge at room temperature and post-deposit annealing for 10 min to 925 K; (b) after deposition of 13.8 ML during 40 min at 815 K sample temperature [9].

than direct methods over size, shape and organization of nanostructures, but if these issues can be overcome, self-organization will be a viable and very cost-effective process. Extensive work has been done to control the size, shape and relative positions of these islands which is essential in achieving a high level of device performance.

Early work on self-assembly of epitaxial islands focused on achieving regular two dimensional arrays with islands of uniform size [8–16]. Zinke *et al* [9] investigated the dynamics of clustering of Ge on Si(111) and Si(100) substrate. They grew their samples in an ultra high vacuum. Samples were held at room temperature during deposition of Ge for post-deposit annealing investigations and at 815 K for cluster growth during deposition. Results of their experiment are presented in Figure 1.4 which shows reflection electron micrographs of Ge clusters on Si. The micrographs are for different experimental conditions and display the same cluster shape. Also, the cluster shape is conserved during cluster ripening. They also showed that the late stage of clustering is well described by ripening mechanics which predicts the time dependence of the growth rate and cluster size distribution. For post-deposition

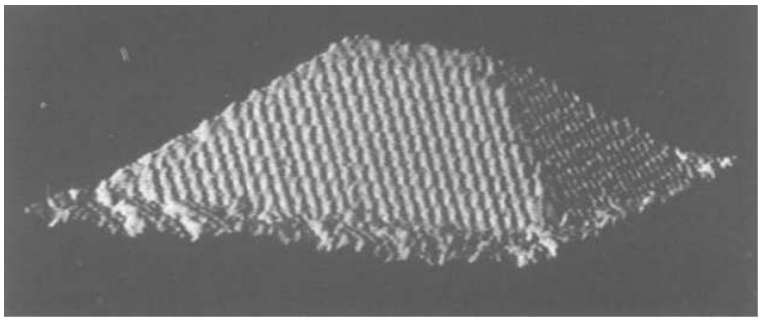

Figure 1.5: STM image of "single" hut cluster observed by Mo *et al.* Scan area is 400 Å×400 Å and the height of the cluster is 28 Å [10].

annealing Zinke *et al* [9] found the cluster-volume growth rate to be linear with time in agreement with an Ostwald-ripening mechanism.

In another study, Mo *et al* [10] investigated the transition from 2D (layer-by-layer) to 3D islands growth of Ge on Si(001) with Scanning Tunneling Microscopy (STM). They have found an intermediate metastable 3D phase consisting of small hut clusters that have specific facet crystallography and alignment of their principal axis with respect to the substrate as shown in Figure 1.5. The clusters consist of four-sided huts with four equivalent {105} facets.

Floro *et al* [14,16] observed enhanced organization during an early stage of growth when islands are small and densely packed and before large scale coarsening tends to occurs. Several mechanisms by which small nanoscale islands might resist coarsening have been proposed in the literature [16–18]. A key observation is that island interactions at close range tends to promote organization [16].

Use of anisotropy in the organization of islands:

There has been an effort to organize epitaxial islands on a substrate by exploiting material anisotropies. For example, Plass *et al* [19] describes a self-

assembled domain pattern of lead deposited at a temperature of 673 K on a solid surface of copper. Figure 1.6a–g is a sequence of low-energy electron microscope (LEEM) images shows the evolution of a pattern from circular islands (average diameter, 67 nm) to stripes and then to circular holes within the lead-overlayer matrix. This sequence of domain patterns, referred to as droplets, stripes and inverted droplets, respectively. For both droplets and stripes, the feature size decreases with increasing temperature. The reason for this is a reduction in the domain-boundary free energy with increasing temperature. For droplets and inverted droplets, reducing the temperature also allows improvement in the long-range order. Figure 1.6h is a LEEM image showing the degree of long-range order that Plass *et al* obtained in the inverted-droplet phase. Gao *et al* [20] conducted a theoretical study to understand these pattern formation. They observe similar patterns to those observed by Plass *et al* [19] in a binary monolayer on the substrate in the case of anisotropic surface stress. Gao *et al* [20] calculated the mesophase transition by using an energy minimization method. When the surface stress tensor is anisotropic, they found that the stripes can be along or off the principal axis of the surface stress tensor depending on the degree of surface stress anisotropy. The formation of the off-axis stripes compromises the inplane and antiplane deformation. Zhang [21], through the kinetic simulation of surface evolution, demonstrated that surface energy anisotropy can affect self-organization and cause shape transitions to occur in epitaxial islands. In his formulation, Zhang assumed that surface energy is a smooth function of surface orientation and its anisotropy is of fourfold symmetry on the (001) plane surface. To get the exact 3D form of surface energy Zhang started with (001), (105), and (103) surfaces that were found to be thermodynamically stable and accordingly took their surface energy densities to be local minima. He called these minima 'first minimum,' 'second minimum,' and 'third minimum,' respectively. He found

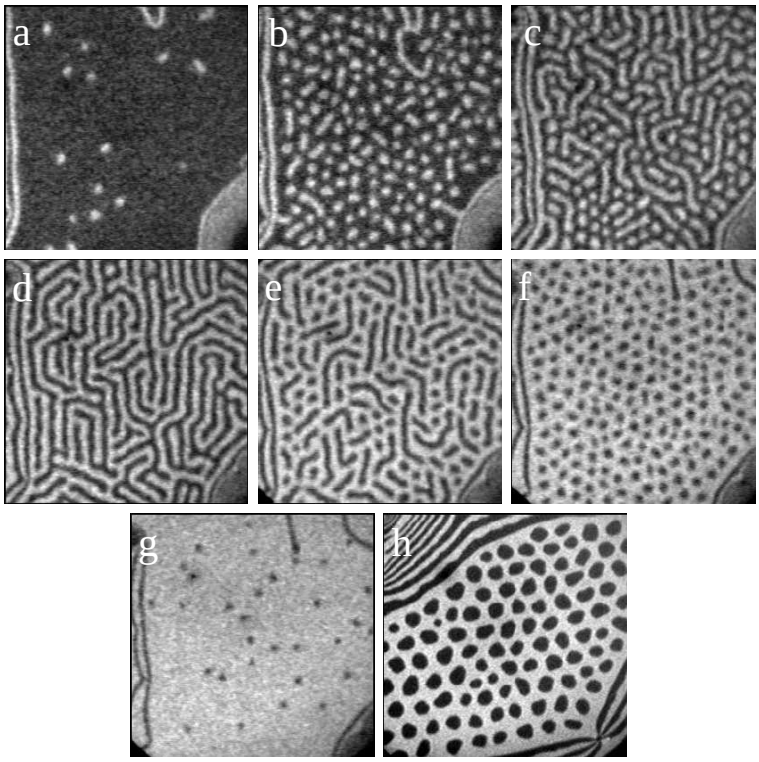

Figure 1.6: Low-energy electron micrographs obtained by Plass *et al* of the Cu(111) surface at 673 K with different area fractions of the lead-overlayer phase (bright) in the surface alloy phase (dark). a-g, Area fractions 0.03, 0.28, 0.35, 0.50, 0.65, 0.73 and 0.95, respectively. The domain pattern evolves from circular islands (droplets) to stripes, to vacancy islands (inverted droplets) with increasing lead coverage. h, Ordered droplet configuration at 623 K. Scale bar, 0.5 μm [19].

that with weak surface energy anisotropy or without surface energy anisotropy, islands are unstable and undergo ripening. If the energy barrier between the second minimum and the third minimum is high, then no island transition occurs and only square based or elongated square-based islands appear. If the energy barrier between the second minimum and the third minimum is intermediately high, then a bi-modal island distribution appears. The islands can coexist without ripening even when subjected to long-time annealing. If the energy barrier between the second minimum and the third minimum is low, then all islands evolve into the third minimum without being trapped in the second minimum. Through this work Zhang demonstrated that strongly self-organized and nonripening island arrays may be obtained by choosing certain surface energy anisotropies by tailoring the material composition and/or by changing the annealing temperature. The effect of growth rate on the organization of islands under anisotropic condition is not discussed by Zhang.

Liu *et al* [22, 23] show that elastic anisotropy can guide the formation of epitaxial islands into regular arrays. Liu *et al* [22] used a three-dimensional finite element method to investigate the effect of growth rate and elastic anisotropy on surface evolution and island formation. They have shown that elastic anisotropy strength plays an important role in surface roughening and island self-assembly. For higher values of anisotropy strength, Liu *et al* [22] found that ripples and islands become increasingly aligned along the $\langle 100 \rangle$ directions, the quality of self-assembly of islands improved, and the roughness wavelength and island spacing are increased. For smaller anisotropy strength they observed that ripples and islands become increasingly aligned along the $\langle 110 \rangle$ directions, the quality of self-assembly of islands is also enhanced, but the roughness wavelength and island spacing are decreased. Eggleston and Voorhees [24] calculated spatially ordered nanocrystals with a nearly monodisperse size distribution for systems with highly anisotropic surface energy. They

used the phase-field model to compute the morphological evolution of growing, misfitting film.

The use of anisotropy enhances the organization of islands but it offers limited control over the organization. The ordering of islands can be controlled more efficiently by the preferential growth of islands over engineered or naturally forming defects present into the substrate. One example is arrays of dislocations network present beneath the surface of the substrate.

Use of defects in the organization of islands:

Some recent experimental work has suggested that the spatial ordering of islands may be controlled by patterning the substrate with defects that produce an inhomogeneous strain field which guides islands positioning [25,26]. The effect of strain patterning on the development of ordered arrays was investigated by Wise *et al* [27]. One of the defect sites used for the organization of islands is arrays of dislocations present beneath the surface of the substrate [28–31]. In the case of a lattice mismatch between the film and substrate materials, strain energy builds up during growth. Beyond a critical layer thickness the strain energy is enough to drives the formation of misfit dislocation resulting in plastic strain relief [32–35]. Directly above the dislocation line the strain is relieved most efficiently, while the strain relief is not as effective far from dislocations [29]. This results in the preferred positions directly above the dislocation line for deposited islands to form.

Chambliss *et al* [28] observed regular arrays of Ni islands deposited on Au(111). They found the Ni islands to form 73 Å apart in rows along $[1\bar{2}1]$ with 140 Å between rows. This nucleation is caused by the long-range herringbone reconstruction of Au(111), which induces periodic "surface-lattice dislocations". The effect of dislocation morphology on the arrangement of islands is not discussed by them.

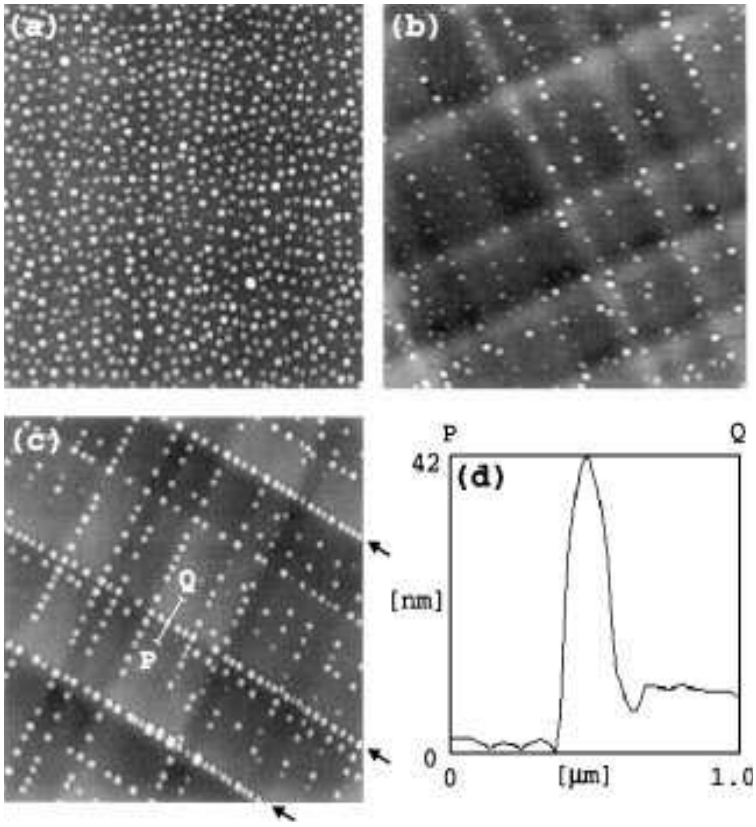

Figure 1.7: The AFM images of the Ge deposition on the surface of a (a) virgin (001)Si wafer and of (b) prestructured $Si_{1-x}Ge_x$/Si and (c) Si-cap/$Si_{1-x}Ge_x$/Si substrates. (d) A height profile through an island in (c) along the line P-Q is shown [29].

Shiryaev *et al* [29] have shown that strained $Si_{1-x}Ge_x$/Si systems possess the ability to control the lateral distribution of Ge islands. The patterned surfaces used in their study were created by a technique which is based on the properties of the dislocation configurations in compositionally graded $Si_{1-x}Ge_x$. Far away from equilibrium, these configurations generate ordered, long-range coherent patterns of highly-localized plastic and elastic displacements on the surface. They have demonstrated that simply by changing the dislocation morphology in the underlying substrate one can achieve remarkable rearrangements in the island patterns as illustrated in Figure 1.7. They observed the island rows aligned with the dislocation bands in the systems involving linear graded substrates (the Ge composition varies linearly). The role of coarsening has not been discussed by Shiryaev *et al*. Voigtlander *et al* [30] considered ordering effects of Ge islands above a dislocation network with a periodicity of 100 Å. In their experiments, they observed the ordering of two-dimensional islands on a Ge layer with a periodic strain field at the surface. They found that the coarsening process enhances the ordering. Due to repeated detachment from islands, adatoms approach the positions above the misfit relieving dislocations. Voigtlander *et al* [30] found that both, kinetic mechanisms (strain dependent diffusion) and energetic mechanisms (strain dependent binding) lead to ordered growth with respect to an underlying dislocation network. The Ge coverage may have some effect over the organization of islands. This issue is addressed by Xie *et al* [31]. They conducted some experiments by using relaxed SiGe thin films as templates to find the efect of growth temperature as well as Ge coverage over the organization of islands. The objective of the relaxed template is to create a regularly distributed variation of the in-plane lattice constant using the misfit dislocation network buried underneath the surface. They observed the absence of islands at locations other than intersections of misfit dislocations. The island sizes are far from uniform,

with the tendency of similar sized islands to line up along selected lines. On reducing the Ge coverage as well as the growth temperature they found a more narrow distribution of islands and much smaller Ge island sizes.

Island formation is a natural phenomenon and is readily achieved. However arranging islands into regular arrays or more complex configurations is a difficult task. One approach to achieving regular arrays of islands is the stacking of successive layers of islands separated by capping layers of another material [36], as shown in Figure 1.8. The strain from one layer of islands helps to determine the position of the islands in overlying layers so that the spacing in successive layers becomes more uniform. Xie *et al* [36] deposited two monolayers of InAs on GaAs (100) substrate at a temperature that encourages diffusion. In their experiment, Xie *et al* [36] obtained an average island density of $\sim 350/\mu m^2$, average height of 35 Å, and an average lateral size of $\sim$ 170 Å. However, a large number of layers must be grown to position the islands with good uniformity [37]. The deposition of numerous layers is time consuming and produces a thick stack that may make integration with other devices difficult.

The drawback of having to form a thick stack due to multiple layer stacking can be overcome by using Si overgrowth on a single layer of Ge islands grown by chemical vapor deposition on Si(001) [38]. Here the lateral motion of Ge islands can be diminish by means of Si overgrowth. The deposition of silicon induces a shape transformation from domes to truncated pyramids with a larger base, generating an array of closely spaced interacting islands and resulting in laterally ordered Ge islands. Capellini *et al* [38] conducted the study on two sample series through the deposition of variable thickness Si-capping layers on morphologically identical Ge island layers. In the first series, both the island layer ($\sim$ 1.5 nm Ge nominal thickness) and the silicon cap layer were deposited at same temperature, while in the second series, the island layer

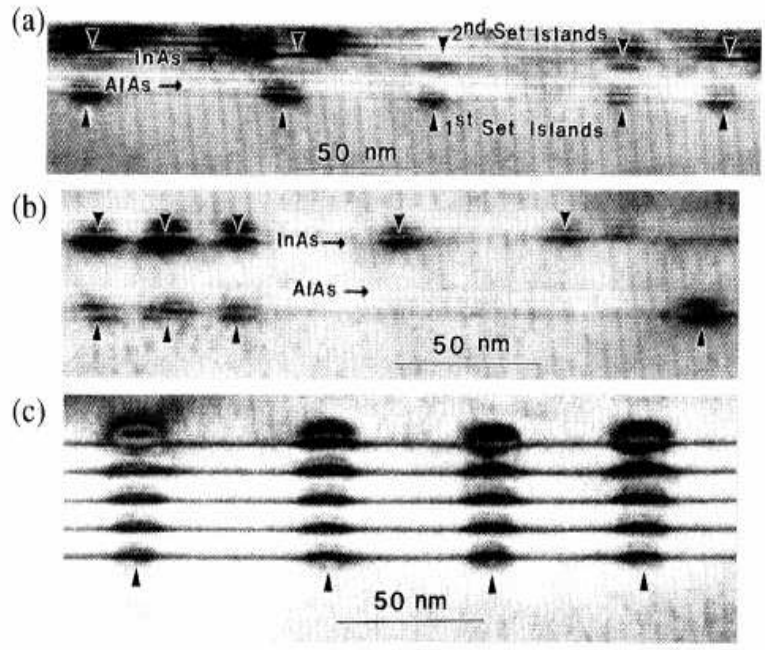

Figure 1.8: TEM pictures reproduced from Xie *et al.* Typical bright field TEM pictures along [011] azimuth of the samples with two sets of islands separated by (a) 46 and (b) 92 ML spacer layers respectively. (c) Dark field TEM picture for a sample with five sets of islands separated by 36 ML spacer layers [36].

($\sim$ 3 nm Ge nominal thickness) was deposited at lower temperature than the silicon capping layer. They found that the ordering process of Ge(Si) islands is proportional to the actual coverage of the substrate, even in the case where the reduced separation between islands are obtained by Si intermixing, via overgrowth. This method is not very efficient for producing highly organized quantum dots that is needed for high level of device performance.

Though the defects present beneath the surface of the substrate help to guide island positioning, they could degrade the device performance. Also the control over the organization of islands is limited in the case of defects present in the substrate. One method to overcome this drawback is to use a topographically surface feature that may occur naturally or might by engineered.

Effect of patterned substrate on the organization of islands:

Pre-patterning a substrate with topographical features can offer better control over the sites where islands tend to form. Here idea is to use relatively large scale feature made by standard techniques to guide positioning of self-assembled nanoscale features. The patterned substrate provides compliant regions where islands can relax their residual strain. These compliant regions are possibly preferred positions for the formation of islands. For example, in the case of a raised mesa or pilar etched into the substrate surface, the boundaries are more compliant than inner regions. It is there expected that strained epitaxial islands are most likely to form at the boundaries.

Lee *et al* [39] used prepatterned GaAs(100) substrates to fabricate InGaAs QDs. The resulting layer of QDs was then used as the seed layer at the bottom of a vertical stack of ten layers of QDs in order to induce specific lateral spatial QD patterns in the top layer. The samples were grown by solid source molecular beam epitaxy on pre-patterned GaAs(100) substrates. The patterns were prepared by photolithography and were etched in H_2SO_4. The

patterns used in their investigation were composed of 1.5 μm wide lines along both the [011] and [01$\bar{1}$]directions. The lines were typically 5 μm in length for above (mesa) and below (trench) surface lines and squares with a height or depth of 35 nm for both line and square structures. Different samples were prepared by varying the InGaAs ML coverage and consequently the QD density. They have found that with relatively high ML coverage, QD chains were formed all over the surface with total disregard for the pre-patterned regions. However, with reduced coverage a QD density was selected that allowed QD formation to be substantially influenced by the pre-patterned substrates, as illustrated in Figure 1.9. As can be observe from the figure that islands prefer the edges of the mesa.

The effect of mesa width on islands positioning is discussed by Kamins *et al* [40]. They discussed the positioning of self-assembled Ge islands adjacent to features formed by conventional lithography. They form patterns by using optical lithography in Si(001) wafers which are oriented in either the $\langle 100 \rangle$ or $\langle 110 \rangle$ direction. They observed single rows of islands near the edges of narrow Si lines and multiple rows of islands on wider Si lines as shown in Figure 1.10. The islands were approximately 86 nm wide and 15 nm high, with a reasonably narrow size distribution. The alignment is probably due to favorable nucleation sites at atomic steps on shallow facets. Therefore, the position of the Ge islands can be influenced by controlling the shape of the underlying Si surface, allowing very small islands to be formed and positioned in predetermined locations using conventional lithography with moderate resolution. While this work delt only with linear (one dimensional) arrangements of islands, many applications requires two-dimensional arrangements.

In recent experiments, configurations such as straight lines [41–44] and circular arrangements [45–48] of islands have been obtained. Kitajima *et al* [46] demonstrated the arrangement of Ge islands over Si(001) substrate patterned

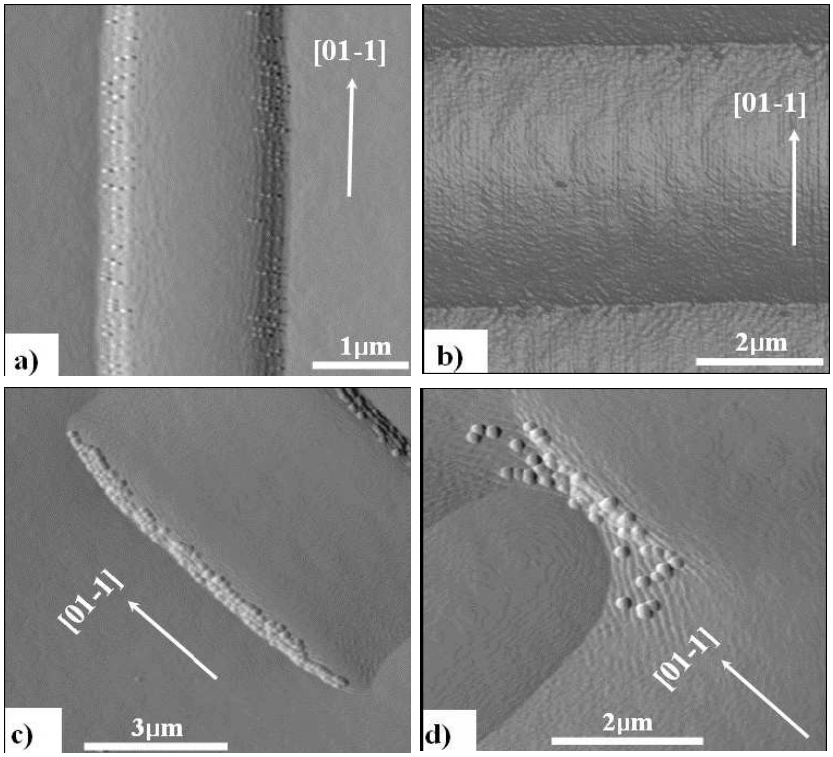

Figure 1.9: AFM images for pre-patterned QD growth observed by Lee *et al*:(a) 4×4 μm^2 area AFM image from a line pattern along $[01\bar{1}]$, (b) 6×6 μm^2 area AFM image from the line pattern along [011], (c) 8×8 μm^2 area and (d) 5×5 μm^2 area are the AFM pictures of upward and downward squares [39].

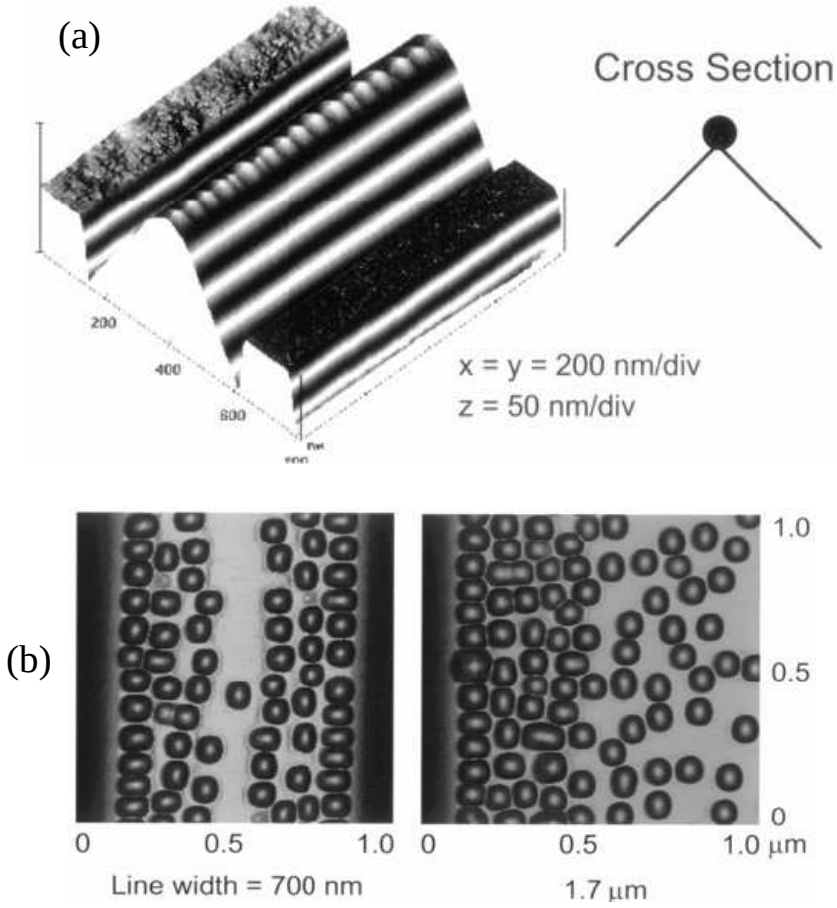

Figure 1.10: Experimental results of Kamins *et al*:(a) the top of the Si line narrows to a ridge, a single row of Ge islands forms at the top of the ridge, (b) 2D atomic-force micrographs of Ge islands on Si lines of 700 nm and 1.7 μm wide, showing ordering of several rows of Ge islands along the edges of the Si line. The central region of 700 nm wide Si line is narrow and contains no Ge islands while the central region of 1.7 μm Si line is wide, allowing Ge islands to nucleate randomly [40].

with square-like mesas. The spacing of features on the substrate surface was limited to 120nm due to the resolution limits of the lithographic technique. Material was deposited via molecular beam epitaxy. They found that for relatively large mesas, islands organize themselves around the edges of the mesa. On reducing the mesa size Kitajima *et al* [46] found islands at the corners of the mesa. On further reducing the mesa size a single island was observed at the center as shown in Figure 1.11. In another experiment on the same system, Jin *et al* [41] observed island formation at the corners of a square mesa with the base square oriented in the $\langle 110 \rangle$ directions, as shown in Figure 1.12(a). In contrast to the boundaries, the central region is free of Ge islands. This is because the central region is like a not preferred sites for islands and Ge adatoms have a sufficiently long diffusion length to migrate to the corners. On increasing the nominal Ge thickness, a fifth island forms in the center of the square mesa, as shown in Figure 1.12(b). They have found that the central island to be pyramidal with a square base, which is different from the other four dome-shaped islands at the corners.

Recently, theoretical work has been done to understand this behavior. Kukta and Kouris [49] investigated the energetic and kinetic mechanisms that guide the positioning of strained epitaxial islands deposited over sinusoidal substrate. In another study, Machtay and Kukta [50] calculated minimum energy configuration of islands deposited atop a raised mesa. Both of these investigations assumed a two-dimensional (plane strain) model. While these studies explain certain characteristic behaviors, they miss features inherent to the three-dimensional nature of real systems. One aspect of this thesis is to extend their ideas to three-dimensions.

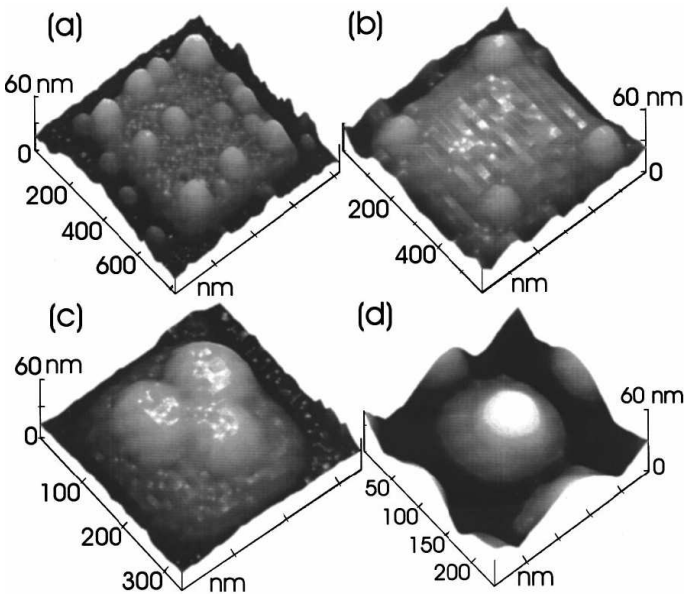

Figure 1.11: Experimental results by Kitajima *et al* [46] Atomic force microscopy images for square mesa dimensions of (a)700nm, (b)500nm, (c)300nm, and (d)140nm.

1.2 Focus of this Research

The focus of this thesis is understanding the mechanisms of self-assembly of islands deposited epitaxially onto a substrate. The self-assembly addressed here is driven by in-plane anisotropies in surface stress and lattice mismatch between the film and substrate materials, defects in the form of dislocation lines present beneath the surface of the surface, and topographically patterned substrate. The first phase of this work is focused on the use of material anisotropy in the organization of islands. The main advantage of introducing anisotropy is that it might suppress defects in quantum dot arrays. In other words, it encourages the formation of near perfect hexagonal or rectangular arrays, eliminating irregularities in the arrays. Irregularities tend to degrade device performance. Control over island positioning beyond arrays is not possible with the use of anisotropy alone. Toward greater control, we subsequently

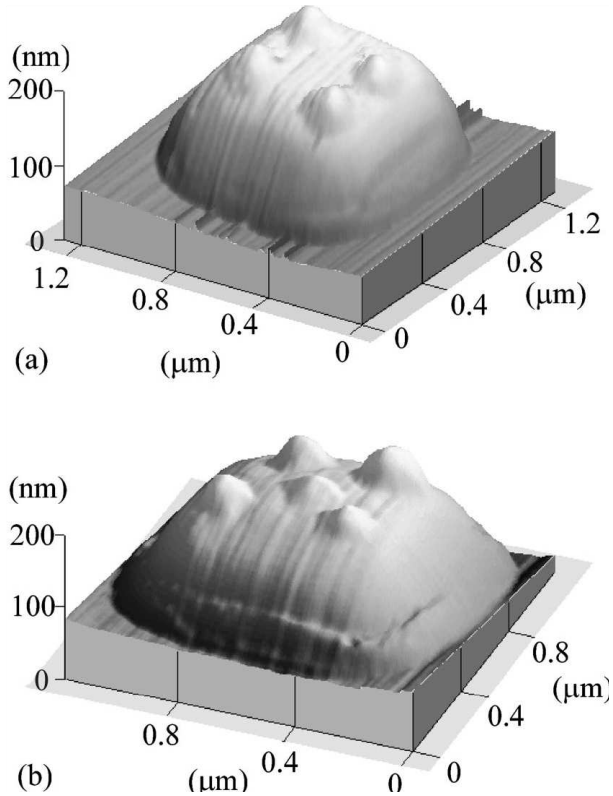

Figure 1.12: Experimental results by Jin *et al* [41] (a) A 3D AFM image with four Ge islands located at the corners on a square Si mesa with the base lines parallel to the $\langle 110 \rangle$ directions. The Ge thickness is 9 ML. (b) A 3D AFM image with five Ge islands with 10 ML Ge. The fifth pyramidal island is formed in the central region. The average base size of the islands is about 140 nm.

study the organization of islands guide by lattice defects. The effect of buried dislocation networks in the substrate on the relative arrangement of islands is investigated. While defects provide some control, they are limited by the arrangement of defect that arise naturally. In interest of further control, the organization of islands deposited on topographically patterned substrates is studied. In all these studies our interest is on sub-monolayer growth where islands are atomically flat raised terraces bounded by steps on the substrate surface. This is distinguished from Kukta and Kouris [49] and Machtay and Kukta [50] where large macroscopic islands were considered. Surface steps that beyond a monolayer island, induce an elastic field in the system through which they interact with each other. Driven by these interactions, the morphology evolves by mass transport. The model used for the elastic field of a surface step follows those of Alerhand et al. [51] and Tersoff et al. [52, 53] which account for the effects of different surface stresses on the film and substrate surfaces and a lattice mismatch between the film and substrate materials respectively. In both cases the elastic field of a step is that of a line distribution of force applied on the surface of an elastic half space. The magnitude and character of the force depends on the difference in surface stress, the lattice mismatch, step height, and step orientation. A model is first constructed for morphological transformations through mass transport by the mechanism of condensation/evaportion. Next, the model of a surface step, including the interaction energy of two surface steps, is reviewed. Subsequently, the self-energy of a square island and interaction energy between two islands is calculated. These are needed to evaluate the driving force for morphological transformations as an island changes size, shape, or translates in the elastic field induced by other islands for isotropic as well as anisotropic conditions.

Chapter 2

Island Evolution during Crystal Growth

Crystal growth involves the deposition and attachment of atoms onto a substrate. The driving force for crystal growth and the individual processes that lead to crystal growth is a decrease in the system's free energy. If energy increases as atoms condense from the vapor onto the substrate, crystal growth will not occur. Crystal growth is possible only if the result is a net decrease in energy. On the atomic scale, growth occurs as atoms land on the substrate surface and adsorb to become adatoms. An adatom belongs neither to the vapor nor to the bulk crystal – it is at an intermediate state. For an adatom to become part of the bulk, it must find a stable low-energy site, typically at the edge of a monolayer island (a stable cluster of atoms). If an adatom does not find a low-energy site, it will detach from substrate and return to the vapor. The attachment and detachment of atoms is a local phenomenon that depends on the local temperature and as well as the local chemical potential. The rates at which attachment and detachment occur depends on both of these factors. Hence, even in instances of uniform temperature, crystal growth may occur at some locations while evaporation is occurring at others. The discriminating factor is the chemical potential.

Consider the processes of adsorption and desorption as shown in Fig-

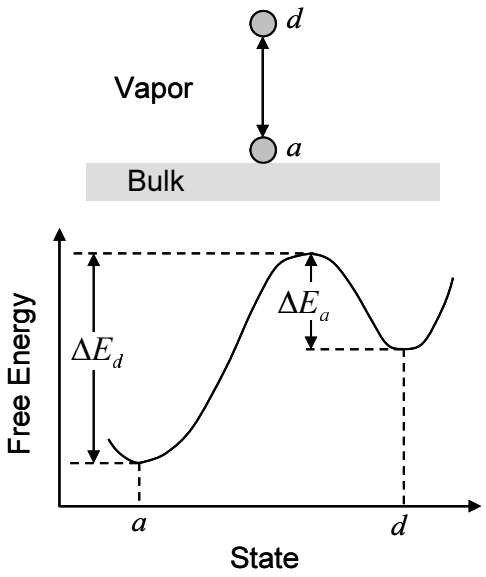

Figure 2.1: A schematic variation of free energy with the state of atoms. Atoms at the adsorbed state (a) has the lower free energy than that at the desorbed state (d). The energy barrier an atom has to overcome to jump from state a to state d is $\triangle E_d$, while from state d to state a, $\triangle E_a$ is required.

ure 2.1. State a corresponds to an atom adsorbed on the substrate surface and state d corresponds to a desorbed (vapor) atom. Both states represent local free energy minima, but the adsorbed state is considered to have the lower energy – hence a net flux of atoms from the vapor to the surface is expected. The difference in energy between these states is called the chemical potential for adsorption $\chi = E_a - E_d$, where E_a and E_d are respectively the energies of states a and d. Chemical potential χ is the increase in free energy associated with the adsorption of an atom, and a negative chemical potential implies a tendency for crystal growth.

Adsorption and desorption do not occur spontaneously, as there are activation barriers that must be overcome for the processes to occur. Let ΔE_a be the activation energy for adsorption and ΔE_d be the activation energy for desorption, as illustrated in Figure 2.1. Also note from Figure 2.1 that

$$\Delta E_d - \Delta E_a = E_d - E_a = -\chi \tag{2.1}$$

According to kinetic theory, the probability of an atom in vapor state reaching the activated state is given by $\exp(-\triangle E_a/kT)$, where k is Boltzmann's constant and T is the temperature. The rate at which the transformation occurs is the attempt frequency times the probability of an atom being in the activated state, or

$$r_a = A_a\, e^{-\Delta E_a/kT} \tag{2.2}$$

where A_a is the frequency factor for adsorption. Using the analogous rate equation for desorption, the net rate of adsorption is calculated as

$$r = r_a - r_d = A_a e^{-\Delta E_a/kT} - A_d e^{-\Delta E_d/kT} \tag{2.3}$$

Then using (2.1) in this expression, and assuming that $\chi \ll \Delta E_a$, which applies to systems where the crystal and vapor are close to equilibrium, the

rate of adsorption becomes

$$r \approx \left[\left(\frac{A_a}{A_d} - 1\right) kT - \chi\right] \frac{A_d}{kT} e^{-\Delta E_a/kT} \tag{2.4}$$

Suppose that all of the parameters in (2.4) except χ are independent of position on the substrate surface. This implies that temperature is uniform and the density of adatoms and vapor atoms (*i.e.* A_a and A_d) are uniform, which is valid for systems sufficiently close to equilibrium. The activation energy ΔE_a is also assumed to be uniform. This is approximately true only if adsorption/desorption is limited to specific sites, for example at the edges of monolayer islands or on the surface of a flat substrate; separate site-specific rate equations would be needed in order to consider both locations. As this work will focus on heterogenous growth by attachment to islands, it is sufficient to treat ΔE_a as a constant. Given these assumptions, (2.4) can be rewritten to reflect two distinct processes, a uniform deposition rate r_{dep} that adds atoms to the crystal and a mass conserving adsorption/desorption process (generically called condensation/evaporation),

$$r \approx r_{dep} + B(\bar{\chi} - \chi) \tag{2.5}$$

where B and $\bar{\chi}$ are constants. The constant $\bar{\chi}$ enforces conservation of mass in the crystal and is later shown to be average of the chemical potential taken over the substrate surface. The advantage of (2.5) is that mass conservation can be enforced simply by setting the deposition rate r_{dep} to zero. This makes it possible to calculate equilibrium configurations for a fixed amount of deposited material. When $r_{dep} = 0$, the system evolves as atoms detach from sites of high chemical potential (high free energy) and then reattach at sites of low chemical potential. The net effect is a decrease in the total free energy.

Condensation/evaporation at island edges is a simplified version of the actual process of crystal growth. In reality, when an atom attaches to the substrate, it has a finite life span as an adatom before it either becomes part of the

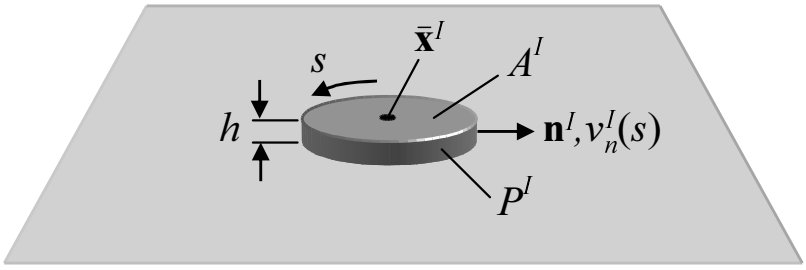

Figure 2.2: Schematic of an island deposited on a substrate. The island is characterized by its projected area A^I, centroidal position $\bar{\mathbf{x}}^I$, height h^I, perimeter P^I, outward pointing unit normal $\mathbf{n}^I$. Its boundary evolves with local normal velocity of $v_n^I(s)$.

growing crystal or detaches back in the vapor. During its lifetime, an adatom may diffuse along the surface, seeking a low-energy site for it to attach. Like adsorption and desorption, surface diffusion is a thermally activated process. Hence the distance an adatom can diffuse before it returns to the vapor, its diffusion length, depends on the activation energy of diffusion versus that of desorption. Neglecting surface diffusion is to imply that the activation energy for desorption is small compared to that of diffusion (*i.e.* the diffusion length is small). In cases where the diffusion length is large compared to the size of morphological features, the assumption of evolution by condensation/evaporation will not capture the transient kinetics. Nevertheless it will suggest the general trend of the evolution towards a minimum energy configuration. Surface diffusion is neglected in this investigation, as solving the diffusion problem is computational intensive and would severely limit the parameter space that could be probed.

2.1 Model of the evolution of islands

Consider a substrate with monolayer islands of various sizes. A typical island, island I, is illustrated in Figure 2.2. It is characterized by its height h^I,

projected area A^I, perimeter P^I of its projected area, and the position $\bar{\mathbf{x}}^I$ of its centroid. The shape of the island is represented by the outward pointing unit normal $\mathbf{n}^I$ to its projected area, which depends on the arclength s measured from a point along the island's perimeter. The island changes shape (grows or shrinks) as atoms are deposited at or removed from the island edge. This is represented by a normal velocity v_n^I of the island edge, which is a function of position s on the perimeter. Following (2.5), the normal velocity is given by

$$v_n^I(s) = v_{dep} + C\left[\bar{\chi} - \chi^I(s)\right] \tag{2.6}$$

where v_{dep} is a constant growth velocity arising from the incident deposition flux, χ^I is the local chemical potential along the island perimeter, and C and $\bar{\chi}$ are constants.

In the case of no deposition ($v_{dep} = 0$), the total mass (or volume, assuming a single species) of the crystal is conserved. Thus for a system with N islands of height $h^I = h$, conservation of mass implies

$$\sum_{I=1}^{N} \int_{P^I} h^I v_n^I \, ds = hC \sum_{I=1}^{N} \int_{P^I} \left[\bar{\chi} - \chi^I(s)\right] \, ds = 0 \tag{2.7}$$

where (2.6) was used to obtain the second expression. Solving this result for $\bar{\chi}$ yields

$$\bar{\chi} = \frac{\sum_{I=1}^{N} \int_{P^I} \chi^I(s) \, ds}{\sum_{I=1}^{N} P^I} = \frac{\sum_{I=1}^{N} \bar{\chi}^I P^I}{\sum_{I=1}^{N} P^I} \tag{2.8}$$

where

$$\bar{\chi}^I \equiv \frac{1}{P^I} \int_{P^I} \chi^I \, ds \tag{2.9}$$

is the average chemical potential taken over the perimeter of island I. Hence $\bar{\chi}$ is the average of the chemical potential taken over the edges of all islands.

One can verify that evolution by condensation/evaporation decreases the free energy of the crystal. Recall that the chemical potential χ is defined as the increase in free energy due to introduction of an atom at a point. Then

the change in free energy with evolution is given by

$$\dot{E} = \sum_I \int_{P^I} \frac{\chi^I}{\Omega} v_n^I \, h \, ds \tag{2.10}$$

where Ω is the atomic volume (volume per atom). Combining equations (2.6) with $v_{dep} = 0$ and (2.10) results in

$$\begin{aligned} \dot{E} &= \sum_I \left(\frac{Ch}{\Omega} \int_{P^I} \chi^I [\bar{\chi} - \chi^I] \, h \, ds \right) \\ &= \frac{Ch}{\Omega} \sum_I \left(\bar{\chi}^2 \int_{P^I} ds - \int_{P^I} \chi^2 \, ds \right) \leq 0 \end{aligned} \tag{2.11}$$

It is noted that deposition v_{dep} will occur such that the *total* free energy of the system, the vapor plus the bulk crystal, is reduced. Physically this controlled through temperature and the pressure of the vapor, but for the current purposes it can be treated as a free parameter of the model.

Supposing that the chemical potential χ^I is known for each island, the evolution is completely described by (2.6). Equation (2.6) is a local expression for the normal velocity at a point on an island. This investigation is less concerned with the specific shape of individual islands than it is with the sizes and relative positions of many islands. It is therefore prudent to simplify the model by restricting the evolution such that islands can grow in size and change position, but not change shape. The normal velocity of an island is constrained as

$$v_n^I(s) = V_n^I + \bar{v}_i^I n_i^I(s) \tag{2.12}$$

where V_n^I is a scalar constant, $\bar{v}_i^I$ are components of a vector constant, n_i^I are components of the outward unit normal defined in Figure 2.2. Here and elsewhere the summation over repeated indices is implied. V_n^I represents a uniform expansion while $\bar{v}_i^I$ represents a translation in the plane of the substrate. The velocity V_n^I is directly related to rate of area change of the island as follows:

$$\dot{A}^I = \frac{d}{dt} \int_{A^I} dA = \int_{P^I} v_n^I \, ds = V_n^I \int_{P^I} ds + \bar{v}_i^I \int_{P^I} n_i^I \, ds = V_n^I P^I \tag{2.13}$$

The physical interpretation of the velocity $\bar{v}_i^I$ is obtained first by considering the definition of the centroid $\bar{\mathbf{x}}^I$,

$$\bar{x}_i^I A^I = \int_{A^I} x_i dA \tag{2.14}$$

Taking the time derivative of this equation and using (2.12), one finds

$$\begin{aligned} \dot{\bar{x}}_i^I A^I + \bar{x}_i^I \dot{A}^I &= \int_{P^I} x_i v_n^I \, ds \\ &= V_n^I \int_{P^I} x_i \, ds + \bar{v}_j^I \int_{P^I} x_i n_j \, ds \\ &= V_n^I \int_{P^I} x_i \, ds + \bar{v}_j^I \int_{A^I} \delta_{ij} \, dA \\ &= V_n^I \int_{P^I} x_i \, ds + \bar{v}_i^I \, A^I \end{aligned} \tag{2.15}$$

Then introducing (2.13) into (2.15) and reorganizing gives

$$\begin{aligned} \dot{\bar{x}}_i^I A^I &= V_n^I \int_{P^I} (x_i - \bar{x}_i^I) \, ds + \bar{v}_i^I \, A^I \\ &= \bar{v}_i^I \, A^I \end{aligned} \tag{2.16}$$

which implies

$$\dot{\bar{x}}_i^I = \bar{v}_i^I \tag{2.17}$$

Hence $\bar{v}_i^I$ is the velocity of the island's centroid.

The evolution equation (2.6) must be constrained according to (2.12). This implies that separate evolution equations are needed for the growth velocity V_n^I and the translation velocity $\bar{v}_i^I$ of an island. To obtain the evolution equation for V_n^I, consider (2.13) along with the local evolution equation (2.6),

$$V_n^I P^I = \int_{P^I} v_n^I \, ds = \int_{P^I} \left[(v_{dep} + C(\bar{\chi} - \chi^I) \right] \, ds \tag{2.18}$$

Using (2.9) in this expression, one finds

$$V_n^I = v_{dep} + C(\bar{\chi} - \bar{\chi}^I) \tag{2.19}$$

The evolution equation for $\bar{v}_i^I$ is obtained by considering the integral

$$\int_{P^I} v_n^I n_i^I \, ds = \int_{P^I} \left[(v_{dep} + C(\bar{\chi} - \chi^I) \right] n_i^I \, ds = -C \int_{P^I} \chi^I n_i^I \, ds = -C \bar{\chi}_i^I \tag{2.20}$$

where the translation potential $\bar{\chi}_i^I$ is defined as

$$\bar{\chi}_i^I \equiv \int_{P^I} \chi^I n_i^I \, ds \tag{2.21}$$

Using the constraint (2.12), one finds

$$\int_{P^I} v_n^I n_i^I \, ds = \int_{P^I} \left(V_n^I + \bar{v}_j^I n_j^I \right) n_i^I \, ds = \bar{v}_j^I \alpha_{ji} \tag{2.22}$$

where

$$\alpha_{ij} = \int_{P^I} n_i^I n_j^I \, ds \tag{2.23}$$

is a symmetric tensor that depends on the island's shape. For example

$$\alpha_{ij} = \pi r^I \delta_{ij} \quad \text{for a circular island of radius } r^I \tag{2.24}$$

and

$$\alpha_{ij} = 2L^I \delta_{ij} \quad \text{for a square island of width } L^I \tag{2.25}$$

where δ_{ij} the Kronecker delta. By comparing (2.20) and (2.22), the evolution equation for $\bar{v}_i^I$ is found to be

$$\bar{v}_i^I = -C \bar{\chi}_j^I \alpha_{ji}^{-1} \tag{2.26}$$

Given the growth potential $\bar{\chi}$ and the translation potential $\bar{\chi}_i^I$, the growth velocity V_n^I and the translation velocity $\bar{v}_i^I$ are readily evaluated from (2.19) and (2.26). The difficultly is that evaluations of $\bar{\chi}$ and $\bar{\chi}_i^I$ from (2.9) and (2.21) require knowledge of the local chemical potential along an island's perimeter, which is difficult to obtain. An alternate method of evaluating $\bar{\chi}$ and $\bar{\chi}_i^I$ is obtained from the constrained form of the dissipation (2.10). With

the constraint (2.12), equation (2.10) becomes

$$\begin{aligned}\dot{E} &= \frac{h}{\Omega}\sum_{I}^{N}\left(V_n^I\int_{L^I}\chi^I\,ds+\bar{v}_i^I\int_{L^I}\chi^I n_i^I\,ds\right)\\ &= \frac{h}{\Omega}\sum_{I}^{N}\left(V_n^I L^I\bar{\chi}^I+\bar{v}_i^I\bar{\chi}_i^I\right)\end{aligned}\tag{2.27}$$

where (2.9) and (2.21) were used to obtain the last expression. Finally, by introducing the evolution equations (2.13) and (2.17), equation (2.27) can be rewritten as

$$\dot{E}=\sum_{I}^{N}\left(\frac{h\bar{\chi}^I}{\Omega}\,\dot{A}^I+\frac{h\bar{\chi}_i^I}{\Omega}\,\dot{\bar{x}}_i^I\right)\tag{2.28}$$

which implies

$$\frac{\partial E}{\partial A^I}=\frac{h\bar{\chi}^I}{\Omega}\tag{2.29}$$

and

$$\frac{\partial E}{\partial \bar{x}_i^I}=\frac{h\bar{\chi}_i^I}{\Omega}\tag{2.30}$$

Equation (2.29) determines an island's growth potential $\bar{\chi}^I$ in terms of the variation in energy with island size and (2.30) determines an island's translation potential $\bar{\chi}_i^I$ in terms of the variation in energy with the location of the island's centroid. Using these results, the evolution equations become

$$V_n^I=v_{dep}+C\left(\bar{\chi}-\frac{\Omega}{h}\,\frac{\partial E}{\partial A^I}\right)\tag{2.31}$$

and

$$v_i^I=-C\,\frac{\Omega}{h}\,\frac{\partial E}{\partial \bar{x}_j^I}\,\alpha_{ji}^{-1}\tag{2.32}$$

where $\bar{\chi}$ is given by (2.8) with $\bar{\chi}^I$ determined from (2.29). Evaluations of $\partial E/\partial A^I$ and $\partial E/\partial \bar{x}_i^I$ are discussed in the next section.

2.2 Free energy of a monolayer island

The free energy of a monolayer island consists of a surface excess energy and the deformational energy. The deformational energy arises from two factors,

local relaxation of the lattice in the vicinity of step edges and residual elastic strain associated with a lattice-mismatch between the film and the substrate materials. The former arises irrespective of the lattice-mismatch. The model of the elastic field associated with step-edge relaxation and residual elastic strain are discussed below.

Figure 2.3 is two-dimensional illustration of the elastic field of a monolayer island due to an epitaxial mismatch and a remotely applied load. Consider a flat substrate loaded remotely such that it has a uniform stress σ^r as shown in Figure 2.3(a). The monolayer island must be elastically strained in order to achieve epitaxy. Assuming that the elastic constants of the island are the same as those of the substrate, the requisite strain is obtained by tractions of magnitude $\sigma^r + \sigma^m$ distributed over the edges of the island as shown in Figure 2.3(a). The traction σ^m adds the mismatch strain and σ^r adds the strain associated with the applied load. Imagine gluing the island on the substrate while maintaining the applied tractions as shown in Figure 2.3(b). The stresses in the substrate and the island are both uniform. The applied tractions on the step edge are then removed to enforce the traction-free boundary condition. This is done by adding the elastic field due to equal but opposite tractions applied along the step edges as illustrated in Figure 2.3(c). The total elastic field is the superposition of the fields of Figures 2.3(b) and (c). The field of Figure 2.3(c) is highly nonuniform and an analytic solution is intractable. Following Tersoff et al. [52, 53] it can be approximate as the elastic field of Figure 2.3(d) which is a flat half-space with concentrated forces of magnitude $h(\sigma^r + \sigma^m)$. Kukta and Bhattacharya [54] shows that this is a first order approximation of the elastic field for small values of step height h and obtain the second order correction.

The elastic field associated with step-edge relaxation was originally modeled by Marchenko and Parshin [55]. Consider a schematic of a surface

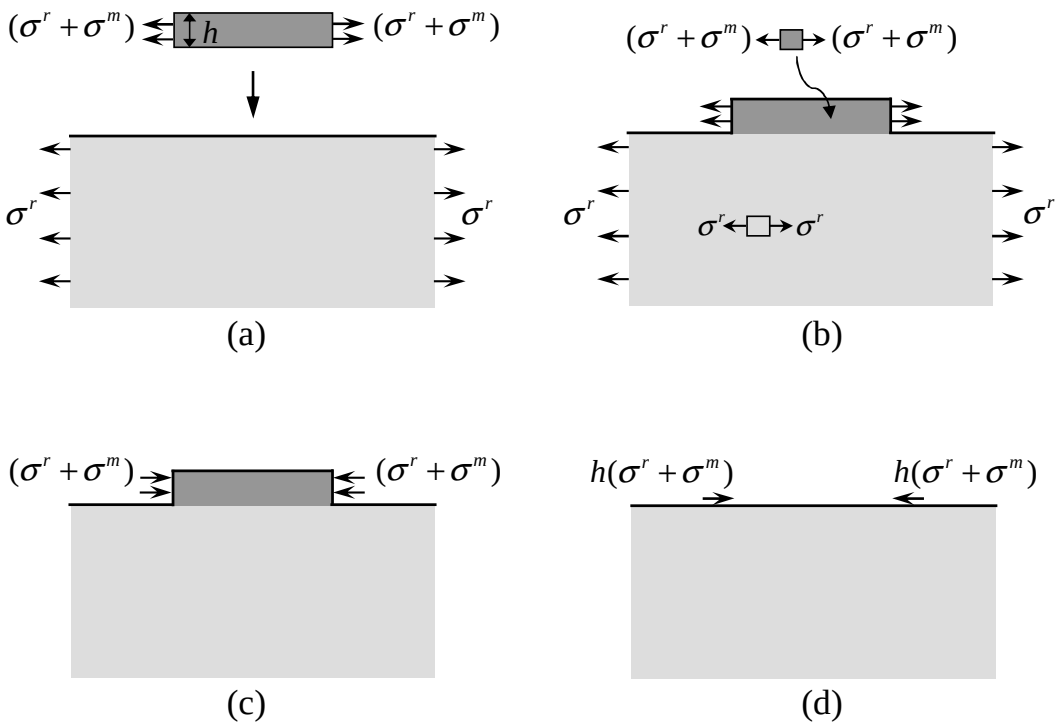

Figure 2.3: Representation of the elastic field of an island due to the remotely applied stress σ^r and the mismatch stress σ^m, h is the height of the island. (a) The film of monolayer thickness is stretched by the traction $(\sigma^m + \sigma^r)$ uniformly distributed over the edges, (b) the stretched island is then glued to the substrate, (c) to maintain the traction free surface of the island equal and opposite traction is applied over its faces, and (d) the approximation of the elastic field of (c) proposed by Tersoff et al. [52, 53].

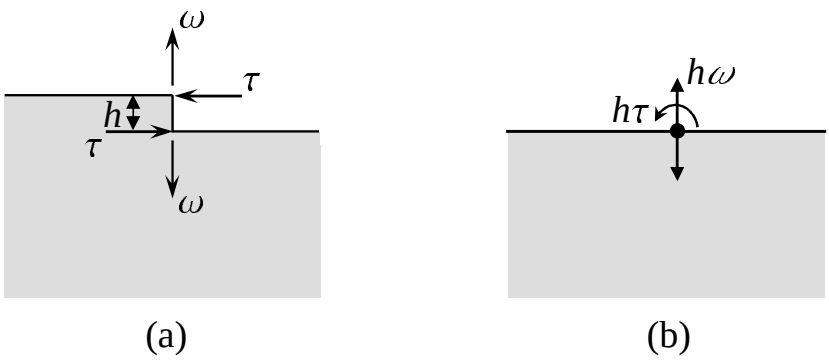

Figure 2.4: (a) Representation of the elastic field of due to surface stresses τ on the terraces adjacent to an atomic step and a dilatation couple ω, (b) equivalent flat surface with a point moment $h\tau$ and point dilatation $h\omega$ where h is the step height.

step shown in Figure 2.4(a). Forces τ are associated with surface stress on the upper and lower terraces adjacent to the step and forces ω account for a dilatational relaxation of atomic positions at the step edge. These forces form a couple or dipole. It is shown by Kukta and Bhattacharya [54] that the elastic field of a force dipole applied at the step gives a first order approximation of the atomic displacements for small values of h/r where h is step height and r is distance from the step. The elastic field of Figure 2.4(a) cannot determined analytically. Marchenko and Parshin [55] suggested approximating the field as that of a point dipole applied on the surface of a half-plane, as illustrated in Figure 2.4(b). The dipole consists of a moment of magnitude $h\tau$ where τ is the surface stress on the upper and lower terraces, and a dilatation of magnitude $h\omega$ where ω can be determined by matching the far-field elastic displacements to those of an atomistic simulation.

Figure 2.5 illustrates the three-dimensional generalization of the models in Figure 2.3(d) and Figure 2.4(b). The elastic field induced by a step with outward point unit normal $\mathbf{n}$ to the step face is approximated by a line force

$$f_i = -h(\sigma^m_{ij} + \sigma^r_{ij})\, n_j \tag{2.33}$$

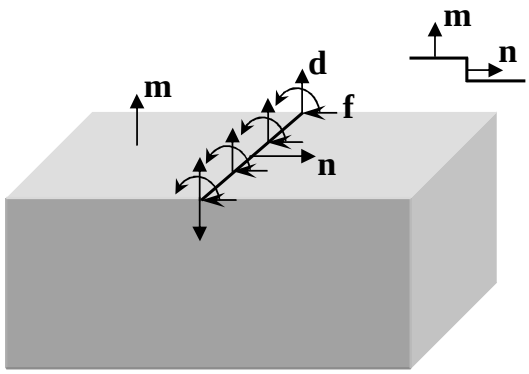

Figure 2.5: Combined three-dimensional representation of the Marchenko and Parshin model [55] shown in Figure 2.4(b) and the nonuniform field in Figure 2.3(d).

and a line force dipole

$$d_{ik} = -h\tau_{ij}n_j m_k + hwn_i n_k \tag{2.34}$$

on a half-space with outward unit normal $\mathbf{m}$. The force and dipole are distributed over a curve that represents the position of the step. The displacement field is given by

$$u_i(\mathbf{x}) = \int_L \left[G_{ij}(\mathbf{x},\mathbf{y}) f_j(\mathbf{y}) + \frac{\partial G_{ij}}{\partial y_k}(\mathbf{x},\mathbf{y}) d_{jk}(\mathbf{y}) \right] d\mathbf{y} \tag{2.35}$$

where the step is represented by a curve L on the half-space and $G_{ij}(\mathbf{x},\mathbf{y})$ is the elastic half-space Green's function. The corresponding stress is the solution to

$$\frac{\partial \sigma_{ij}(\mathbf{x})}{\partial x_j} + \int_L \left[f_i(\mathbf{y})\delta(\mathbf{x}-\mathbf{y}) - d_{ij}(\mathbf{y}) \frac{\partial \delta(\mathbf{x}-\mathbf{y})}{\partial x_j} \right] d\mathbf{y} = 0 \quad \text{for all } \mathbf{x} \text{ in } V \tag{2.36}$$

subjected to the boundary condition

$$\sigma_{ij}(\mathbf{x}) m_j = 0 \quad \text{for all } \mathbf{x} \text{ on } A \tag{2.37}$$

where $\delta(\mathbf{x}-\mathbf{y})$ is the Dirac delta, V is the half-space volume and A is the half-space surface. In this sense, the line force and dipole are considered to

lie slightly beneath the surface of the half-space. In the case of a straight and unbounded step, the displacement associated with the line force varies as $\ln(h/r)$ where r is distance from the step. The displacement of the line dipole varies as h/r. Hence the dipole field is of short-range compared to that of the line force and is negligible except at distances from the step on the order of step height h. In this work the dipole term is neglected unless step interact at close range. At close range the dipole term dominates the interaction between step and causes them to repel energetically [55]. This repulsion is introduced to stop steps from merging. The remainder of this chapter neglects the dipole and deals only with the line force contribution of the elastic field.

2.2.1 Energetic interaction between steps

Consider two step segments A and B on the respective curves L^A and L^B. The elastics field of step A (B) is that of a distributed force monopole f_i^A (f_i^B) measured per unit length the step. Step segments A and B may be located on different islands or may be part of the same island. Let $(\sigma_{ij}^A, \epsilon_{ij}^A, u_i^A)$ and $(\sigma_{ij}^B, \epsilon_{ij}^B, u_i^B)$ represent the elastic fields induced by segments A and B respectively, where σ_{ij} is the stress, $\epsilon_{ij} = \frac{1}{2}(u_{i,j} + u_{j,i})$ is the infinitesimal strain, and u_i is the displacement. The material is considered to be linearly elastic. Considering only these two segments, elastic field is given by the superposition $\sigma_{ij} = \sigma_{ij}^A + \sigma_{ij}^B$, $\epsilon_{ij} = \epsilon_{ij}^A + \epsilon_{ij}^B$ and $u_i = u_i^A + u_i^B$. The strain energy is

$$W = \frac{1}{2}\int_V \sigma_{ij}\epsilon_{ij}\, dV = \frac{1}{2}\int_V \sigma_{ij}^A\epsilon_{ij}^A\, dV + \frac{1}{2}\int_V \sigma_{ij}^B\epsilon_{ij}^B\, dV + \int_V \sigma_{ij}^A\epsilon_{ij}^B\, dV \quad (2.38)$$

where V is the domain of the half-space. The reciprocal theorem was used to obtain the last term. The first two integrals on the right-hand side are the elastic self-energies of the step segments. Due to the singular nature of the elastic fields, these are unbounded and must be regularized in some way.

Regularization of the self-energies is discussed in the next section. The last term is the interaction energy between the segments *i.e.,*

$$E_{int}^{AB} = \int_V \sigma_{ij}^A \epsilon_{ij}^B \, dV = \int_V \sigma_{ij}^B \epsilon_{ij}^A \, dV \tag{2.39}$$

The last expression in (2.39) comes directly from the reciprocal theorem. On using strain-displacement relation in (2.39), one finds

$$\begin{aligned} E_{int}^{AB} &= \int_V \sigma_{ij}^A \, u_{i,j}^B \, dV \\ &= \int_V \left[\left(\sigma_{ij}^A \, u_i^B \right)_{,j} - \sigma_{ij,j}^A \, u_i^B \right] dV \\ &= \int_{\partial V} \sigma_{ij}^A \, n_j \, u_i^B \, dA - \int_V \sigma_{ij,j}^A \, u_i^B \, dV \end{aligned} \tag{2.40}$$

where the last equality comes from application of the divergence theorem and ∂V is the boundary of V. The boundary ∂V consists of the half-space surface and the remote boundary. Using (2.37) and noting that $\sigma_{ij}^A u_i^B$ vanishes at the remote boundary (for finite step segments it decays as the inverse cube of distance from the segments), the first integral in the last equality of (2.40) vanishes. Then using (2.36) and the sifting property of the Dirac delta function, (2.40) becomes

$$E_{int}^{AB} = \int_{L^A} f_i^A(\mathbf{y}) \, u_i^B(\mathbf{y}) \, d\mathbf{y} = \int_{L^B} f_i^B(\mathbf{y}) \, u_i^A(\mathbf{y}) \, d\mathbf{y} \tag{2.41}$$

Hence, the interaction energy is equal to the work done by the monopole of one step segment as it acts through the displacement induced by the other.

2.2.2 Self-energy of a step

Equation 2.41 might also be used to evaluated the self-energy of a step segment, consider A and B to be the same segment. However the result is unbounded because displacement field is unbounded along the segment. This is an artifact of linear elasticity which fails at points in the vicinity of the segment. Assuming

that the linear elastic model is accurate at distances of a_0 and further from the segment, the displacement along the segment (A) might be interpolated as $u_i^A(\mathbf{y}) \approx [u_i^A(\mathbf{y}+a_0\mathbf{n}) + u_i^A(\mathbf{y}-a_0\mathbf{n})]/2$ where $\mathbf{y}$ is a point on the segment and $\mathbf{n}$ is the unit normal at that point. The self-energy can then be approximated

$$E_{self}^A = \frac{1}{2}\int_{L^A} f^A(\mathbf{y})\big[u_i^A(\mathbf{y}+a_0\mathbf{n}) + u_i^A(\mathbf{y}-a_0\mathbf{n})\big]/2\, d\mathbf{y} + \int_{L^A} \psi\, d\mathbf{y} \quad (2.42)$$

The last term was added to account for the energy associated with dangling bonds along the step face and the elastic energy within the core-region near the segment which is missed by linear elasticity and the regularization. The quantity ψ is excess energy per unit length of the segment and is taken to be a constant for simplicity. The elastic cut-off a_0 is taken to be on the order of lattice spacing (or equivalently to the step height of a monolayer island). It is noted that a similar regularization scheme is commonly used in elastic dislocation theory [56].

2.2.3 Self-energy of a square-island

The energies evaluated above can be used to construct the energy of an arbitrarily shaped island composed of piecewise linear segments and, with use of an appropriate kinetic relation, the results can be used to investigate shape transitions of individual islands. As the focus of the current investigation is on the spatial organization of multiple islands, the analysis is simplified by constraining the islands to be square such that they may transform only by changing their sizes and positions. Furthermore it is assumed that the square islands are aligned with the principle directions of the stress induced by the lattice mismatch and remotely applied loads. Hence, according to (2.33), the line force that approximates the elastic field is normal to the steps as shown in Figure 2.6. Forces $f_1 = -h\sigma_{11}$ and $f_2 = -h\sigma_{22}$ where σ_{11} and σ_{22} are the principle stresses of the field $\sigma_{ij}^m + \sigma_{ij}^r$. The interaction energies between steps aligned parallel and orthogonal to each other are provided in the Appendix.

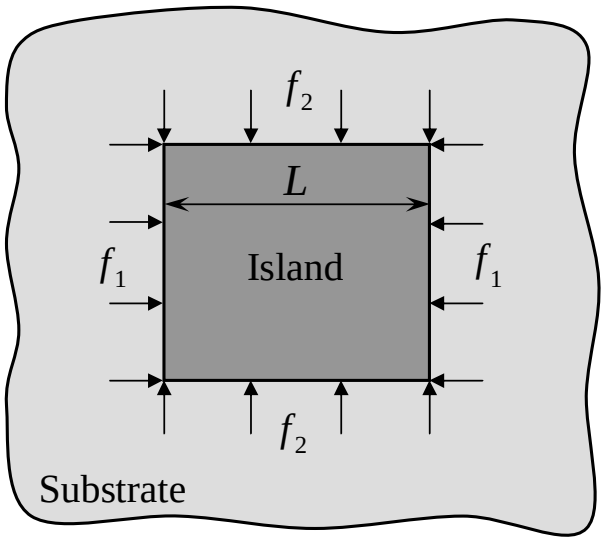

Figure 2.6: Schematic representation of top-view of the square island of width L bounded by steps on a substrate having distributed force monopole f_1 and f_2 acting along its edges.

The self-energy of an island is calculated by summing the energies of the individual step segments, including segment self-energies (A-4) and step-step interaction energies (A-2), (A-3). The self-energy of a square island of size L (Figure 2.6), is calculated as

$$E_{self}\big(L, f_1, f_2\big) = 4\psi L \,+\, \frac{L}{2\,\pi\,G}\Bigg[\big(f_1^2 + f_2^2\big)\Bigg\{(1-2\nu)\,(4-2\sqrt{2}) \\ +\,k\,(1-\nu) \,+\, (1-\nu)\,\ln\left(\frac{a_0^2}{L^2}\right)\Bigg\} \,+\, f_1 f_2\,\nu\,\big\{4\,(\,2-\sqrt{2}\,)\big\}\Bigg] \quad (2.43)$$

where $k = \ln[(1+\sqrt{2})/(-4+4\sqrt{2})]$. For the case of a biaxial stress $f_1 = f_2 = f$ self-energy (2.43) becomes

$$E_{self}\big(L, f, f\big) = 4\psi L \,+\, \frac{L}{\pi\,G}\Bigg[f^2\,(1-\nu)\Bigg\{\,\ln\left(\frac{\alpha\,a_0^2}{L^2}\right)\Bigg\}\Bigg] \quad (2.44)$$

where $\alpha = \exp[k + 4 - 2\sqrt{2}\,]$.

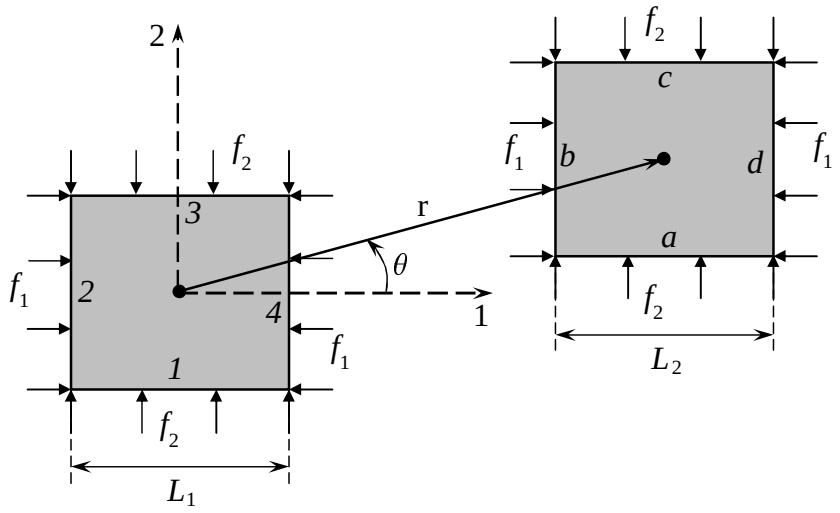

Figure 2.7: Schematic representation of two square islands of size L_1 and L_2 having distributed force monopole f_1 and f_2 along their edges. Origin of the coordinate system is taken at the center of left island. Position vector of center of island at right is $\mathbf{r}$ and its orientation is θ from direction-1.

2.3 Energy of interaction between islands

The self-energy of islands is but one contribution of the total free energy of a system with many islands. As individual steps interact thorough their elastic field, islands will also interact. The interaction energy between islands can be evaluated by adding the interaction energies of the steps of one island with those of the other. Two interacting island are illustrated in Figure 2.7 along with the line forces that determine their elastic fields. Using (A-2) and (A-3) for the step interaction energies and accounting for all combinations of step pairs, the interaction energy between the islands is found to be function of r, θ, L_1, L_2, f_1, and f_2. As the result is lengthly it is not included here. Furthermore, its length makes it undesirable for use in a large scale computation with many islands. Computation of the interaction energy can be accelerated by using an approximation valid for separations r sufficiently larger than the sizes L_1 and L_2 of the islands.

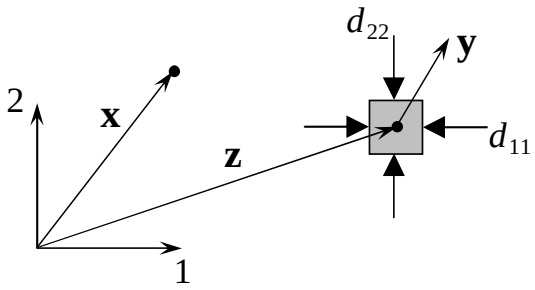

Figure 2.8: In the far-field islands will looks like as illustrated here. Distributed force monopole acting on an island appears to be point dipole d_{11} and d_{22} in far-field approximation as shown.

Far-field approximation

Under the far-field approximation, islands appear as a point-dipoles on an elastic half-space. Consider an island centered at point $\mathbf{z}$ as illustrated in Figure 2.8. Following (2.35), the displacement field of the island at a point $\mathbf{x}$ can be written as

$$u_i(\mathbf{x};\mathbf{z}) = \int_P G_{ij}(\mathbf{x}-\mathbf{z},\mathbf{y}) f_j(\mathbf{y})\, d\mathbf{y} \tag{2.45}$$

where P is the perimeter of the island and vector $\mathbf{y}$ points from the island's center to a point on the perimeter. This field can be approximated at points where $|\mathbf{x}-\mathbf{z}| \gg |\mathbf{y}|$ by expanding Green's function about $\mathbf{y}=\mathbf{0}$,

$$u_i(\mathbf{x}) = G_{ij}(\mathbf{x}-\mathbf{z},\mathbf{0}) \int_P f_j(\mathbf{y})\, d\mathbf{y} + \frac{\partial G_{ij}}{\partial y_k}(\mathbf{x}-\mathbf{z},\mathbf{0}) \int_P f_j y_k\, d\mathbf{y} + \quad \ldots\ldots \tag{2.46}$$

In (2.46) first integral is the net force acting on the island, which vanishes. The approximation becomes

$$u_i(\mathbf{x};\mathbf{z}) \approx \frac{\partial G_{ij}}{\partial y_k}(\mathbf{x}-\mathbf{z},\mathbf{0})\, d_{jk} \tag{2.47}$$

with

$$d_{ij} = \oint f_i y_j\, dl \tag{2.48}$$

where integral is performed over boundary of the island. This is the elastic field of a point dipole d_{jk} on the half-space surface. The corresponding stress

is the solution to

$$\frac{\partial \sigma_{ij}(\mathbf{x};\mathbf{z})}{\partial x_j} - d_{ij}\frac{\partial \delta(\mathbf{x}-\mathbf{z})}{\partial x_j} = 0 \tag{2.49}$$

subject to a traction-free boundary condition of the surface.

Now consider two islands I and J and points $\mathbf{z}^I$ and $\mathbf{z}^J$ and characterized by point dipoles d_{ij}^I and d_{ij}^J respectively. Following (2.40), there interaction energy is given by

$$E_{int}^{IJ} = -\int_V \sigma_{ij,j}^I u_i^J \, dV = -\int_V d_{ij}^I \frac{\partial \delta(\mathbf{x}-\mathbf{z}^I)}{\partial x_j} u_i^J(\mathbf{x}) \, d\mathbf{x} \tag{2.50}$$

Using the sifting property of the Dirac delta function, the interaction energy becomes.

$$E_{int}^{IJ} = -d_{ij}^I u_{i,j}^J(\mathbf{z}^I) \tag{2.51}$$

To evaluate the accuracy of this approximation, consider two islands of same size L and separated by a distance r, a shown in the inset of Figure 2.9(b). Figure 2.9(a) compares the exact and approximation interaction energies versus r/L and Figure 2.9(b) plot the error of the approximation versus r/L. It is found that for separation distances larger than three times the size of islands *i.e.* $r/L \geq 3$, the approximation differs by less than 2.5% from the exact interaction energy. The approximation is found to be sufficient for the calculations done in this work.

2.4 Total free energy and evolution

The total free energy of a system with N islands, numbered 1 through N is given by

$$E = E_0 + \sum_{I=1}^{N} E_{self}^I + \frac{1}{2}\sum_{I=1}^{N} \sum_{\substack{J=1 \\ J\neq I}}^{N} E_{int}^{IJ} \tag{2.52}$$

where E_0 is a constant that depends on the amount of material deposited, but not on the number and configuration of islands, E_{self}^I is the self-energy of I^{th}

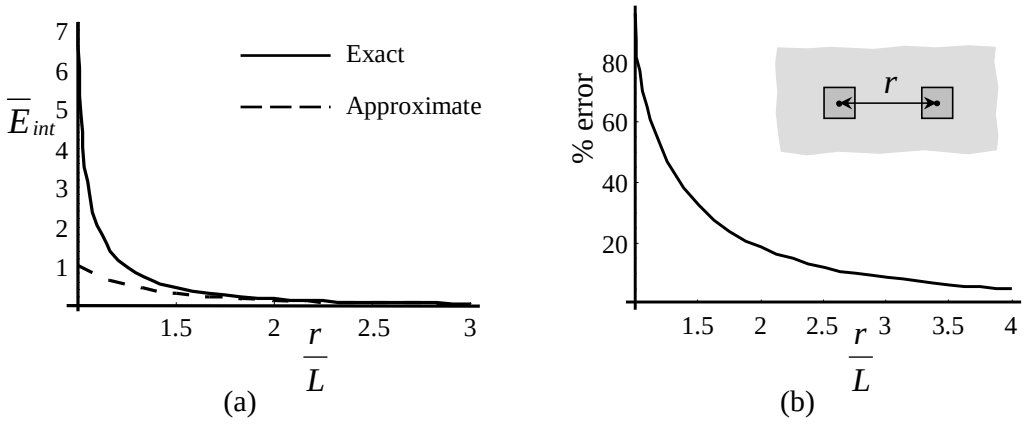

Figure 2.9: The comparison of exact interaction energy with the approximated interaction energy is shown in this plot. In plot (a) the dimensionless exact and the dimensionless approximate interaction energy is plotted together, and plot (b) shows the percentage error $100 \times (E_{exact} - E_{approx})/E_{exact}$. In both cases dimensionless energy, $\overline{E}_{int} = (\pi\, G\, E_{int})/[f^2\, L\, (1-\nu)])$, is plotted with r/L, where E_{int} is the interaction energy of islands, r is the distance between islands shown in the inset of (b) and L is the width of the islands (width of both islands are same).

island given by (2.44) and E_{int}^{IJ} is the energy due to the interaction between I^{th} and J^{th} islands given by (2.51). In the second term on the right of (2.52), one-half is incorporated to abate the counting of same pair of islands twice. Given the configuration at time t, the islands sizes A^I and positions x_i^I at time $t + \Delta t$ are approximated by a forward Euler time step,

$$\begin{aligned} A^I(t+\Delta t) &= A^I(t) + P^I V_n^I \Delta t \\ x_i^I(t+\Delta t) &= x_i^I(t) + v_i^I \Delta t \end{aligned} \tag{2.53}$$

where Δt is the time step, P^I is the perimeter of island I, V_n^I is the growth rate as given by (2.31), and v_i^I is the translational velocity as given by (2.32). The time step Δt is chosen to be small enough for the solution to converge.

2.5 Periodic boundaries

Periodic boundary conditions are used to approximate growth on a substrate that is large compared to the simulation cell. The simulation cell is a square with sides of length S. All of the sides have periodic boundaries conditions such that the periodic images of an island at $\mathbf{x} = \mathbf{x}^I$ are located at $\mathbf{x} = \mathbf{x}^I + pS\mathbf{e}_1 + qS\mathbf{e}_2$ where p and q are integers and $\mathbf{e}_1$ and $\mathbf{e}_2$ form an orthogonal basis in the plane of the substrate surface. Accordingly, if an island leaves the simulation cell, an image island (of the same size) enters the simulation cell on the opposite side.

Interactions between simulation cell islands and periodic image islands are calculated only for the eight cells that neighbor the simulation cell. This is a suitable approximation as the interaction energy between islands decay fairly quickly with separation distance. Calculating the interaction with all periodic images would have significant computational overhead with negligible gain.

Chapter 3

Anisotropy-driven island organization

Consider the earliest stage of film growth on a flat defect-free substrate. As the surface is uniform and there are no preferred nucleation sites, monolayer islands will nucleate randomly on the surface. Suppose then that deposition is stopped and the system is annealed at a temperature high enough to activate mass transport. The configuration at the start of the anneal is a distribution of islands with random positions and sizes. On annealing, the system will evolve towards a configuration of minimum free energy as islands change in size and position. Under conservation of mass, change in island size may occur by coarsening, where large islands grow at the expense of smaller islands, or by a stabilizing mechanism, where small islands grow at the expense of large ones, leading to size uniformity. The later is favorable for achieving a uniform array of self-organized islands.

Figure 3.1 shows a simulation of an isotropic system by Liu *et al* [18]. The domain shown is a single periodic of a bi-periodic configuration, *i.e.* it is unbounded in both the horizontal and vertical directions of the page. Figure 3.1a is the initial configuration of islands and Figure 3.1b is the result of a long-time anneal with the islands held fixed in their initial positions. Mass transport occurs only such that the islands may change in size. In this simu-

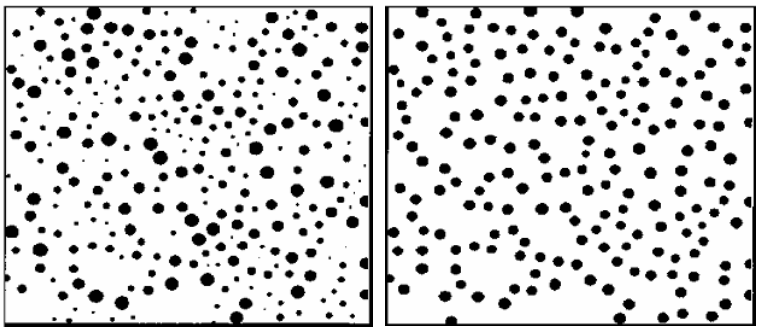

Figure 3.1: Snapshots of simulated island configurations performed by Liu *et al* [18]. (a) The initial configuration with random island sizes and positions. (b) The final converged island configuration from coarsening simulations without island migration, using the initial configuration of (a).

lation, it is apparent that both coarsening and size stabilization mechanisms are operative. Very small islands disappear, while large to moderate size islands achieve a uniform size. The reason for this behavior and the conditions for coarsening versus size stabilization is discussed in the first section of this chapter.

Suppose that the configuration of Figure 3.1b is allowed to evolve further by the translation of islands towards a minimum energy configuration. The system is isotropic, which implies the force monopoles of a step are independent of the step's orientation, in other words $f_1 = f_2 = f$ in Figure 2.7. From (2.48), under isotropic conditions, the elastic field of an square island of length L is that of a dipole $d_{ij} = fL^2\delta_{ij}$ where δ_{ij} is the Kronecker delta. From (2.51) the interaction energy between two islands I and J is given by

$$E_{int} = -fL^2 u^J_{i,i}(\mathbf{z}^I) = f^2 L^4 \frac{\pi(1-\nu)}{2Gr^3} \tag{3.1}$$

where r is the distance between the islands. Note first that energy increases as the separation distance decreases. This implies that the islands tend to repel each other. Also note that the interaction is independent of the relative

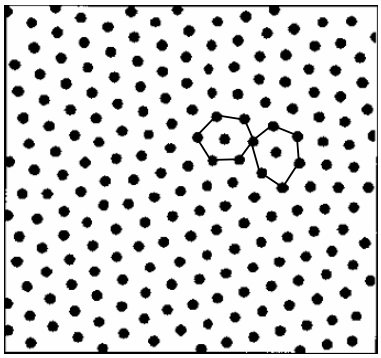

Figure 3.2: The converged island configuration from coarsening simulations with island migration using the initial random configuration performed by Liu *et al* [18] is shown here. Two hexagons are drawn to illustrate a defect arise in case of isotropic force distribution around the islands.

orientation of the islands. Hence in the case of isotropy, islands repel each other uniformly from all directions. Isotropy of the driving force for evolution should lead to an isotropic configuration of islands, in other words, to an array with three-fold symmetry—a hexagonal array. As the evolution begins, islands will locally configure themselves into a hexagonal structure which will then grow in size as islands are incorporated at the periphery. The process is analogous to grain growth. As there is no directional preference, hexagonal arrays form with various orientations over the substrate and a defect, analogous to a grain boundary, will result where two differently oriented merge. This is illustrated in Figure 3.2. Several differently oriented domains are apparent. A structure such as this will either evolve very slowly to decrease the defect density (which comes with an energy cost) or it will be locked in a metastable state that represents a local minimum in free energy.

Self organization under isotropic conditions leads to local ordering. Achieving long-ranged order under isotropic conditions is unlikely as ordered domains form locally with no directional preference. Introducing a directional preference in the form of an anisotropy might help to uniformly orient domains

such that they merge with a defect-free boundary. The effect of anisotropy on long-ranged order is investigated in this chapter. In the present context, anisotropy is considered to arise for the epitaxial mismatch strain or from a remotely applied strain. In order words, the system is anisotropic when the forces $f_1 \neq f_2$ in Figure 2.6. For simplicity, elasticity moduli are assumed to be isotropic.

3.1 Island coarsening versus size stabilization

Coarsening occurs as large islands grow at the expense of smaller ones, producing a progressively smaller number of islands of increasing size. This processes acts against the formation of a regular array, as the system is driven towards that of a single large island. In order to achieve a self organized array, there must be a mechanism that inhibits coarsening.

The free-energy of an island consists of its step-edge energy and an elastic energy arising from distortion of the crystal lattice in the vicinity of the island. For the moment, suppose the elastic energy is negligible and step-edge energy ψ, measured per unit length, is the only contribution to the free energy. The energy of a square island of area A is $4\psi\sqrt{A}$. Now consider two islands of area A and suppose that a small amount of material of area ΔA is transferred from one island to the other. The free energy is

$$E = 4\psi\sqrt{A - \Delta A} + 4\psi\sqrt{A + \Delta A} \approx 8\psi\sqrt{A} - \psi(\Delta A)^2/A^{3/2} \tag{3.2}$$

Noting that the last term on the right-hand size is negative, it is apparent that the energy decreases for small values of ΔA. Hence two islands of the same size are unstable; one island will grow and the other will shrink and ultimately vanish. This demonstrates that if there is in fact a mechanism that stabilizes islands, it must arise from the elastic energy.

Including the elastic energy, the free energy of a square island is given

by (2.44). Again considering two islands, one of area $A + \Delta A$ and the other of area $A - \Delta A$, the total free energy is

$$E = 4\psi\sqrt{A - \Delta A} + \frac{f^2(1-\nu)\sqrt{A-\Delta A}}{\pi G}\ln\left(\frac{\alpha\, a_0^2}{A-\Delta A}\right) + 4\psi\sqrt{A + \Delta A} + \frac{f^2(1-\nu)\sqrt{A+\Delta A}}{\pi G}\ln\left(\frac{\alpha\, a_0^2}{A+\Delta A}\right)$$

where $\alpha \approx 4.7022$. For small ΔA the total energy is approximately

$$\begin{aligned} E &\approx 8\psi\sqrt{A} + \frac{2f^2(1-\nu)\sqrt{A}}{\pi G}\ln\left(\frac{\alpha\, a_0^2}{A}\right) \\ &- \frac{(\Delta A)^2}{A^{3/2}}\left[\psi + \frac{f^2(1-\nu)}{4\pi G}\ln\left(\frac{\alpha\, a_0^2}{A}\right)\right] \end{aligned} \tag{3.3}$$

According to (3.3), it is evident that if

$$\psi + \frac{f^2(1-\nu)}{4\pi G}\ln\left(\frac{\alpha\, a_0^2}{A}\right) < 0 \tag{3.4}$$

the free energy increases as mass is transferred from one island to the other. Equation (3.4) defines a critical size of islands which resist coarsening, that is, islands of size

$$\sqrt{A} > L_{cr} = a_0\alpha^{1/2}\exp\left(\frac{2\pi G\psi}{f^2(1-\nu)}\right) \tag{3.5}$$

are stabile against coarsening. In the case of no lattice mismatch and no remotely applied load ($f = 0$), the critical size becomes unbounded, which is consistent with the observation of (3.2). The critical size decreases as the lattice mismatch or applied load is increases. Consider for example a Ge_xSi_{1-x} film on Si where the lattice mismatch varies from $\epsilon_m = 0\%$ to -4% as the Ge fraction x varies from 0 to 1. Step excess energies are on the order of 0.1 eV/atom [57, 58], or $\psi \sim (0.1/a_0)$ eV where a_0 is the lattice spacing. Taking this value for ψ, $a_0 = 5.65$ Å, shear modulus $G = 40$ GPa, Poisson ratio $\nu = 0.25$, step height $h = a_0/2$ and force monopole $f = 2h\epsilon_m G(1+\nu)/(1-\nu)$, the critical size is calculated as $L_{cr} = 80.12$ nm for $\epsilon_m = -0.04$ and $L_{cr} = 2.07$ μm for $\epsilon_m = -0.03$. Over a modest range of lattice mismatches, the

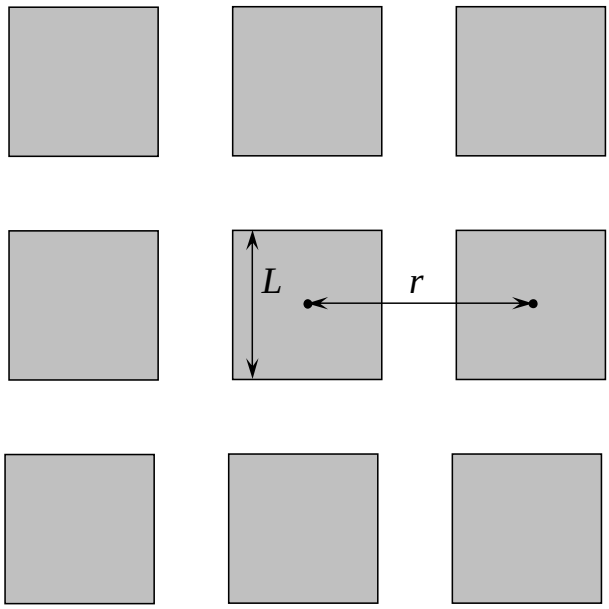

Figure 3.3: A square array of islands of size L separated by distance r on a substrate is shown.

critical size of an island varies from a few nanometer to several microns. In the case of multiple islands of various sizes, whether an island grow or shrinks depends on its chemical potential relative to the average chemical and not necessarily on the critical size. It is *not* the case that islands larger than the critical size grow while small one shrink. The critical size does, nevertheless, establish a minimum density of stable islands for a given amount of deposited material. Let Θ be the fractional coverage of film atoms on the substrate, and consider a square array of island of size L and separation distance r as shown in Figure 3.3. The fractional coverage is $\Theta = L^2/r^2$. By (3.5), the condition for the array to be stable is $L = r\sqrt{\Theta} > L_{cr}$, or

$$r > L_{cr}/\sqrt{\Theta} = a_0 \left(\frac{\alpha}{\Theta}\right)^{1/2} \exp\left(\frac{2\pi G\psi}{f^2(1-\nu)}\right) \tag{3.6}$$

For GeSi on Si with $\epsilon_0 = -0.04$, the minimum separation distance is 801.2 nm for a coverage $\Theta = 0.01$ and 179.2 nm for a coverage $\Theta = 0.2$. Hence engineering of the coverage and the lattice mismatch could be used to manipulate

the configuration of an island array and furthermore a wide range of stable configurations are possible.

Finally, it is noted that island interaction were omitted in this calculation. Island interactions where found to very weakly favor coarsening, but the effect was found to be negligible compared to the self-energy of the islands.

3.2 Effect of anisotropy on driving forces

As noted previously, an isotropic non-coarsening system will tend to evolve to locally ordered domains of hexagonal island arrays, separated by grain-boundary-like defects. Anisotropy introduces orientation dependence that could give rise to long-range order, as desired for many device applications. Anisotropy implies that the force monopole of a step depends on its orientation. According to (2.33) this implies that the principle stresses associated with the lattice mismatch and/or remote loading differ. An anisotropy in the mismatch can arise when the crystal structure of either the island or substrate is tetragonal.

It was shown that under isotropic conditions islands repel each other uniformly from all directions. Consider the interaction between two islands under anisotropic conditions. The islands are taken to square and of the same size L. Their sides are aligned with the principle directions of the residual stress (mismatch plus remote). Hence the force monopoles f_1 and f_2 of an islands are normal to its steps as shown in Figure 2.7. From (2.48) the elastic field of each island is approximated by a dipole $d_{11} = f_1 L^2$, $d_{22} = f_2 L^2$, and $d_{12} = d_{21} = 0$. The ratio $\zeta = d_{11}/d_{22} \, (= f_1/f_2)$ characterizes the anisotropy. An anisotropy ratio $\zeta = 1$ corresponds to the isotropic case. Large values of ζ or $1/\zeta$ implies large anisotropies. Using (2.47) in (3.4), the interaction energy

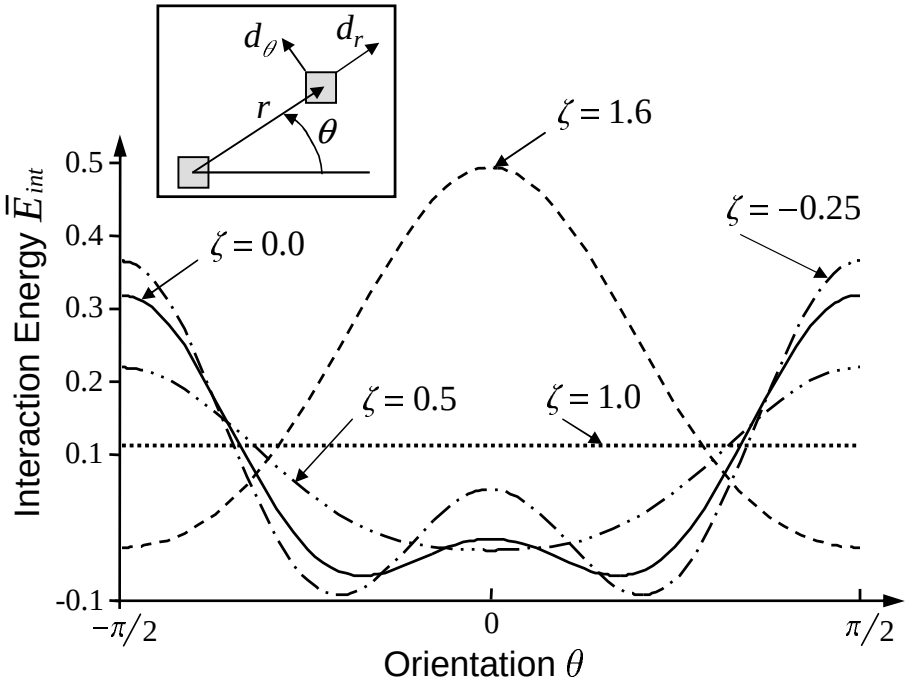

Figure 3.4: Plots of normalized interaction energy, $\overline{E}_{int} = E_{int}Gr^3/d_{22}^2$ of two islands (given by equation 3.7) versus orientation defined in the inset for several anisotropy values (ζ) is presented. G is shear modulus, d_{22} is the dipole acting on islands, r is the distance between islands and Poisson's ratio $\nu = 0.3$.

between the islands is calculated as

$$E_{int} = \frac{d_{22}^2}{16\pi G r^3}\left\{4(1+\zeta^2) - \nu[3+\zeta(2+3\zeta)] - 12(1-\nu)(1-\zeta^2)\cos 2\theta + 15\nu(1-\zeta)^2\cos 4\theta\right\} \quad (3.7)$$

where r is the separation distance and θ is the relative orientation of the islands as shown in the inset of Figure 3.4. In (3.7), G is shear modulus and ν is Poisson ratio. Observe that interaction depends on the orientation of the islands. The character of the interaction depends on the factor in {} in Equation (3.7) while is plotted in Figure 3.4 for various anisotopies. If the factor is positive, the energy decreases with separation distance and the islands repel. If the factor is negative, the energy decrease as separation distance decreases and the islands attract. As shown in Figure 3.4, whether the island

attract or repel depends on both the anisotropy and their orientation. Note also that for isotropy ($\zeta = 1$) the island repel uniformly for all orientations. Figure 3.4 also illustrates the tendency for the orientation to change. Consider for example $\zeta = 1.6$ with an initial orientation of $\theta = \pi/4$. Energy decreases as θ increases towards $\pi/2$, which is the stable equilibrium orientation of this anisotropy. The orientation $\theta = 0$ correspond to an unstable stationary state where the orientation will change in either the clockwise or counterclockwise sense. It is also observed from Figure 3.4 in the anisotropic case ($\zeta \neq 1$) there is either one or two stable equilibrium orientations. When two stable orientations exists, they are generally nonorthogonal. They are orthogonal only for the case of $\zeta = -1$. The strength by which the islands are driven to reorient is scales with the slope of curves in Figure 3.4. It is noted that orientational driving force is small when the islands are near a stationary orientation. The tendency for island to reorient also decreases as the anisotropy approaches $\zeta = 1$.

The tendency for the two-island system to evolve can be understood in terms of repulsive and orientational driving forces

$$d_r = -\frac{\partial E_{int}}{\partial r} \quad \text{and} \quad d_\theta = -\frac{\partial E_{int}}{\partial \theta} \tag{3.8}$$

respectively. If $d_r > 0$ ($d_r < 0$) the island tend to repel (attract) each other and if $d_\theta > 0$ ($d_\theta < 0$) the islands tend to reorient with increasing (decreasing) θ. Stationary states correspond to $d_r = d_\theta = 0$. Figure 3.5 plots the character if the interaction is a function of θ and ζ. Shaded regions denote attractive configurations and unshaded regions denote repulsion. The solid and dashed line plot stationary orientations ($d_\theta = 0$). Solid line represent stable orientations when dashed lines represent unstable orientations. Note that by symmetry, a system of anisotropy $\zeta = a$ is equivalent to one of anisotropy $\zeta = 1/a$. They differ only by a 90° rotation. Hence further discussion will be limited to anistropies $-1 \geq \zeta \geq 1$ which includes all possible systems. Phys-

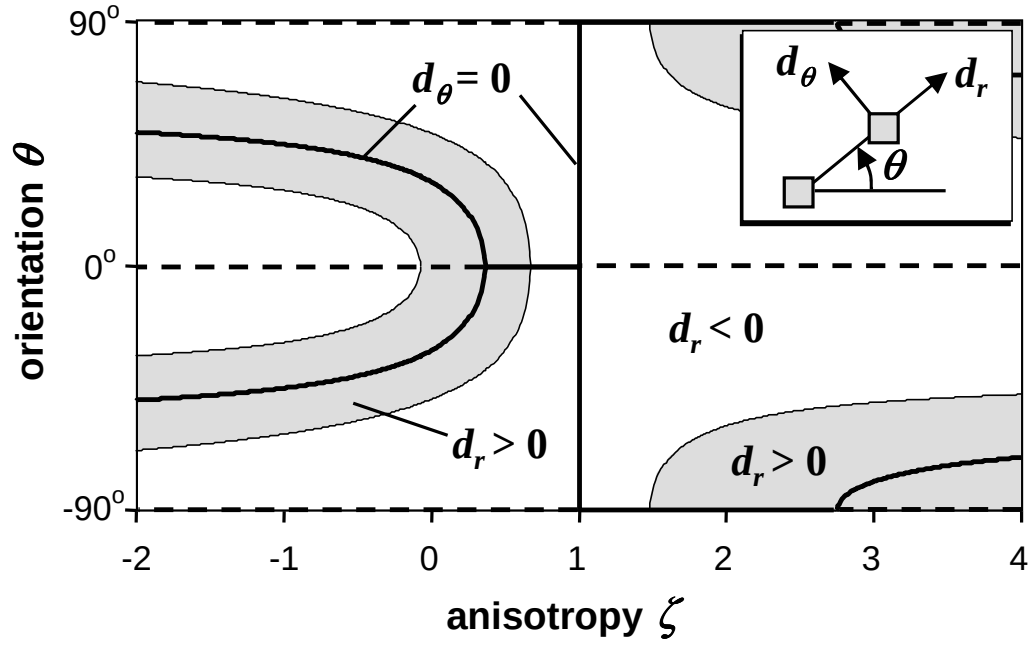

Figure 3.5: Plot of interaction between two islands with orientation θ. The solid lines plot stable equilibrium orientations θ versus anisotropy ζ. The dashed lines plot unstable stationary states. Shaded regions denote states where the islands attract each other while unshaded region denote state where they repel. The inset shows the orientation of the radial (d_r) and orientational (d_θ) driving forces on an island. The Poisson's ratio is $\nu = 0.3$.

ically speaking, the anisotropy increases from $\zeta = 1$ to $\zeta = -1$. Changing ζ from -1 to $-\infty$ is equivalent to changing it from -1 to 0. Likewise changing ζ from 1 to ∞ is equivalent to changing it from 1 to 0. The apparent jump in the character of the interaction from $\zeta = 1 - \varepsilon$ to $1 + \varepsilon$ is misleading. While the stable orientation abruptly changes from vertical ($\theta = \pm 90°$) to horizontal $\theta = 0$, the driving force d_θ changes continuously with ζ; it vanishes at $\zeta = 0$. The abrupt change in character is accompany by a very small driving force. Hence a significant difference is *not expected* between an isotropic system and one with a small level of anisotropy.

As anisotropy is increased ($\zeta < 1$) from the isotropic case, a single

orientation becomes stable while the strength of the orientational driving force (not discernable from Figure 3.5) increases from zero. For anisotropies $\zeta > \nu + \sqrt{(1-\nu)(1-2\nu)/2}$ ($\zeta > 0.67$ for $\nu = 0.3$), the islands tend to repel at their stable orientations. There is a bifurcation at $\zeta = (6\nu - 1)/(1 + 4\nu)$ ($\zeta = 0.36$ for $\nu = 0.3$), where for larger anisotropies two generally nonorthogonal orientations become stable. The islands tend to attract at both of these orientations. It is noted that a behavior similar to that of Figure 3.5 has been reported by Kukta *et al.* in the case of adatoms under anisotropic conditions.

The evolution of two islands from an arbitrary starting configuration can be quite rich in behavior. Consider for example the case of $\zeta = 0$ which islands oriented at $\theta \approx 89°$. At this state the island will simultaneously grow in separate and reorient with decreasing θ. As the islands separate, the driving forces for both separation and reorientation decrease, hence their velocities will decrease. Once the orientation angle θ reaches a critical value, the islands will begin to attract. As separation distance decreases both components of the driving force will increase and the islands will accelerate towards their stable orientation. Recall that the model is valid only for islands that are sufficiently far appear for the dipole approximation to hold. Furthermore repulsive surface step dipoles that dominate close-range interactions between steps were omitted in the model. Hence the model cannot predict if the islands merge or begin to repeal at close distances to ultimately achieve an equilibrium separation. Calculations have been done on shape transitions of a single rectangular island under anisotropic conditions by Li *et al.* [59]. They find that square islands are stable for small levels of anisotropy, while for large anisotropies they transform to a rectangular shape. Hence whether or not the islands merge, the resulting structure will be an elongated mass, consisting of either two slightly separated islands or a single elongated island. To avoid complexities associated with the close-ranged interaction, a near-field repulsion is introduced to stop

the islands from combining. This achieves a configuration representative of an elongated mass without having to depart from the constraint of square islands. Furthermore, without adding the near-field repulsion, the driving force becomes singular as the separation between islands vanishes. This behavior is nonphysical and certainly cannot be handled numerically.

3.3 Evolution of Many-Island Systems

Evolutions of multiple island systems with various anisotropies are considered in this section. Simulations are done as described in Chapter 2. The initial configuration is taken to be a random distribution of islands—island sizes and positions are both random. The systems are annealed, such that evolution occurs under the constraint of fix mass of the islands. Simulations were carried out until equilibrium was achieved. Results are shown in Figure 3.6. Figures 3.6(b)-3.6(f) respectively are the resulting equilibrium configurations for anisotropies $\zeta = 1$ (isotropic), $\zeta = 0.8$, $\zeta = 0.5$, $\zeta = 0$, and $\zeta = -0.25$ where $\zeta = f_1/f_2$. The initial configuration for each of these simulations is as shown in Figure 3.6(a). In terms of dimensionless parameters, each of the simulations shown correspond to the case of

$$\frac{2\pi\psi G}{f_2^2(1-\nu)} = 0.8354 \tag{3.9}$$

with $S/h = 2000$ where S is the simulation cell size, $a_0/h = 2$ where a_0 is the cut-off radius, coverage $\Theta = 0.02$, island sizes vary from $5h$ to $50h$, and Poisson ratio $\nu = 0.3$. Using these values in (3.5) the critical islands size for coarsening is $L_{cr} = 10h$. Hence islands larger than this value will tend to resist coarsening.

The isotropic case, Figure 3.6(b), is similar to the result obtained by Liu *et al* [18] (compare Figure 3.2). As island interactions are independent of orientation, the minimum energy configuration is a hexagonal array of islands.

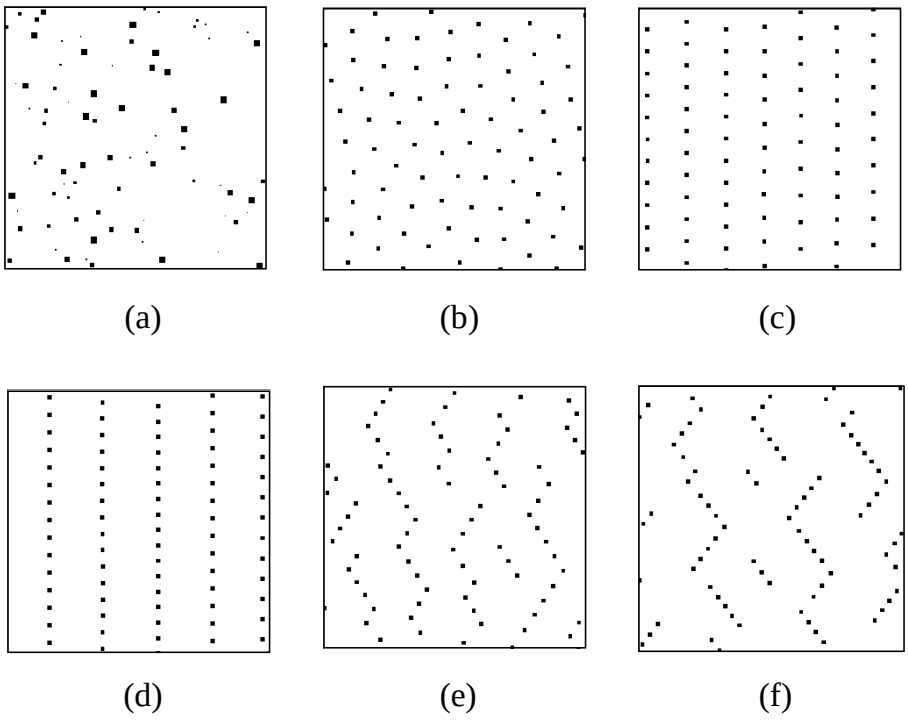

Figure 3.6: (a) Initial size and positions of all islands are shown. Also the equilibrium configurations of different force distribution (b) $\zeta = 1.0$, (c) $\zeta = 0.8$, (d) $\zeta = 0.5$, (e) $\zeta = 0.0$, and (f) $\zeta = -0.25$ are shown.

Domains of various orientations form locally and expand to meet at grain-boundary-like defects. Once the hexagonal domains are established a process analogous to grain growth occurs as islands on the boundaries jump from one domain to another. This occurs until the entire system becomes either a single hexagonal array or a metastable state with multiple hexagonal domains. The equilibrium configuration and in particular the number of hexagonal domains remaining at equilibrium, is largely dependent on the initial conditions. In practice, the initial condition cannot be controlled as island nucleation is largely a random process. Hence, if a single uniform array is desired, growth under isotropic conditions would be ineffective. It is noted that uniform arrays are less likely to form in practice than they do in these simulations because the finite size of the periodic simulation cell limits the number of differently oriented hexagonal domain that initially form.

For the case of $\zeta = 0.8$, Figure 3.6(c), islands are driven to align along a single direction. It is apparent from the Figure 3.5 that for $\zeta = 0.8$ the islands have only one orientation preference, at $\theta = 0$ so the islands aligned vertically. The Figure 3.5 also indicates that the islands repel each other in all directions which is reflected in the snapshots of the progress of the evolution shown in Figure 3.7(a). As the evolution begins the islands align themselves in their preferred orientations. While the islands move towards their stable locations they repel other islands. The repulsion between islands increase as they come closer by addition of other islands in a column already formed. This repulsive character of islands limits the separation between two islands. Once the separation between the islands reached this limit further addition of islands are not allowed. This phenomenon results in the formation of many columns of islands. The islands in consecutive columns do not align in horizontal direction which results the configuration into a domain of rectangular arrays with different orientations. A modest anisotropy, as in this simulation, provides a

unidirectional arrangement of islands and eliminates the grain-boundary-like defects observed in the isotropic case.

For the case of $\zeta = 0.5$, Figure 3.5 shows that islands have one preferred orientation at $\theta = 0$ but they attract each other at this orientation. As mentioned earlier a near-field repulsion is introduced to keep the islands from merging, thus obtaining an elongated structure without departing for the constraint of the islands being square. The repulsion is set to keep the islands a small distance apart as compared to the step height. The result of the simulation for $\zeta = 0.5$ is shown in Figure 3.6(d). It is apparent from the plot of Figure 3.5 that the islands attract each other over a range of orientations (*i.e.* from -31.1° to 31.1° for $\nu = 0.3$) including their preferred orientation. This behavior is also observed in the snapshots of progress of the simulation, Figure 3.7(b). First snapshot shows the initial random configuration of islands. It is observed that when the evolution starts the islands that are close to other islands begin to align in a vertical line. This behavior is shown in the fourth snapshot of the Figure 3.7(b). These small groups of islands then align with the nearest group as time proceeds. This behavior continues till all islands align along vertical lines. This tendency is shown in the consecutive snapshot in the Figure 3.7(b).

In cases of larger levels of anisotropy, ($\zeta = 0$ and $\zeta = -0.25$ are considered), two preferred orientations are observed—one at an orientation between $-\pi/2$ and 0 and the other at an orientation between 0 and $\pi/2$. In the case of $\zeta = -0.25$ orientations are -36.8° and 36.8°. Also the islands attract as well as repel each other over non-equilibrium orientations. The islands attract at orientations from 15.5° to 53.7° and -15.5° to -53.7° while they repel elsewhere. Under the influence of two preferred orientations the islands will form several zigzag lines and the angle between adjacent lines will be either 73.6° or 106.4°. The snapshots of progress of the simulation for $\zeta = -0.25$ is shown in

the Figure 3.7(c). The islands are found to organize in a zigzag pattern, such that rows of islands shift in orientation between the two stable orientations. Similar patterns were observed in recent experiments [60–62]. Zigzag patterns were also observed by Gao *et al.* [20] in simulations of phase segregation in binary thin films. Within a zigzag row, pairs of islands on either side of the shift in orientation interact at orientations that are not of minimum free energy. Hence the zigzag pattern comes with an energy cost, and it is expected that islands aligned in a single orientation are of lower energy. However there is an energy barrier for a zigzag row to transform into a straight row, as islands must translate through high-energy orientations. This intuition applies only to a single line of islands. The elastic interaction between adjacent lines will favor the zigzag pattern, as a larger number of islands that lie on different lines will be along a low energy orientation than in the case of a colony of straight lines. If the separation between adjacent lines is small compared the size of the zigzag pattern of a single line, the colony of zigzag lines may have lower energy than the colony of straight lines. Gao et al [20] found this to occur in the case of a binary monolayer. However they do address the individual energy contributions to say that it is the interaction between adjacent lines that make zigzag lines in a herringbone pattern energetically favorable.

This investigation shows that the elastic energy of islands introduces a mechanism that stabilizes the islands from coarsening and helps them to achieve a uniform array. More importantly this investigation demonstrates that by introducing the anisotropy it is possible to obtain strongly selforganized island arrays. It is shown that the anisotropy, which may be changed by the change in epitaxial system and the remote load, plays an important role in the self-organization, and stability of epitaxial islands. By the proper selection of these parameters it is possible to achieve a range of anisotropies which could lead to varieties of arrangement from straight arrays to zigzag

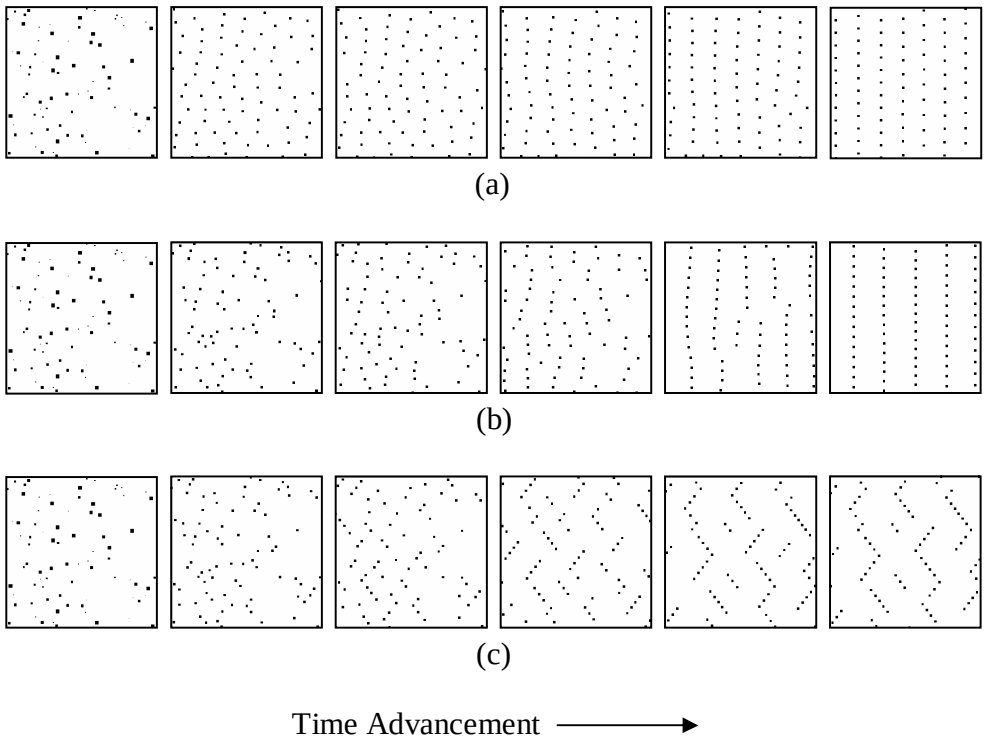

Figure 3.7: The Snapshots of the simulation for (a) $\zeta = 0.8$, (b) $\zeta = 0.5$, and (c) $\zeta = -0.25$ with the advancement of time is shown. The first and the last snapshots shows the initial and the final configurations.

lines at any desired angle. The devices in microelectronic and optoelectronic applications requires a uniform and regular arrangement of quantum dot arrays. The anisotropy may have potential application in the manufacturing of these devices.

Chapter 4

Effect of Dislocations on the Organization of Islands

Anisotropy influences the relative positions of islands on a substrate but it does not control the absolute positions. Islands may form a particular pattern but the pattern can be located anywhere on the substrate. Furthermore, the variety of patterns possible by exploiting anisotropy is rather limited. Formation of wider range of patterns and positioning of islands at specific sites can be achieved by introducing some inhomogeneity in the substrate. This chapter addresses organization controlled by natural inhomogeneities and in particular lattice dislocations within the substrate.

The type of inhomogeneity of interest is one that produces a nonuniform strain field on the surface of the substrate. Consider the interaction energy between an island I and a nonuniform strain field caused by a defect D within the substrate. Following (2.40), the interaction energy is given by

$$E_{int}^{ID} = -\int_V \sigma_{ij,j}^I u_i^D \, dV \tag{4.1}$$

where superscripts I and D refer to the elastic fields of the island and defect respectively. Introducing (2.49) for the elastic field of the island yields

$$E_{int}^{ID} = -d_{ij}^I u_{i,j}^D(\mathbf{z}^I) \tag{4.2}$$

where d_{ij}^I is the island's dipole and $\mathbf{z}^I$ is the island's position. From (4.2) it is clear that if the defect field u_i^D depends on position, the interaction energy also depends on position. It is also observed that the energy is reduced if the island moves in the direction of the energetic driving force

$$d_k^{ID} = -\frac{\partial E_{int}^{ID}}{\partial z_k^I} = d_{ij}^I u_{i,jk}^D(\mathbf{z}^I) \tag{4.3}$$

The preferred minimum energy site of the island is determined by the u_i^D. Consider the case $d_{ij}^I = fL^2\delta_{ij}$. Equation (4.3) becomes

$$d_k^{ID} = fL^2 u_{i,ik}^D(\mathbf{z}^I) = fL^2\epsilon_{ii,k}^D(\mathbf{z}^I) \tag{4.4}$$

where ϵ_{ij}^D is the strain field of the defect and ϵ_{ii}^D is the dilatational strain on the substrate surface. The case $f > 0$, corresponds to the situation where the island is compressed onto the substrate to achieve a coherent interface (see Figures 2.3 and 2.6); the island behaves as a dilatational dipole. According to (4.4), such an island is driven to move from regions of low dilatational strain to regions of higher dilatational strain. Physically, the island wants to move to a site where the lattice of the substrate is expanded to a level closer to its undeformed lattice. The island will come to rest at a site where the defect's dilatational strain is maximum. The chemical potential at such a site is generally lower than sites of low dilatational strain. Hence once the island comes to rest, it will tend to grow at the expense of islands at high-energy sites. Conversely for the case of $f < 0$, where the island is stretched onto the substrate, the island will come to rest at a site where the defect's dilatational strain is minimum. It is noted that f is assumed to be a constant, in other words independent of the islands position. In light of (2.33), one might consider it to change in response to the defect's elastic field according to $f_i = -h(\sigma_{ij}^D + \sigma_{ij}^m + \sigma_{ij}^r)n_j$ where σ_{ij}^D is the defect's stress field. If the defect's field scales with lattice spacing (for example the Burger's vector of a

dislocation), the correction is on the order of the square of lattice spacing or equivalently h^2. As the island's elastic field is approximated to first order in h, this correction should be omitted for consistency. The physical limitation of the model is that the strain field on the surface that is produced by the defect should be much smaller than that of the lattice mismatch plus remote loading.

Defects provide locations for preferential growth of the islands by modulating the strain field over the substrate. One such defect is a dislocation buried underneath the surface. Arrays of these dislocation lines are readily achieved in lattice mismatched epitaxial systems. Consider a film of material A grown on a substrate of material B and suppose the film grows layer-by-layer to a fairly large thickness. In the case of a lattice mismatch, strain energy builds in the system as film thickness increases. It is well-known and understood theoretically that once the film reaches some critical thickness, it becomes energetically favorable for the film-substrate interface to loose registry along discrete lines, call misfit dislocations [32–35]. Misfit dislocations relax an amount of the mismatch strain stored in the system. Directly above the dislocation line the strain is relieved most efficiently, while the strain relief is not as effective far from dislocations [29]. Systems where the critical thickness is exceeded by a sufficient amount tend to exhibit dislocation networks, often in the form of two sets of parallel lines oriented orthogonal to each other, appearing as a rectangular grid. With a network of dislocations at the interface between the film A and substrate B, the film surface will become nonuniformly strained due the elastic fields of the indivdual dislocations. If the film is then used as a substrate to grow another material C, there will be preferred sites for islands to form. Ordering of islands on a substrate having a buried dislocation network has been observed in metal epitaxy [28] as well as in the semiconductor epitaxy [29–31, 63].

4.1 Misfit dislocations

In an epitaxial system where the lattice parameter of the film differs from that of the substrate by a modest amount, the film grows with the extensional strain that is required in the plane of the interface to retain perfect atomic registry of the film with the substrate. After certain thickness of film deposition the film-substrate interface looses the atomic registry at some locations thus form misfit dislocations. A misfit dislocation is a linear crystallographic defect, or irregularity, along the film-substrate interface. Misfit dislocations compensate for differences in the lattice constants by concentrating the misfit in one-dimensional regions – the dislocation lines. Between the dislocation lines the interface is coherent. Generally speaking, the formation of misfit dislocation rows at interphase boundaries is either desirable or deleterious, from an applications viewpoint, depending on the roles of the films and interphase boundaries in applications of heteroepitaxial systems. The formation of misfit dislocations may be desirable as it results in a (partial) compensation for misfit stresses in the film. If the properties of an interphase boundary are exploited, the formation of misfit dislocation rows commonly is undesirable, since the misfit dislocation cores formed violate the pre-existing ideal (coherent) structure of the interphase boundary. This investigation focus on the properties of film so the formation of misfit dislocation is desirable for this investigation. The misfit dislocations are more or less lattice dislocations of the crystals and it can be visualized as the termination of a plane of atoms in the middle of a crystal, as shown in Figure 4.1. Misfit dislocations can be characterized by the Burgers vector which gives information about the orientation and magnitude of the dislocation.

The Burgers vector of a misfit dislocation vector, specified by Miller indices, that quantifies the difference between the distorted lattice around the

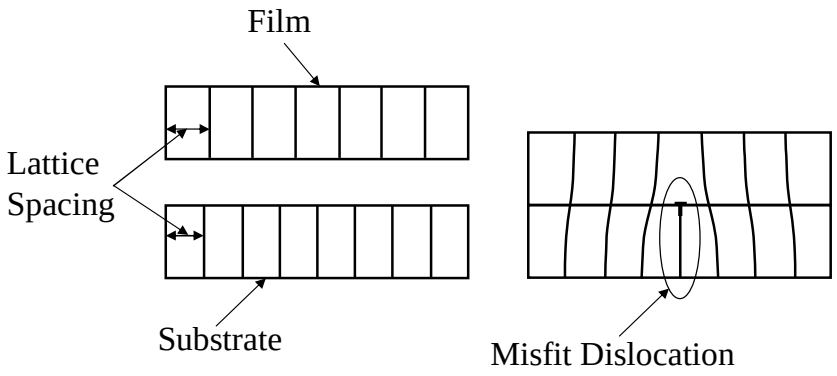

Figure 4.1: Representation of misfit dislocation develop during an epitaxial growth.

dislocation and the perfect lattice. Equivalently, the Burgers vector denotes the direction and magnitude of the atomic displacement that occurs when a dislocation moves. The Burgers vector of a misfit dislocation can be determined as follows: trace around the end of the dislocation plane to form a closed loop (Figure 4.2(a)). Record the number of lattice vectors traveled along each side of the loop (shown here by the numbers in corresponding direction). In a perfect lattice (Figure 4.2(b)), trace out the same path, moving the same number of lattice vectors along each direction as before. This loop will not be complete, and the closure failure is the Burgers vector.

4.2 Elastic field of a misfit dislocation

Island nucleation may be influenced by the strain field of a misfit dislocation network of a relaxed Si_xGe_{1-x} layer. The misfit associated with these dislocations extends into the epitaxial layer and induces a regular variation in the lattice constant at the surface. The residual strain, albeit small, is sufficient to cause preferential nucleation of the Ge dots along the misfit dislocation. Each dislocation has an associated strain field which translate into a lattice constant variation on the surface.

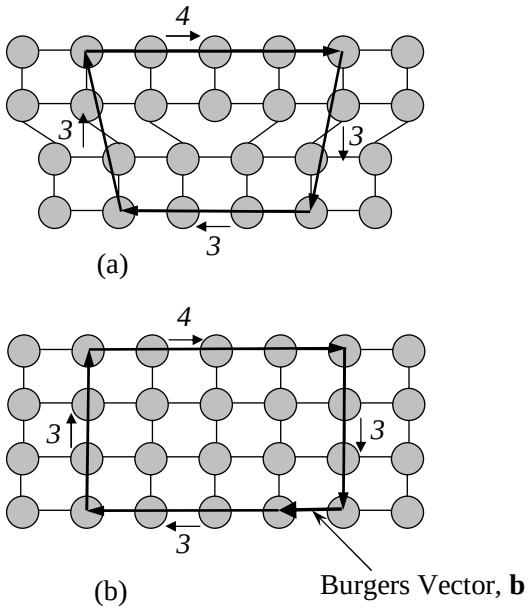

Figure 4.2: Two-dimensional primitive square lattice (a) with dislocation and (b) without dislocation is shown here.

Consider an edge dislocation with Burgers vector **b** having components b_x and b_y in an unbounded homogeneous and isotropic elastic solid. The plane strain field is considered here. The origin of the coordinate system is taken to coincide with the location of the core of the dislocation. The elastic field of this system can be expressed in term of complex variables, according to which the stress components and displacement components are represented in terms of two functions φ and ϕ of $\zeta = x + iy$, which are analytic over the region of the body, except at isolated points or lines, as

$$\begin{aligned} \frac{1}{2}\left(\sigma_{xx} + \sigma_{yy}\right) &= 2\,\mathrm{Re}[\varphi'(\zeta)] \\ \frac{1}{2}\left(\sigma_{yy} - \sigma_{xx}\right) + i\sigma_{xy} &= \bar{\zeta}\,\varphi''(\zeta) + \phi'(\zeta) \end{aligned} \tag{4.5}$$

The overbar denotes complex conjugate. The values of functions φ and ϕ for

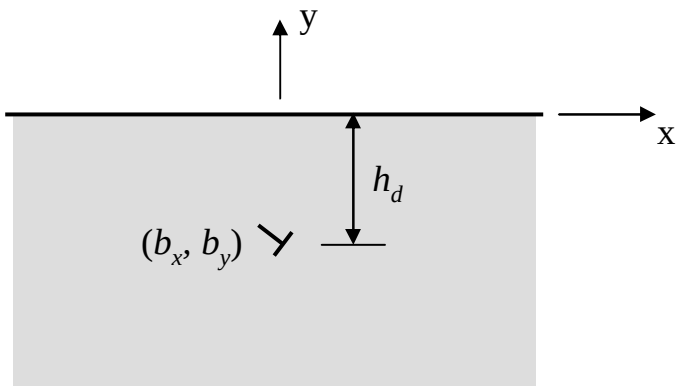

Figure 4.3: An edge dislocation whose Burgers vector is having components b_x and b_y and located at the depth of h_d in a traction-free half space.

the dislocation located at $x = 0$, $y = -h_d$ are

$$\begin{aligned} \varphi'(\zeta) &= \frac{ib\,G}{4\,\pi\,(1\,-\,\nu)\,(\zeta\,+\,ih_d)} \\ \phi'(\zeta) &= -\frac{G}{4\,\pi\,(1\,-\,\nu)}\left[\frac{i\bar{b}}{(\zeta\,+\,ih_d)} + \frac{b\,h_d}{(\zeta\,+\,ih_d)^2}\right] \end{aligned} \tag{4.6}$$

where G is the shear modulus and ν is the Poisson's ratio.

For an edge dislocation in a half-space, as shown in Figure 4.3, the elastic field can be obtained from the field represented by (4.6) by adding the appropriate nonsingular elastic field to ensure the traction free boundary condition on the surface $y = 0$. The corresponding complex function [64] becomes

$$\varphi'(\zeta) = \frac{G}{4\,\pi\,(1\,-\,\nu)}\left[\frac{ib}{\zeta\,+\,ih_d} - \frac{i\bar{b}\,(\zeta\,+\,ih_d)}{(\zeta\,-\,ih_d)^2} - \frac{i(b\,-\,\bar{b})}{\zeta\,-\,ih_d}\right] \tag{4.7}$$

The expression for $\phi'(\zeta)$ is not calculated here because $\varphi(\zeta)$ and $\phi(\zeta)$ are uniquely related throughout the elastic half-space [65]. As a result, all components of stress and displacement can be represented in terms of a single analytic function of ζ throughout the half-space according to

$$\begin{aligned} \sigma_{yy}\,-\,\sigma_{xx} &= \varphi'(\zeta)\,-\,\varphi'(\bar{\zeta})\,+\,(\zeta\,-\,\bar{\zeta})\,\overline{\varphi''(\zeta)} \\ \sigma_{xx}\,+\,\sigma_{yy} &= \varphi'(\zeta)\,+\,\varphi'(\bar{\zeta})\,+\,2\,\overline{\varphi'}(\zeta)\,-\,(\zeta\,-\,\bar{\zeta})\,\overline{\varphi''(\zeta)} \end{aligned} \tag{4.8}$$

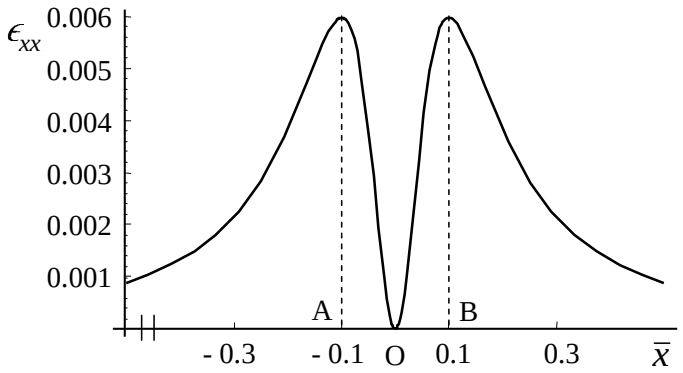

Figure 4.4: Plot of strain against the normalized distance along x-direction, $\bar{x}$ along the substrate surface. The distance is normalized with magnitude of the Burgers vector *i.e,* $\bar{x} = x/b$. The Burgers vector of the dislocation is parallel to the substrate surface and is located at origin O at the normalized depth, $\overline{h}_d = h_d/b$ of 20. The Poisson's ratio is $\nu = 0.3$ and the Burgers vector are taken to be of the order of lattice spacing.

The elastic field of a dislocation is completely defined by (4.8) and (4.7). If there are more than one dislocation then the resulting field can be obtained by superposing the elastic field of individual dislocation.

4.2.1 Strain Variation on the Substrate Surface

The effect of dislocation present beneath the surface of a substrate on the organization of monolayer islands deposited on the substrate is presented here. Recall that the presence of dislocation modifies the elastic field in the substrate. The elastic field of the dislocation can be obtained from (4.7) and (4.8). The strain filed along the substrate surface due to the presence of a dislocation in the substrate whose Burgers vector is parallel to the substrate surface is plotted in the Figure 4.4. As can be observed from the plot that the strain is tensile at all other locations being maximum in the vicinity of the dislocation. For the film in tension *i.e,* if the lattice spacing of the film is smaller than that of the substrate, the islands should move towards the region of the highest compressive strain or at the lowest tensile strain; in the present context at

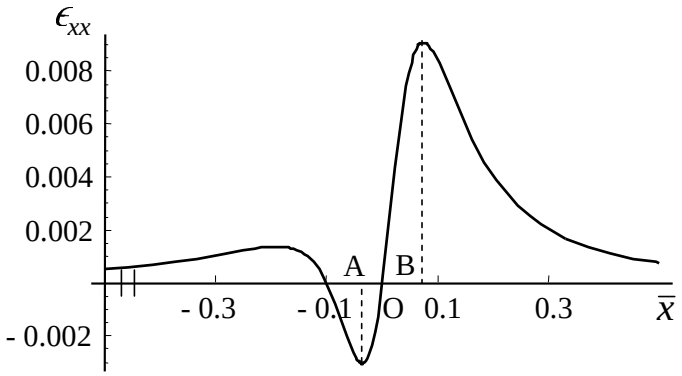

Figure 4.5: Plot of strain against the normalized distance along x-direction along the substrate surface. The Burgers vector of the dislocation is aligned at 45^0 to the substrate surface and is located at origin O at the normalized depth, $\overline{h}_d = h_d/b$ of 20. The Poisson's ratio is $\nu = 0.3$ and the Burgers vector are taken to be of the order of lattice spacing.

point O in Figure 4.4. Similarly, if the film is under compression then the islands should moves to the region of the highest tensile strain, at A and B in the Figure 4.4 and along the thickness of the substrate which is normal to the plane of the paper. For the case of an oblique dislocation *i.e,* for the dislocation whose Burgers vector is at some inclination to the substrate surface, there is only one region of maximum tensile strain as shown by point B in the strain plot of dislocation of 45° in Figure 4.5. If the film is under compression then the islands should move towards B, while for the case of the film under tension the islands should move towards A.

For the case of more than one dislocation, the resultant elastic field can be obtained by superimposing the elastic field of individual dislocation. One such case is shown in Figure 4.6 which represents the strain variation of two dislocations having Burgers vector parallel to the substrate. Here the dislocations are at C and D. The islands under compression should prefers the region intermediate of the two dislocations (at O) which is the maximum tensile region. But when the separation between the dislocations is large then the

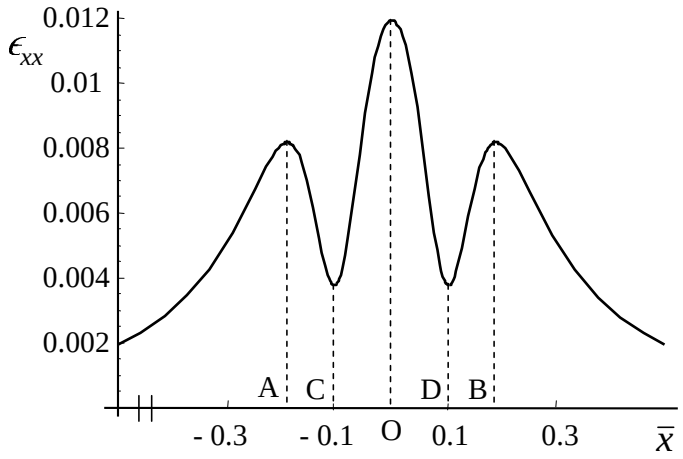

Figure 4.6: Plot of strain against the normalized distance along x-direction along the substrate surface of two dislocations. The Burgers vector of dislocations is parallel to the substrate surface and is located at C and D and at the normalized depth, $\overline{h}_d = h_d/b$ of 20. The Poisson's ratio is $\nu = 0.3$ and the Burgers vector are taken to be of the order of lattice spacing.

maximum tensile strain region shifts from O and, instead of single maximum tensile strain zone two zones of maximum tensile strain appears, as shown in the Figure 4.7. This is because the elastic field of dislocation is of short ranged *i.e,* it varies as $(x^2 + (h_d + y)^2)^{-1}$. Hence the elastic field of dislocations get affected for smaller separation between dislocations, while for larger separation the effect on the elastic field is small as can be observe by comparing Figures 4.4 and 4.7.

4.3 Influence of misfit dislocation

The evolutions of initially random configuration of islands are simulated for different configuration of the edge dislocations present beneath the substrate surface. In terms of dimensionless parameters, each of the simulations shown correspond to the case of

$$\frac{4\pi\psi G}{f_2^2(1-\nu)} = 0.408 \tag{4.9}$$

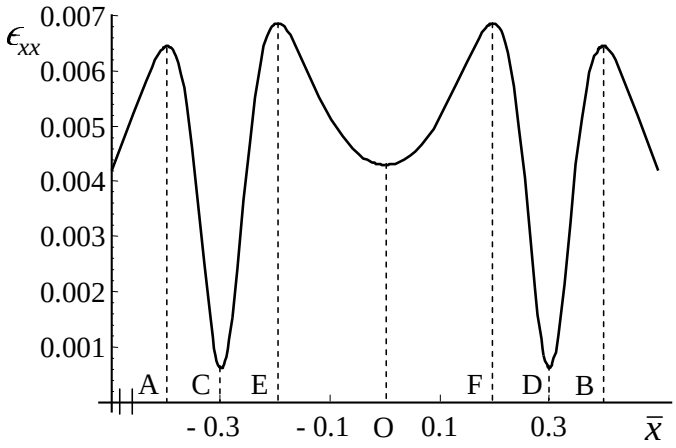

Figure 4.7: Plot of strain against the normalized distance along x-direction along the substrate surface of two dislocations located far from each other. The Burgers vector of dislocations is parallel to the substrate surface and is located at C and D and at the normalized depth, $\overline{h}_d = h_d/b$ of 20. The Poisson's ratio is $\nu = 0.3$ and the Burgers vector are taken to be of the order of lattice spacing.

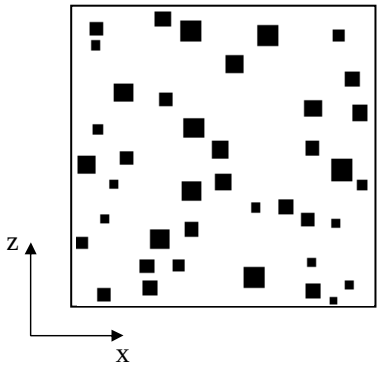

Figure 4.8: Initial random configuration of islands used to simulate the evolution under the influence of dislocation present beneath the surface of the substrate is shown.

where ψ is the step excess energy and G is the shear molulus. Other parameters are $S/h = 300$ where S is the simulation cell size and h is the island height, $a_0/h = 1/2$ where a_0 is the cut-off radius, coverage $\Theta = 0.08$, $b/h = 1/2$ where b is the Burgers vector, depth of the dislocation is $h_d = 20b$ and Poisson ratio $\nu = 0.3$. Initial sizes of the islands are in between $4h$ and $8h$. Figure 4.8 shows the initial configuration of islands. In simulation the dislocation lines are along the z-direction and the deposited film is considered to be under compression. Once islands comes at their preferred location under the influence of dislocations (*i.e,* along the z-direction), they repel each other and try to leave the simulation boundary. So the region is bounded along z-direction while in the x-direction the region remains unbounded. Figure 4.9(a) − 4.9(d) shows the snapshots of advancement of the evolution of islands when one dislocation with Burgers vector parallel to the substrate surface is present beneath the substrate surface. The line at O in each snapshot represents the dislocation line while lines A and B are same as of strain plot in Figure 4.4. As the evolution starts, some islands evaporate quickly (simulation starts with 40 islands and as observed in Figure 4.9(a) that 30 islands are left). As evolution advances the islands move towards the lines A and B (shown in Figures 4.9(b) and 4.9(c)) which are the preferred positions of islands for the present configuration of dislocation. The snapshot after considerable amount of time, Figure 4.9(d) shows arrangement of islands along the maximum tensile zone *i.e,* along A and B. Apart from the preferred positions, the islands are also observed at other places. The existence of islands at these locations are due to the balance between various forces (repulsive forces between islands and attractive force between the island and the dislocation line) acting on the islands. Figure 4.10(a) − 4.10(d) shows different stages of the evolution of islands when one dislocation with Burgers vector inclined at 45^0 to the substrate surface is present. It is found that the preferable positions for islands

are at B which is the zone of maximum tensile strain as can be observed from the Figure 4.5. Simulation results for two dislocations are presented in Figures 4.11(a) − 4.11(d) and Figures 4.12(a) − 4.12(d). In both these simulations the dislocations are located at C and D (represented by the solid lines). The dashed lines in these snapshots shows the zone of tensile strain peak of corresponding stain plot in Figure 4.6 and Figure 4.7.

It is found from these simulations that the unidirectional arrangements of the islands can readily be achieve in the presence of edge dislocation underneath the substrate. Similar results were observed by Shiryaev *et. al,* [63] for arrays of dislocation network beneath the substrate surface, shown in Figure 4.13. The epitaxial system used in their study is $Si_{1-x}Ge_x/Si$. They have found that simply by changing the dislocation morphology in the underlying substrate one can achieve remarkable rearrangements in the island patterns as illustrated in Figure 4.13. They observed the island rows aligned with the dislocation bands.

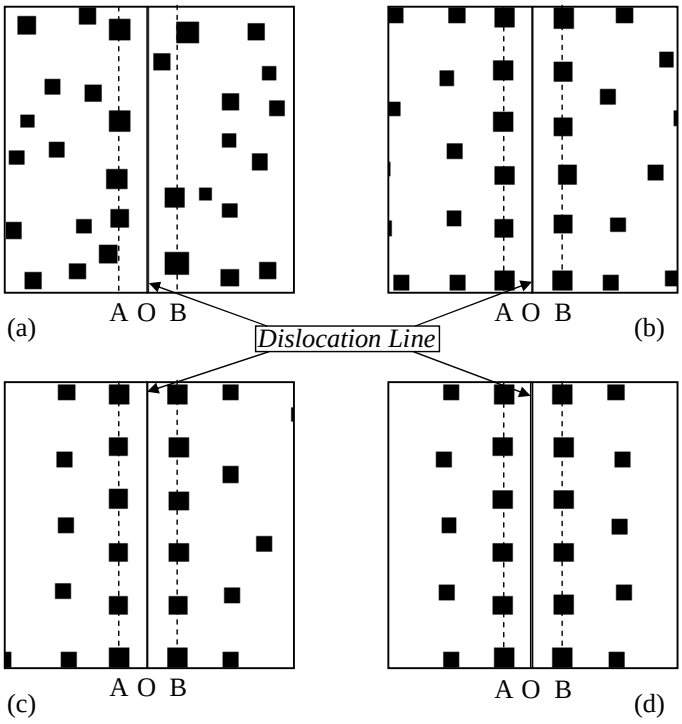

Figure 4.9: Advancement of the evolution of islands when one dislocation whose Burgers vector is parallel to the surface of the substrate is presented. The dislocation is along the line O. (a) early stage of evolution (b) and (c) is the intermediate stage and (d) evolution after considerable amount of time are shown. Lines A, O and B are same as in Figure 4.4.

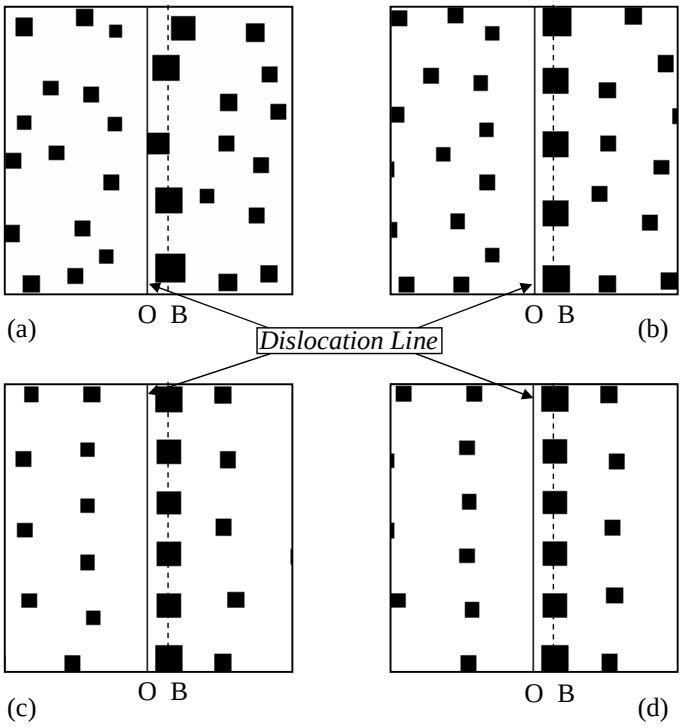

Figure 4.10: Different stage of the evolution of islands when one dislocation whose Burgers vector is inclined at 45^0 to the surface of the substrate is presented. The dislocation is along the line O. (a) early stage of evolution (b) and (c) is the intermediate stage and (d) evolution after considerable amount of time are shown. Lines O and B are same as in Figure 4.5.

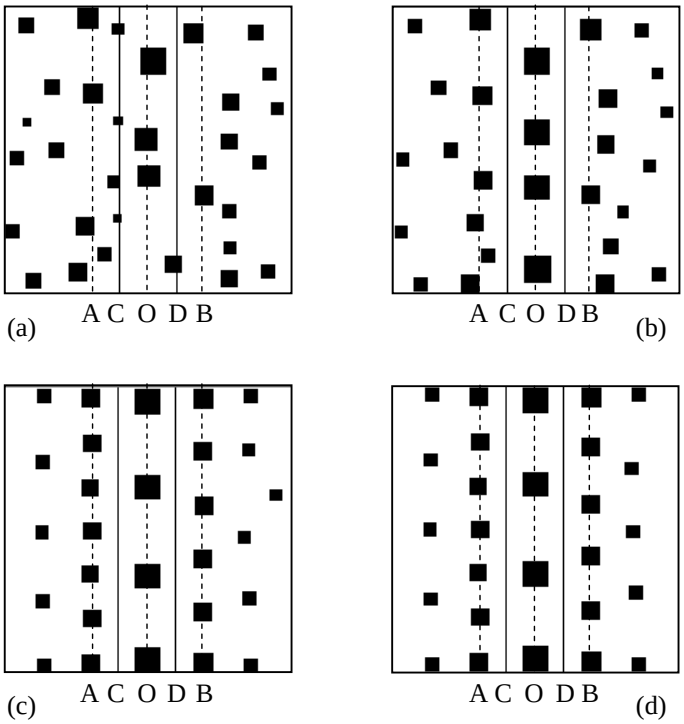

Figure 4.11: Stages of evolution when two dislocations present beneath the surface of the substrate whose Burgers vector is parallel to the substrate surface are presented here. The dislocations are along the lines C and D. The early stage of evolution (a), the intermediate stage (b) and (c) and, evolution after considerable amount of time (d) are shown here. Lines A, O and B are lines of the strain peak and are same as in Figure 4.6.

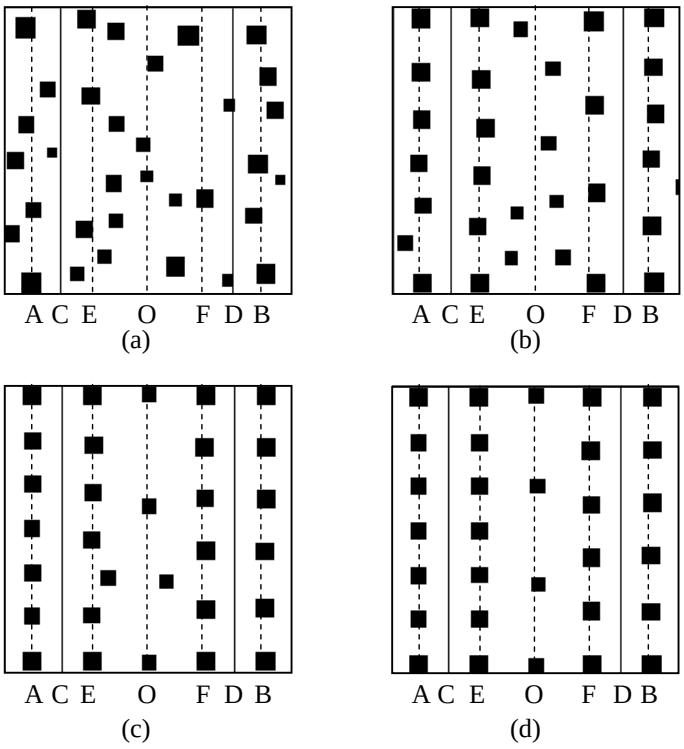

Figure 4.12: Stages of evolution when two dislocations present beneath the surface of the substrate whose Burgers vector is parallel to the substrate surface are presented here. The dislocations are along the lines C and D. The early stage of evolution (a), the intermediate stage (b) and (c) and, evolution after considerable amount of time (d) are shown here. Lines A, E, O, F and B are lines of the strain peak and are same as in Figure 4.7.

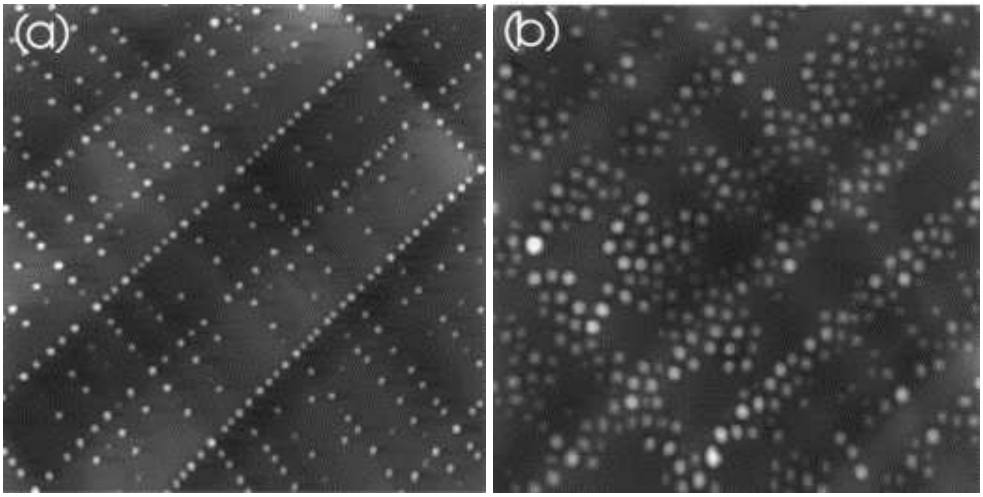

Figure 4.13: AFM images ($7.7 \times 7.7\mu m^2$) of Ge islands on the surface of dislocation pre-structured substrates obtained by Shiryaev *et, al.* [63]. The nominal thickness of the Ge overlayer is 1 nm for both images. The layer structure consists of a 2 μm thick graded layer with a Ge gradient of 1% Ge per micrometer, a top uniform $Si_{0.80}Ge_{0.20}$ layer with a 10 nm thick Si cap (a) and without the Si cap (b). The height scales (black to white) are (a) 61 nm and (b) 75 nm.

Chapter 5

Use of Selective Area Epitaxy for the Organization of Islands

Dislocations and other natural features be used to guide dot placement but site-specific control is limited. Hence organization via natural features is not suitable for most applications. The intrinsic random fluctuation in dislocation line spacing in relaxed epitaxial layers will result in a distribution of Ge islands on an irregular square grid and thus have limited accuracy in positioning. Furthermore misfit dislocations are terminated by threading dislocations which in most cases adversely affect the optical and/or electrical properties of a device structure.

The placement of islands at specific sites can be achieved by the combination of self-assembly and pre-patterning of the surface. The pre-patterning is most often done by lithography, etching and partial overgrowth of the substrate, forming trenches or holes, as well as ridges or mesas at the surface with preferential nucleation sites for dot formation [66–68]. Highly ordered arrays of Ge islands could be obtained on templates grown by a combination of pre-patterning and subsequent deposition of a strained-layer Ge_xSi_{1-x} /Si superlattice [69]. These features can be of any topography. A pattern used often in experiments is a square shaped raised pattern, or mesa. Arranging of islands by using periodic array of mesas developed on a substrate has drawn

attention experimentally [41, 46] as well as theoretically [49, 50] in past few years. These works demonstrate that islands deposited on a mesa organize at the well defined configurations (corners or center of the mesa) which depend on the geometrical and physical properties of the epitaxial system. Kitajima *et al* [46] investigated the effect of mesa size on the organization of Ge islands on a Si mesa. For large mesas Kitajima *et al* found that nucleation occurred at the mesa edges and corners, and also at random locations across the top of the substrate mesa. For smaller mesas, the edge and corner location were found to be preferred nucleation sites over other interior locations. For yet smaller mesas, only a single island was found to form on the mesa top, either centered on the mesa, or offset to one side. It is speculated that the preference of the mesa edges and corners for certain systems is due to the lateral compliance of those locations due to the reduced constraint of the substrate which allows for a reduction in strain relative to other potential nucleation sites. Also the mesa tops admit lower strain levels in general, and surface diffusion is expected to favor the relocation of deposited material from more constrained (geometrically stiff) locations of the substrate topology to the mesa top. In another study on the same system, Jin *et al* [41] found the islands to form preferentially at the four mesa corner locations. With further deposition a fifth island was found to form at the mesa center. A possible mechanism for the formation of this central island is offered by Jin *et al* as the result of islands strain field interaction which in turn alters the energy distribution on the mesa top, resulting in a shift in the relative favorability of sites within the substrate topology. Some theoretical work [49, 50], that has also been done recently, focuses on the organization of islands on the mesa but their model is two-dimensional so they may misses some feature due to three-dimensional nature of the system. This work address the organization of islands deposited on a selective region of the substrate while retaining the three-dimensional nature of the system.

The effect of the epitaxial system and the deposit amount of the film material on the stable configuration of islands is discussed. Followed by the effect of nucleation rate of islands on their stable configuration is discussed.

5.1 Effect of system's parameters on the stable configurations of islands

Consider a system with islands on a square region of a substrate. The islands may evolve, but are constrained to remain inside this region. The system evolves such that the total energy of the system is reduced. Here the evolution is governed by the elastic interaction between islands and self energy of islands. Since island repel each other, the evolution proceeds such that the separation between islands tends to increase. The system evolves until it reaches a stable equilibrium. The stable configuration of islands depends on the physical and the geometrical properties of the epitaxial system and the amount of film material deposited. Depending on these parameters the system will evolve to one of may possible stable configurations with one island, two islands, three islands or more. To understand the effect of system parameters on the stable configuration of islands, relations between system parameters and deposit amount of the film material is obtained for different stable configurations and is plotted as shown in Figure 5.1. Parameters involved in these calculations are (a) physical properties of the epitaxial system: mismatch between film and substrate material ϵ_m, Poisson ratio ν, sheer modulus G, excess energy per unit length ψ and cutoff a_0, (b) geometrical properties of the system: square region of size S and (c) deposit fraction Θ which is defined as the ratio of deposit volume to the volume of the selected region. The height of the islands are kept constant as one atomic distance. The physical and geometrical properties are combined into a single parameter $\alpha = (1-\nu)\psi/(4(1+\nu)^2 G h^2 \epsilon_m^2) - (1/\pi)\ln(S/a_0)$. The energy of the system consists of self energy and interaction energy of the is-

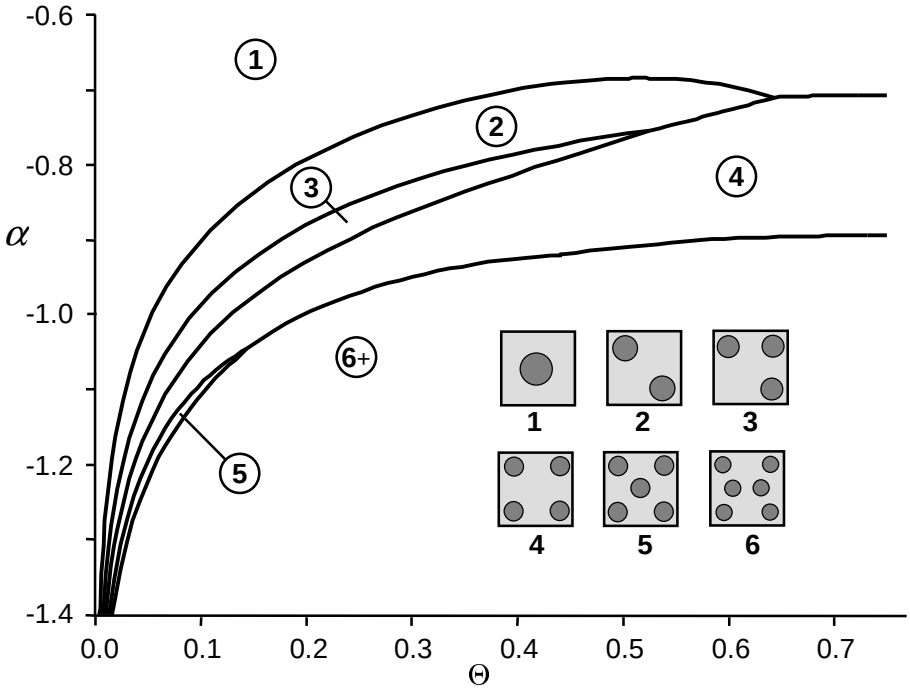

Figure 5.1: The effect of properties of an epitaxial system and deposit amount of the film material on the stable configurations is shown. Size of all islands in a particular stable configurations is considered to be the same. The α is a parameter that depends on the physical (mismatch strain ϵ_m, excess energy per unit length ψ, sheer modulus G and Poisson ratio ν) as well as geometrical properties (size of the region S) of the system, $\alpha = (1-\nu)\psi/(4(1+\nu)^2 G h^2 \epsilon_m^2) - (1/\pi)\ln(S/a_0)$. The Θ is the deposit fraction of the film material defined as the ratio of deposit volume to the volume of the selected region.

lands. To simplify the calculation, the shape of the islands are considered to be circular. The self energy of a circular island of radius R can be evaluated by following (2.42) as

$$E_{self} = \frac{2f^2R(1-\nu)}{G}\left[2 + \ln\left(\frac{a_0}{8R}\right)\right] + 2\pi R\psi \tag{5.1}$$

and the interaction energy of two circular islands of same radius R and separation distance L can be evaluated by using (2.51) as

$$E_{int} = \frac{\pi f^2 R^4(1-\nu)}{2GL^3} \tag{5.2}$$

It is observed from above equations that only the interaction energy of islands varies with the separation distance as $1/L^3$. This indicates that for a given number of islands the total energy of the system will be minimum when the interaction energy of the islands is minimum. In the case of a raise mesa the self energy of an island would also depend on position, but mesas are not considered here. Hence for a given islands density, minimum interaction energy configurations represent stable configurations. The focus is to find the dependence of stable configuration of islands on the properties of the system and the deposit amount. The analysis is done in the following manner. For a given number of islands the stable configuration and the corresponding energy is calculated. Only the configurations starting from one island up to five islands are considered in this analysis. The size of all islands in a given configuration is assumed to be the same, with radius $R = \sqrt{\Theta/(\pi n)}$, where n is the number of islands and Θ is the deposit fraction. For the case of one island, the energy of the system is independent of the position of the island. The general configuration of two islands in the region is shown in Figure 5.2(a). The corresponding interaction energy of the islands $E_{int} \propto 1/(1+m^2)^{3/2}$ is minimum at $m = 1$. This indicates that in the stable configuration the islands settle at opposite corners of the region. For three islands, shown in Figure 5.2(b), the interaction

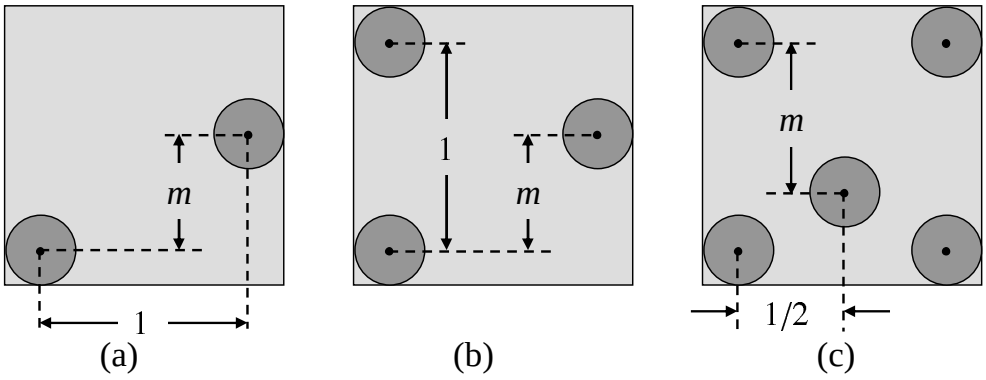

Figure 5.2: Schematic representation of two islands (a), three islands (b) and five islands (c) inside the square region of unit width. The size of all islands are same.

energy $E_{int} \propto 1 + 1/(1+m^2)^{3/2} + 1/(1+(1-m)^2)^{3/2}$ is minimum at $m = 0$ or 1 *i.e.,* the islands settle at corners of the region. The minimum energy configuration of four islands is the one in which all islands settle at the corners of the region. The interaction energy of 5 islands configuration shown in Figure 5.2(c) $E_{int} \propto 2/((1/2)^2+m^2)^{3/2} + 2/((1/2)^2+(1-m)^2)^{3/2}$. The energy of this system is minimum at $m = 1/2$ *i.e.,* four islands at corners and one at center of the region minimizes the energy of the system. After evaluating the stable configuration and the corresponding minimum energy, transition states where the minimum energy configuration changes (for example five islands to four islands, four islands to three islands and so on) are evaluated. This gives α as a function of Θ along the transition curves, which are plotted in Figure 5.1. As shown in the plot, the stable configuration depend on α as well as Θ. By controlling either α or Θ one can achieve a particular stable configuration. The α can be changed either by changing the epitaxial system (ϵ_m, ψ, G and ν) or by changing the size of the region or by changing both. It is evident from the plot that for a particular epitaxial system the number of islands in the stable configuration increases with increasing the deposit amount Θ. For a fixed deposit the number of islands increase with increasing α, which implies

an increase in ψ or S or a decrease in ϵ_m. Consider for example Ge_xSi_{1-x}/Si where the lattice mismatch varies from $\epsilon_m = 0\%$ to -4% as the Ge fraction x varies from 0 to 1. Step excess energies are on the order of 0.1 eV/atom [57,58], or $\psi \sim (0.1/a_0)$ eV where a_0 is the lattice spacing. Taking this value for ψ, $a_0 = 5.65$ Å, shear modulus $G = 40$ GPa, Poisson ratio $\nu = 0.3$, step height $h = a_0/2$, force monopole $f = 2h\epsilon_m G(1+\nu)/(1-\nu)$, mismatch $\epsilon_m = 4\%$ and size of the region $S/a_0 = 200$ the α is calculated as -1.11. For this system, before $\Theta = 0.036$ the stable configuration consists of only one island. On increasing Θ up to 0.10, island density increases from one island to five islands in the stable configuration. After $\Theta = 0.10$ the stable configuration consists of 6 or more islands. It is also evident from the plot that for $\alpha > -1.05$ and $\Theta > 0.135$ configuration of five islands is not favorable and on reducing Θ below 0.135 at $\alpha = -1.05$ or increasing α beyond -1.05 at $\Theta = 0.135$, from six or more islands configuration one can observe four islands configuration. Also, for $\Theta < 0.52$ and $\alpha > -0.75$ configuration of three islands is not favorable. Similarly, for $\Theta < 0.64$ and $\alpha > -0.71$ configuration of two islands is not favorable.

The above calculation is done on the basis of equilibrium without regard to kinetics. These configurations can be achieved if the system does not evolve to one of many possible metastable states. In experiment, many islands are nucleated over the region and as time proceeds some islands disappear due to coarsening. It is likely that the complex kinetic evolution from an initially random state will produce a metastable configuration. In order to understand the behavior of such system dynamic analysis has been done and discussed in the next section.

5.2 Evolution of islands during epitaxy on a selective area

Evolution of multiple islands on a selective area of the substrate is considered in this section. Islands are deposited randomly at periodic intervals on the area. The initial diameter of a deposited island is taken to be 5 atomic spacings which is roughly the size of a stable nucleus. The systems are annealed, such that evolution occurs under the constraint of fixed mass of all islands. The islands are constrained to remain inside the selected area. This is done by adjusting the driving force on an island lying at boundary such that it will not cross the boundary. Simulations were carried out until equilibrium was achieved. Results are presented as: (a) the epitaxial system and the deposit amount varies while the size of the region is fixed, shown in Figure 5.3 and 5.6 to 5.9, and (b) the deposit amount and the size of the region varies while α is fixed, shown in Figure 5.10. These results are discussed below.

Effect of deposit amount on the stable configuration of islands:

The effect of deposit amount and epitaxial system on the stable configuration of the islands for fixed size of the region is presented. In Figure 5.3 the size of the region is $S/a_0 = 200$ and the Poisson ratio is 0.3, and the simulations start from a fixed amount of deposited material. The simulations were carried out for deposit fractions ranging from 0.04 to 0.34. In the initial random configuration, islands are separated by at least one atomic distance. The initial random configuration with deposit fraction $\Theta > 0.34$ is difficult to achieve because the entire region becomes populated with islands. For a given Θ the simulations are done by changing α such that the desired configuration of islands (from 5 islands to 1 island) is achieved. It is observed that the resulting configuration differs on different runs for the same parameters. For example, lets consider a system with $\alpha = -0.85$ and the deposit amount $\Theta = 0.10$. The system equili-

brates to 5 or 6 islands depending on the initial random state (see Figure 5.3). This behavior indicates that the system is evolving to different metastable configurations. The plot of Figure 5.3 is obtained by performing 5 to 6 sets of simulations for the same parameters, and from the resulting configurations the configuration is chosen which has maximum number of occurrences. Each dot represents a result of the simulation. Diamonds represents the 5-island configuration, unfilled square represents 4-island, triangle represents 3-island, unfilled circle represents 2-island and filled square represents 1-island configurations. In the resulting configurations, islands located symmetrically are of the same diameter. This means in the 3-island configuration islands located at the opposite corners are of same diameter while the third island is smaller than the other two islands. Similarly, in 5-island configuration all 4 islands at the corners are of same diameter while the islands sitting at the center is smaller than remaining four islands. It is evident from Figure 5.3 that for a fixed system the island density increases with increasing the deposit amount. For a fixed deposit amount the islands density increases with decreasing α. This behavior is similar to the one observed in the plot of minimum energy configurations, Figure 5.1. For a given system and deposit amount the plot of Figure 5.3 gives a higher island density than the minimum energy state (Figure 5.1). To illustrate that the kinetically determined configurations are in fact metastable, consider an epitaxial system with $\alpha = -0.86$. For such system it can be observed from the Figure 5.3 that for $\Theta = 0.10$ the resulting configuration consists of 5 islands. The normalized energy $\overline{E} = EG/(f^2(1-\nu))$ of this system for different configurations is plotted as shown in Figure 5.4. The energy is calculated by changing the size of the islands for configurations from 5-island to 1-island. In 5-island configuration the size of the center island is changed by transferring equal mass to/from all corner islands; the size of the corner islands remain equal. In the 4-island configuration mass is transferred

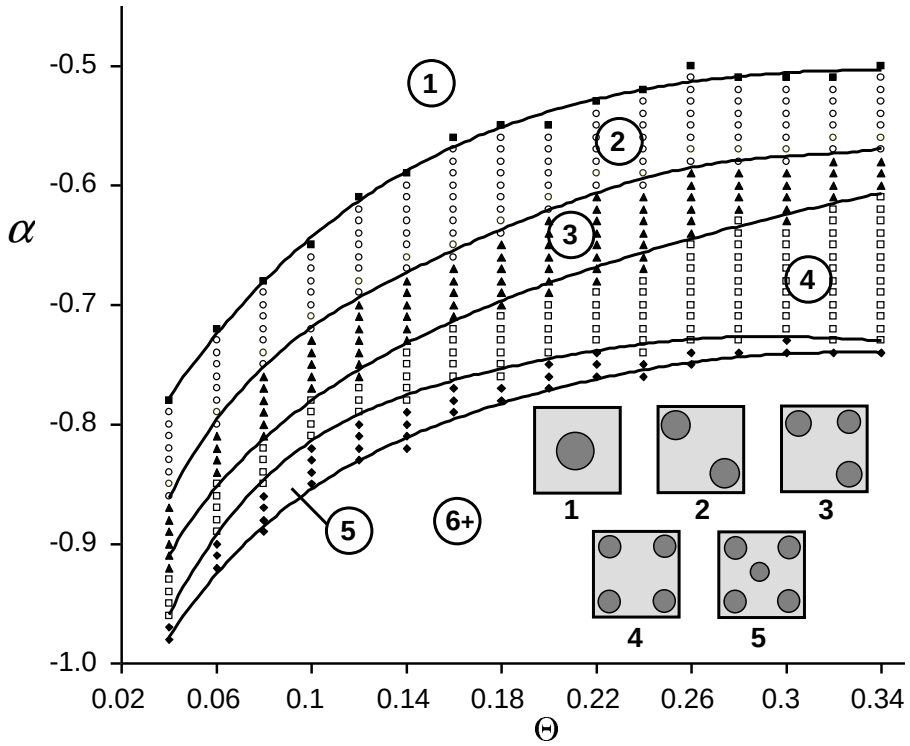

Figure 5.3: Effect of the deposit amount Θ and the properties of the epitaxial system α on the stable configuration of islands is presented. The size of the region is fixed as $S/a_0 = 200$, size of all islands is same as 5 atomic distance, height of the islands is taken as 1 atomic distance the deposition rate of islands is infinite and Poisson ratio $\nu = 0.3$.

from one corner island to the others, in the 3-island configuration mass is transferred from the asymmetric island to the others and in 2-island configuration it is transferred from one island to the other. Energies along these transition paths are plotted in Figure 5.5. The plot shows that the energy increases with either increasing or decreasing the size of the island, which indicates that each of these states are metastable. The minimum energy configuration for this system is that of a single island configuration, as shown in Figure 5.1.

To probe the relationship between deposition rate and the most likely metastable state, instead of depositing all islands together and letting them evolve (which mimics very fast deposition rate followed by an anneal), the

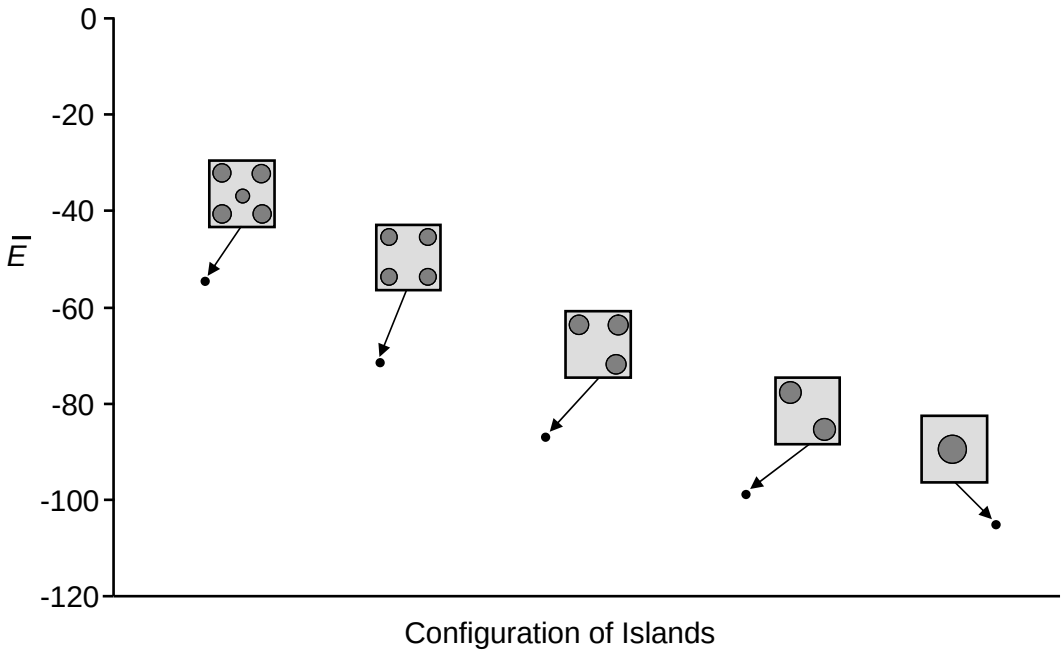

Figure 5.4: The energy of the system form 5-island to 1-island configuration is shown for $\alpha = -0.86$, $\nu = 0.3$ and $S/a_0 = 200$, deposit fraction $\Theta = 0.10$. The energy changes by changing the configuration and in particular it decreases by reducing the island density.

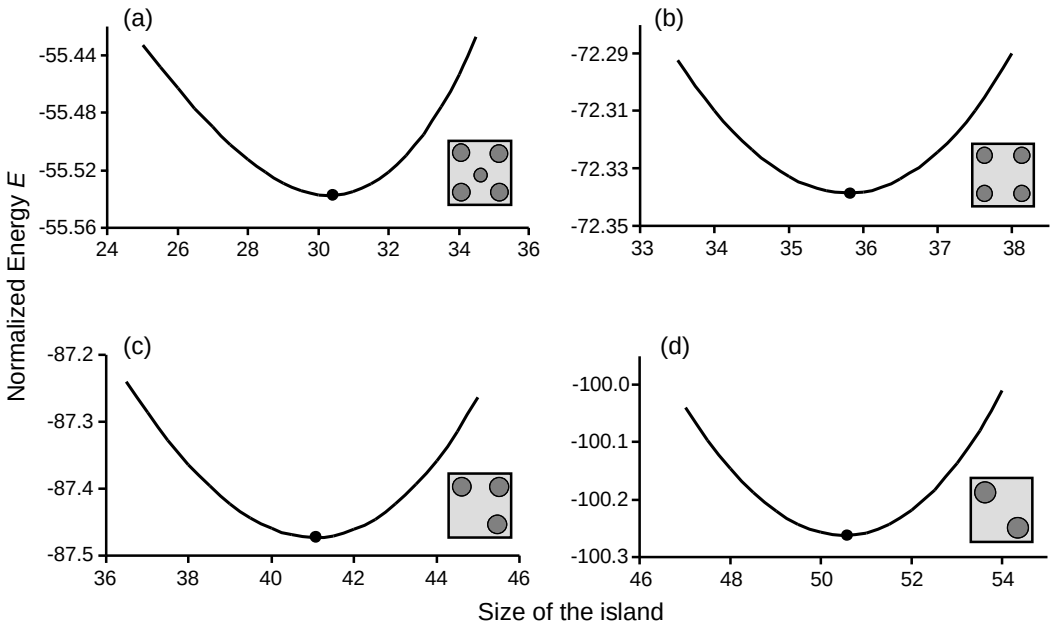

Figure 5.5: The variation of energy of the system of Figure 5.4 by changing the size of the islands is shown. In 5-island configuration (a) the size of the center island is changed by transferring equal mass from all corner islands. At any instant the size of all corner islands is same. In 4-island configuration (b) bottom left corner island, in 3-island configuration (c) the island located at top right corner and in 2-island configuration (d) bottom right corner island is picked. The energy increases with either increasing or decreasing the size of the island.

islands are now deposited at various rates. Simulations start from 1 island of diameter 5 atomic spacings. Subsequent islands are randomly deposited at a regular intervals until the required amount of deposit is achieved. The system is then annealed to equilibrium. The results are shown in Figures 5.6 to 5.9 for different deposition rates of the islands. The size of the area is fixed at $S/a_0 = 200$ and the Poisson ratio is 0.3. From Figure 5.6 through 5.9 the deposition rate is progressively slower. The deposition rates of Figures 5.7, 5.8 and 5.9 are respectively 0.5, 0.3 and 0.27 times that of Figure 5.6. The trend of island density on the epitaxial system and deposit amount is same as observed for minimum energy configurations (Figure 5.1) and in the case of infinite deposition rate (Figure 5.3), *i.e.,* the islands density increases either by increasing Θ for fixed α or by decreasing α for fixed Θ. Quantitatively, the results of the fastest deposition rate (Figure 5.6) are most similar to the result for minimum energy configurations (Figure 5.1). Nevertheless, marked differences are apparent and it is likely that any similarities are nothing but coincidence. As deposition rate is decreased from Figures 5.6 to 5.8, the number of islands in the final stable configuration decreases for a given system. The reason for this is clear considering that large islands tend to grow at the expense of smaller islands and the small islands of similar size are subject to coarsening according to Eqn (3.5). Consider a very slow deposition rate. Early in the growth, two critical nuclei of similar size lie on the substrate. If their size is less than the critical size required to resist coarsening (Eqn 3.5), mass will be transferred from one island to the other. If the deposition rate is slow enough compared to the rate of mass transfer, this process results in a single larger island before a third island is nucleated. The third island will then be absorbed into the larger island before a fourth nucleates and so on until the result is a single large island. Faster deposition rates suppress this effect resulting in two or more islands of size greater than the critical size to

resist coarsening. While multiple islands of similar size may have lower free energy, there is an activation barrier that must be overcome in order for a single large island to break up on the smaller ones. Hence the results should contain an explicit temperature dependence in addition the implicit one related to the ratio of mass transfer rate to deposition rate. The activation barrier has not been estimated and hence the current simulations do allow this process to occur. Additional work will be necessary to understand this effect on the assembly process.

Effect of area size on the stable configuration of islands:

According to the minimum energy analysis (Figure 5.1), the effect of selective area size S is completely contained in the parameter α. In the above results, obtained via kinetic simulation, the area size was fixed, which implies that α characterizes the epitaxial system, and not necessarily the area size. It is likely that for the kinetic case the effect of size $\overline{S} = S/a_0$ is not completely contained in the parameter α. This is because the results ought also to depend on the size of the initial nuclei as compared to $\overline{S}$. To test this likelihood, the area size $\overline{S} = S/a_0$ is varied for fixed α; the result is shown in Figure 5.10. The deposition rate is same as that in Figure 5.9 and $\alpha = -1.11$. It is evident from these plots that the effect of $\overline{S}$ is not completely contained within α in the kinetic case. In order to test that the reason is the size of the critical nuclei relative to S, a similar plot would be needed, but holding the ratio r_{nuc}/S fixed where r_{nuc} is the nuclei size. Furthermore, as S is contained in α, the plot of Figure 5.10 can not be used to understand the effect of S on the resulting configurations. To obtain such an understanding, plots of $\psi/Gh^2\epsilon^2$ versus Θ are needed.

This investigation shows that by the use of selective area epitaxy it is possible to obtain well defined islands configuration. It is shown that the mate-

rial properties, deposit amount, the size of the region and deposition rate plays an important role in the arrangement of islands. By the proper selection of these parameters it is possible to achieve a range of islands configuration. The devices in microelectronic and optoelectronic applications requires a uniform and regular arrangement of quantum dot at specific locations. The selective area epitaxy may have potential application in the manufacturing of these devices.

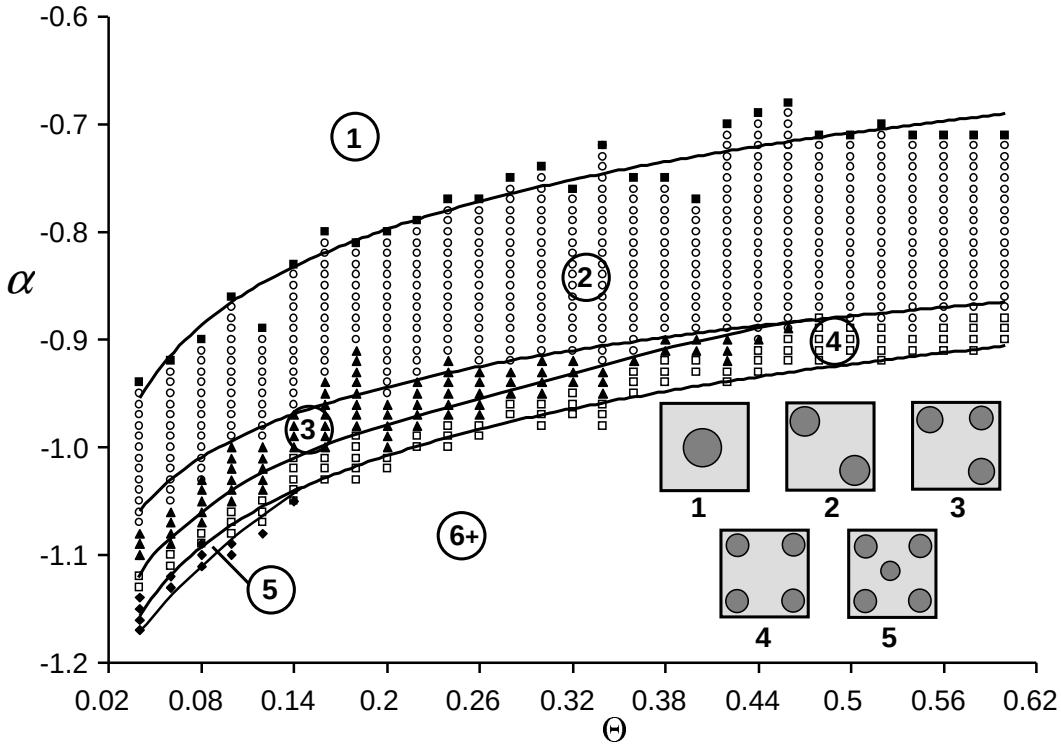

Figure 5.6: Effect of the deposit amount Θ and the properties of the epitaxial system α on the stable configuration of islands is presented. The size of the region is fixed as $S/a_0 = 200$, height of the islands is taken as 1 atomic distance and Poisson ratio $\nu = 0.3$. A deposition rate is introduced in these simulations. Size of all deposited islands is same as 5 atomic distance. Simulation starts with 1 island then after some interval second island is deposited at a random location inside the region. After the same interval another island is deposited and this process of deposition continues until the desired deposit amount is achieved.

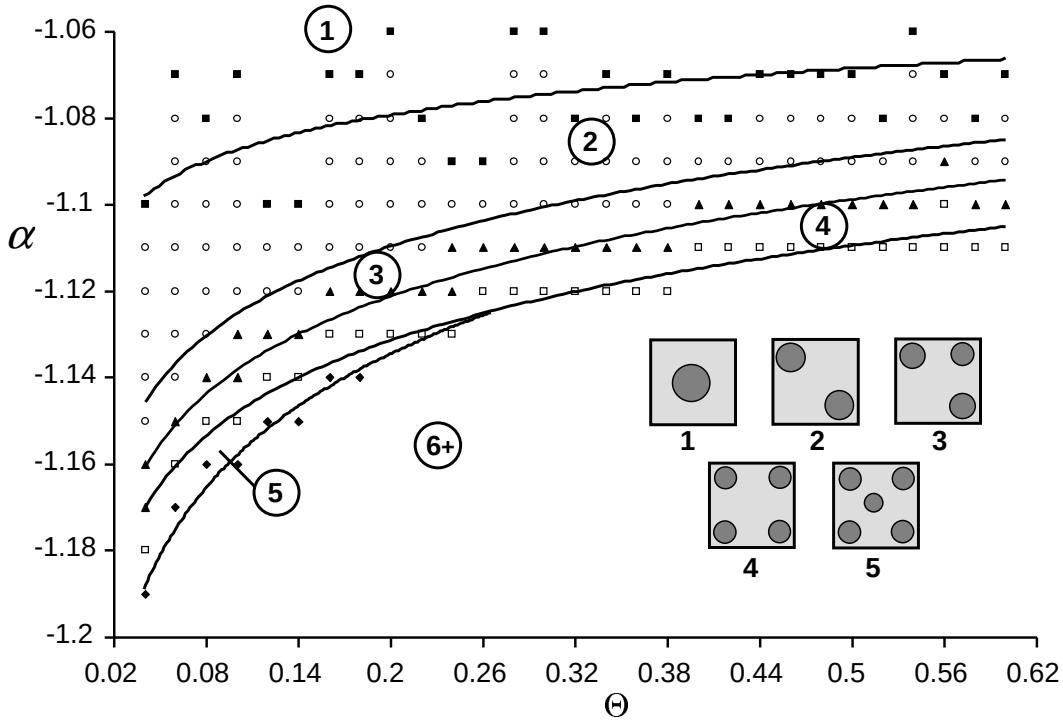

Figure 5.7: Plot illustrate the dependence of the stable configuration on the deposit amount Θ and the properties of the epitaxial system α. The size of the region is fixed as $S/a_0 = 200$, height of the islands is taken as 1 atomic distance and Poisson ratio $\nu = 0.3$. An intermediate deposition rate (0.5 times than that in Figure 5.6) is chosen.

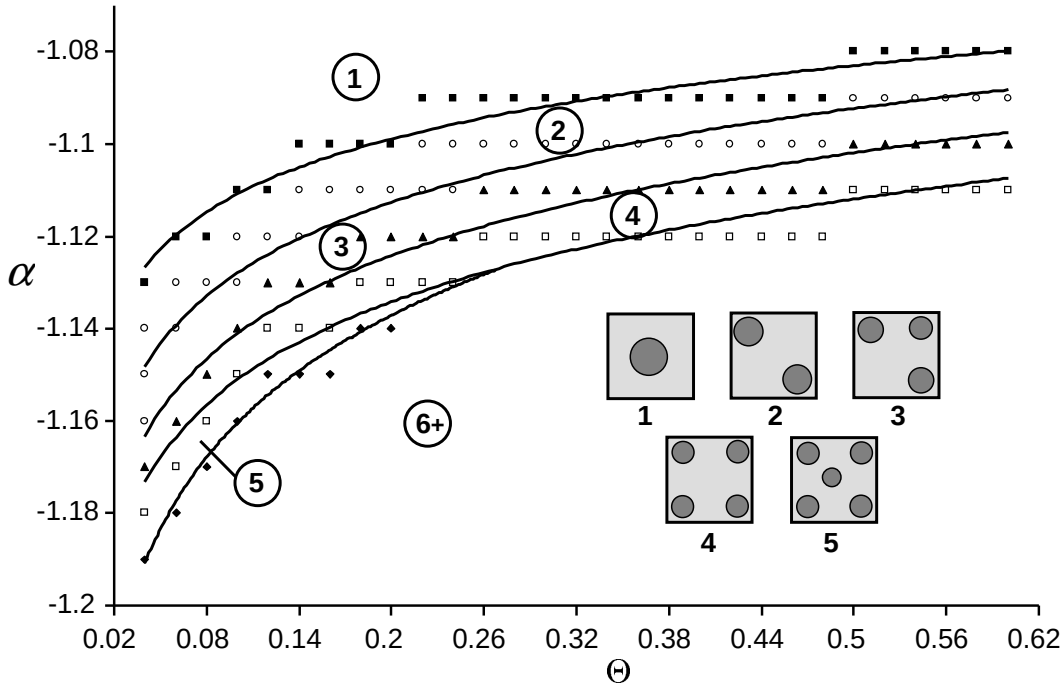

Figure 5.8: The effect of the deposit amount Θ and the properties of the epitaxial system α on the stable configuration of islands is illustrated. The deposition rate of the islands is considered to be slow (0.3 times than that in Figure 5.6). The size of the region is fixed as $S/a_0 = 200$, height of the islands is taken as 1 atomic distance and Poisson ratio $\nu = 0.3$.

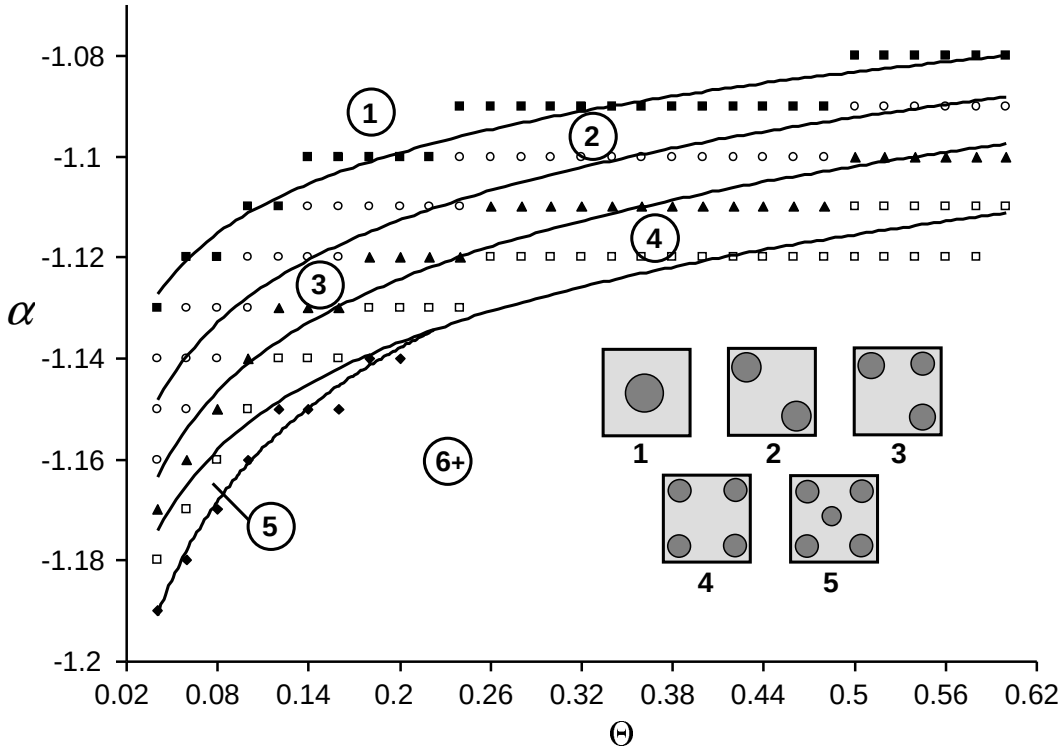

Figure 5.9: The dependence of stable configuration of islands on the deposit amount Θ and the properties of the epitaxial system α is illustrated. The deposition rate of the islands is considered to be slow (0.27 times than that in Figure 5.6). The size of the region is fixed as $S/a_0 = 200$, height of the islands is taken as 1 atomic distance and Poisson ratio $\nu = 0.3$.

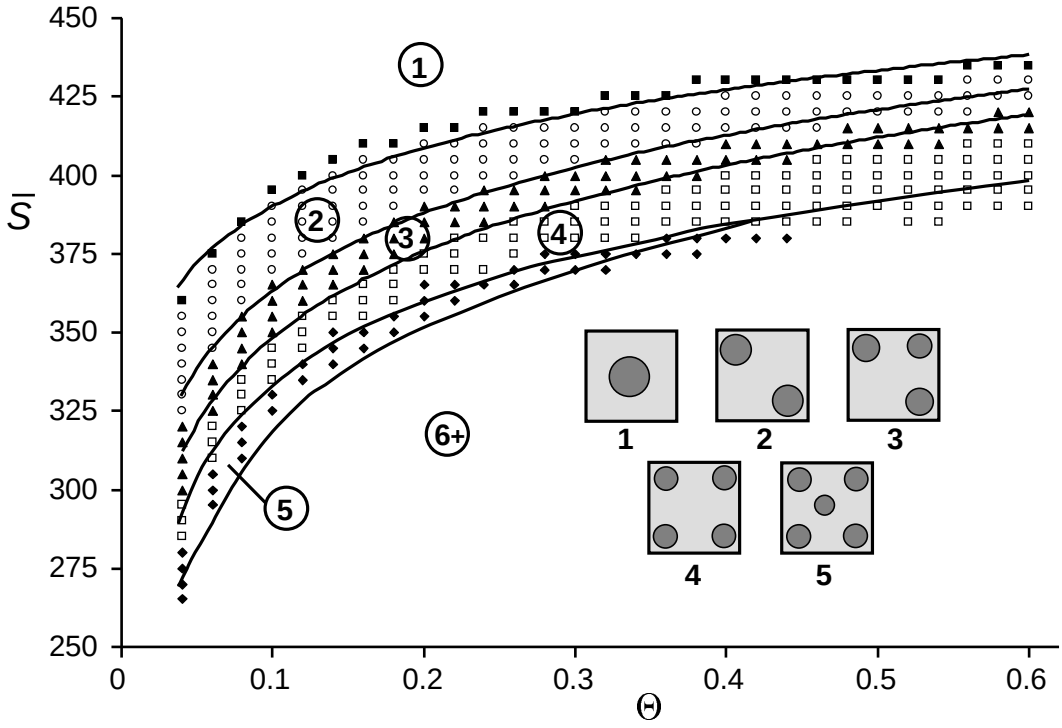

Figure 5.10: The dependence of stable configuration on the deposit amount Θ and size of the region $\overline{S} = S/a_0$ on the stable configuration is illustrated. The height of the islands is taken as 1 atomic distance, $\alpha = -1.11$ and Poisson ratio $\nu = 0.3$. The deposition rate is slow which is same as in Figure 5.9.

Chapter 6

Conclusion

The self-organization of strained epitaxial islands deposited on a substrate is discussed in this work. Arrangements of islands by using anisotropy in surface stress and/or in lattice mismatch, by introducing dislocation into the substrate and by using selective area epitaxy are considered. First, a model is developed for the evolution by condensation/evaporation of islands. Followed by elastic interaction of an island with itself and with other islands is presented. It is shown that the elastic energy of islands introduce a mechanism that stabilizes the islands from coarsening and helps them to achieve a uniform array. For the isotropic case their is no preferred orientation so islands repel each other. This results in hexagonal domains that meet at grain-boundary-like defects. In order to reduce these defects anisotropy is introduced. Anisotropy introduces an orientational preference and changes the repulsion into attraction at certain orientations. It was shown that anisotropy can reduce the occurrence of defects relative to the isotropic case. Simulation results demonstrate that the anisotropy, which may be tailored though choice of the epitaxial system and the application of an remote load, plays an important role in the self-organization, and the stability of epitaxial islands. By the proper selection of these parameters it is possible to achieve a range of anisotropies which could lead to a variety of arrangements. Both for small levels of anisotropy (Fig-

ure 3.6b) and large levels of anisotropy (Figures 3.6e and 3.6f), islands tend *not* to self-organize into regular patterns, but into metastable states characterized by a high defect density. The best case for self-organization is a modest level anisotropy (Figure 3.6c). Long-ranged self-organization is enhanced by both the repulsion between islands and tendency for islands to align in a particular direction. Small anisotropies provide the required repulsion but not a strong enough tendency for islands to align in particular directions. Large anisotropies provide the necessary strength for alignment but cause islands to attract.

Controlled positioning of islands can be achieved by naturally forming defects and other sources of residual strain. The example of organization in the vicinity of subsurface lattice dislocations was simulated. It was shown that the resulting configuration of islands is directly related to the strain field on the substrate surface. Locations where islands preferentially form depends on the nature of the mismatch between the islands and the substrate. If an island must be compressed (stretched) onto the surface in order to achieve epitaxy, it will preferentially form at locations of low residual compressive (tensile) strain or more favorably at location of high residual tensile (compressive) strains. Such locations reduce an island's chemical potential and thus reduce the total free energy over less favorable sites.

Selective area epitaxy was also considered as a method to control the arrangement of islands. Here the configuration of islands depends on various parameters such as the epitaxial system, amount of deposited material and, size of the region. The configurations of interest were those of a single island in the region, 2 islands at corners of the region, 3 islands at the corners, 4 islands at the corners, and 5 islands–4 at corners and 1 at the center. It was shown that by changing the epitaxial system, deposit amount or the size of the region it is possible to achieve each of the different configurations. For a fixed epitaxial

system and size of the region, it is found that on increasing the deposit amount the density of islands in stable configuration increases. Also for a fixed deposit amount and the epitaxial system, the density of islands increases by decreasing the size of the region. It was found that kinetics play an important role in the stable configuration of islands and that the resulting configuration is likely to be metastable. Deposition rate was found to have a strong effect on the resulting stable configuration of islands. Temperature effects were implicitly contained in the relative rates of mass transfer to deposition. However, as metastable state configurations were found to be common, additional effects should be included in order to completely characterize the self-organization process. Primarily, a temperature dependent mechanism must be included, by which a single island can separate into two smaller islands. This can be done by determining the activation energy for the process and a stochastic model for the event to occur.

APPENDIX

Green's function for an elastic half-space (Cerrutti's problem)

The expression for the Green's function $G_{ij}(\mathbf{x}, \mathbf{y})$ can be expressed as:

$$
\begin{aligned}
G_{ij} &= \frac{\delta_{ij}}{r_p} + \frac{(3-4\nu)\delta_{ij}}{r_m} + \frac{4(1-\nu)(1-2\nu)\delta_{ij}}{r_p + x_3 + y_3} + \frac{2x_3 y_3 \delta_{ij}}{r_p^3} \\
&\quad + \frac{r_i r_j}{r_m^3} + \frac{r_i r_j (3-4\nu)}{r_p^3} - \frac{6 r_i r_j x_3 y_3}{r_p^5} - \frac{4 r_i r_j (1-\nu)(1-2\nu)}{r_p (r_p + x_3 + y_3)^2} \\
G_{13} &= \frac{r_1 (x_3 - y_3)}{r_m^3} + \frac{r_1 (3-4\nu)(x_3 - y_3)}{r_p^3} + \frac{6 r_1 x_3 y_3 (x_3 + y_3)}{r_p^5} \\
&\quad - \frac{4 r_1 (1-\nu)(1-2\nu)}{r_p (r_p + x_3 + y_3)} \\
G_{23} &= \frac{r_2 (x_3 - y_3)}{r_m^3} + \frac{r_2 (3-4\nu)(x_3 - y_3)}{r_p^3} + \frac{6 r_2 x_3 y_3 (x_3 + y_3)}{r_p^5} \\
&\quad - \frac{4 r_2 (1-\nu)(1-2\nu)}{r_p (r_p + x_3 + y_3)} \\
G_{31} &= \frac{r_1 (x_3 - y_3)}{r_m^3} + \frac{r_1 (3-4\nu)(x_3 - y_3)}{r_p^3} - \frac{6 r_1 x_3 y_3 (x_3 + y_3)}{r_p^5} \\
&\quad + \frac{4 r_1 (1-\nu)(1-2\nu)}{r_p (r_p + x_3 + y_3)} \\
G_{32} &= \frac{r_2 (x_3 - y_3)}{r_m^3} + \frac{r_2 (3-4\nu)(x_3 - y_3)}{r_p^3} - \frac{6 r_2 x_3 y_3 (x_3 + y_3)}{r_p^5} \\
&\quad + \frac{4 r_2 (1-\nu)(1-2\nu)}{r_p (r_p + x_3 + y_3)} \\
G_{33} &= \frac{(x_3 - y_3)^2}{r_m^3} + \frac{(3-4\nu)x_3^2 + 4(1-2\nu)x_3 y_3 + (3-4\nu)y_3^2}{r_p^3} \\
&\quad + \frac{6 x_3 y_3 (x_3 + y_3)^2}{r_p^5} + \frac{3-4\nu}{r_m} + \frac{5 + 4\nu(-3+2\nu)}{r_p}
\end{aligned}
\tag{A-1}
$$

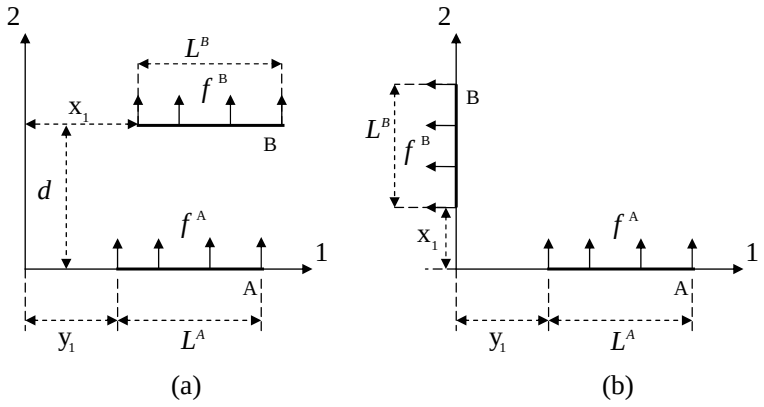

Figure A-1: Two types of step orientations with respect to each other are shown. Steps A and B of lengths L^A and L^B, and force distribution of f^A and f^B are oriented (a) parallel to each other, and (b) perpendicular to each other.

where i and $j = 1, 2$ and $r_1 = x_1 - y_1$, $r_2 = x_2 - y_2$, $r_m = \sqrt{r_1^2 + r_2^2 + (x_3 - y_3)^2)}$ and $r_p = \sqrt{r_1^2 + r_2^2 + (x_3 + y_3)^2}$.

Interaction energies of steps

Self-interaction of an island is calculated as the sum of the self-energies of individual steps of the island and the interaction energy between steps of the island. Energy of interaction of steps aligned parallel to each other, shown schematically in Figure A-1(a), can be calculated by using (2.41). Here two parallel steps A and B are considered, shown in Figure A-1(a). The steps are located at y_1 and x_1 from the axis-2 with separation d between them. The sizes of steps are L^A and L^B. The complete expression for their interaction

energy is

$$E_{int}^{AB}\big(x_1, y_1, d, L^A, L^B, f^A, f^B\big) = \frac{f^A\, f^B}{4\,\pi\, G}\Bigg[(1-2\,\nu)\Big\{\sqrt{d^2+(L^A-k)^2} - \sqrt{d^2+k^2} + \sqrt{d^2+(L^B+k)^2} + \sqrt{d^2+(L^A-L^B-k)^2}\Big\} + (1-\nu)\Big\{(L^A-k)\,\ln\big(-L^A+k+\sqrt{d^2+(L^A-k)^2}\,\big) - (L^A-L^B-k)\,\ln\big(-L^A+L^B+k+\sqrt{d^2+(L^A-L^B-k)^2}\,\big) - (L^B+k)\,\ln\big(L^B+k+\sqrt{d^2+(L^B+k)^2}\,\big) + k\,\ln\big(k+\sqrt{d^2+k^2}\,\big)\Big\}\Bigg] \tag{A-2}$$

where $k = x_1 - y_1$, f^A and f^B are the distributed forces acting on respective steps, ν is poisson's ratio, and G is modulus of rigidity of the material. Correspondingly, the interaction between steps aligned orthogonal to each other, shown in Figure A-1(b), can also be evaluated by using (2.41) as

$$E_{int}^{AB}\big(x_1, y_1, L^A, L^B, f^A, f^B\big) = \frac{f^A\, f^B\,\nu}{4\,\pi\, G}\Bigg[\sqrt{x_1^2+y_1^2} - \sqrt{(L^B+x_1)^2+y_1^2} - \sqrt{x_1^2+(L^A+y_1)^2} + \sqrt{(L^B+x_1)^2+(L^A+y_1)^2}\Bigg] \tag{A-3}$$

Besides the interaction with other steps, step also interacts with its own elastic-field. Energy of self-interaction of a step of length L^A and having distributed force f^A can be calculated by using (2.42) as

$$E_{self}^{A}\big(L^A, f^A\big) = L^A\,\psi + \frac{L^A\,\big(f^A - 2\,f^A\,\nu\big)\Big(2\,f^A + f^A\,\ln\Big(\frac{a_0^2}{4\,(L^A)^2}\Big)\Big)}{4\,\pi\, G} \tag{A-4}$$

where a_0 is the cut-off of the order of surface lattice constant and ψ is the excess energy per unit length of the step.

Bibliography

[1] S. Y. Chou, P. R. Krauss, and L. Kong. Nanolithographically defined magnetic structures and quantum magnetic disk. *J. Appl. Phys.*, 79(8):6101, 1996.

[2] U. Drodofsky, J. Stuhler, T. Schulze, M. Drewsen, B. Brezger, T. Pafu, and J. Mlynek. Hexagonal nanostructures generated by light masks for neutral atoms. *Appl. Phys. B*, 65(6):755, 1997.

[3] R. L. Kubena, F. P. Stratton, J. W. Ward, G. M. Atkinson, and R. J. Joyce. Sub-20-nm-wide line fabrication in poly(methylmethacrylate) using a ga+ microprobe. *J. Vac. Sci. Technol. B*, 7(6):1798, 1989.

[4] P. P. Nguyen, D. H. Pearson, R. J. Tonucci, and K. J. Babcock. Fabrication and characterization of uniform metallic nanostructures using nanochannel glass. *J. Electrochem. Soc.*, 145(1):247, 1998.

[5] S. Y. Chou, P. R. Krauss, and P. J. Renstrom. Imprint of sub-25 nm vias and trenches in polymers. *Appl. Phys. Lett.*, 67(21):3114, 1995.

[6] S. Y. Chou and P. R. Krauss. Imprint lithography with sub-10 nm feature size and high throughput. *Microelectronic Engg.*, 35(1-4):237, 1997.

[7] A. D. Kent, D. M. Shaw, S. V. Molnar, and D. D. Awschalom. Growth of high-aspect-ratio nanometer-scale magnets with chemical-vapor-

deposition and scanning-tunneling-microscopy. *Science*, 262(1537):1249, 1993.

[8] D. J. Eaglesham and M. Cerullo. Dislocation-free stranski-krastanow growth of ge on si(100). *Phys. Rev. Lett.*, 64(16):1943, 1990.

[9] M. Zinke-Allmang, L. C. Feldman, S. Nakahare, and B. A. Davidson. Growth mechanism and clustering phenomena: The ge-on-si system. *Phys. Rev. B*, 39(11):7848, 1989.

[10] Y.-W. Mo, D. E. Savage, B. S. Swartzentruber, and M. G. Lagally. Kinetic pathway in stranski-krastanov growth of ge on si(001). *Phys. Rev. Lett.*, 65(8):1020, 1990.

[11] M. Krishnamurthy, J. S. Drucker, and J. A. Venables. Microstructural evolution during the heteroepitaxy of ge on vicinal si(100). *J. Appl. Phys.*, 69(9):6461, 1991.

[12] D. Leonard, K. Pond, and P. M. Petroff. Critical layer thickness for self-assembled inas islands on gaas. *Phys. Rev. B*, 50(16):11687, 1994.

[13] T. I. Kamins, E. C. Carr, R. S. Williams, and S. J. Rosner. Deposition of three-dimensional ge islands on si(001) by chemical vapor deposition at atmospheric and reduced pressures. *J. Appl. Phys.*, 81(1):211, 1997.

[14] J. A. Floro, E. Chason, M. B. Sinclair, L. B. Freund, and G. A. Lucadamo. Dynamic self-organization of strained islands during sige epitaxial growth. *Appl. Phys. Lett.*, 73(7):951, 1998.

[15] F. M. Ross, J. Tersoff, and R. M. Tromp. Coarsening of self-assembled ge quantum dots on si(001). *Phys. Rev. Lett.*, 80(5):984, 1998.

[16] J. A. Floro, M. B. Sinclair, E. Chason, L. B. Freund, R. D. Twesten, R. Q. Hwang, and G. A. Lucadamo. Novel sige island coarsening kinetics: Ostwald ripening and elastic interactions. *Phys. Rev. Lett.*, 84(4):701, 2000.

[17] V. A. Shchukin, N. N. Ledentsov, P. S. Kop'ev, and D. Bimberg. Spontaneous ordering of arrays of coherent strained islands. *Phys. Rev. Lett.*, 75(16):2968, 1995.

[18] Feng Liu, Adam H. Li, and M. G. Lagally. Self-assembly of two-dimensional islands via strain-mediated coarsening. *Phys. Rev. Lett.*, 87(12):126103–1, 2001.

[19] R. Plass, J. A. Last, N. C. Bartelt, and G. L. Kellogg. Nanostructures self-assembled domain patterns. *Nature*, 412:875, 2001.

[20] Y. F. Gao, W. Lu, and Z. Suo. A mesophase transition in a binary monolayer on a solid surface. *Acta Materialia*, 50(9):2297, 2002.

[21] Y. W. Zhang. Self-organization, shape transition, and stability of epitaxially strained islands. *Phys. Rev. B*, 61(15):10388, 2000.

[22] P. Liu, Y. W. Zhang, and C. Lu. Computer simulations of the stranski-krastanov growth of heteroepitaxial films with elastic anisotropy. *Surf. Sc.*, 526(3):375, 2003.

[23] P. Liu, Y. W. Zhang, and C. Lu. Formation of self-assembled heteroepitaxial islands in elastically anisotropic films. *Phys. Rev. B*, 67(16):165414–1, 2003.

[24] J. J. Eggleston and P. W. Voorhees. Ordered growth of nanocrystals via a morphological instability. *Appl. Phys. Lett.*, 80(2):306, 2002.

[25] G. Capellini M. DeSeta and F. Evangelisti. Ordered growth of ge island clusters on strain-engineered si surfaces. *Phys. Rev. B*, 71(11):115308–1, 2005.

[26] S. Kiravittaya, H. Heidemeyer, and O. G. Schmidt. Lateral quantum-dot replication in three-dimensional quantum-dot crystals. *Appl. Phys. Lett.*, 86(26):263113–1, 2005.

[27] S. Wise, J. Lowengrub, J. Kim, and W. Johnson. Efficient phase-field simulation of quantum dot formation in a strained heteroepitaxial film. *Superlattices Microstruct*, 36(1-3):293, 2004.

[28] D. D. Chambliss, R. J. Wilson, and S. Chiang. Nucleation of ordered ni island arrays on au(111) by surface-lattice dislocations. *Phys. Rev. Lett*, 66(13):1721, 1991.

[29] S.Y. Shiryaev, F. Jensen, J. L. Hansen, J. W. Petersen, and A. N. Larsen. Nanoscale structuring by misfit dislocations in $si_{1-x}ge{-}x/si$ epitaxial systems. *Phys. Rev. Lett*, 78(3):503, 1997.

[30] Bert Voigtl˙ Ordered growth of ge islands above a misfit dislocation network in a ge layer on si(111).

[31] Y.H. Xie, S.B. Samavedam, M. Bulsara, T.A. Langdo, and E.A. Fitzgerald. Relaxed template for fabricating regularly distributed quantum dot arrays. *Appl. Phys. Lett.*, 71(24):3567, 1997.

[32] J.W. Matthews, S. Mader, and T. B. Light. Accommodation of misfit across interface tebween crystals of semiconducting elements or compounds. *J. Appl. Phys.*, 41(9):3800, 1970.

[33] J.W. Matthews, A. E. Blakeslee, and S. Mader. Use of misfit strain to remove dislocations from epitaxial thin films. *Thin Solid Films*, 33(2):253, 1976.

[34] L. B. Freund. The mechanics of dislocations in strained-layer semiconductor materials. *Adv. Appl. Mech.*, 30:1, 1994.

[35] P. Politi, G. Grenet, A. Marty, A. Ponchet, and J. Villain. Instabilities in crystal growth by atomic or molecular beams. *Phys. Rep.*, 324(5-6):271, 2000.

[36] Q. Xie, A. Madhukar, P. Chen, and N. P. Kobayashi. Vertically self-organized inas quantum box islands on gaas(100). *Phys. Rev. Lett.*, 75(13):2542, 1995.

[37] J. Tersoff, C. Teichert, and M. G. Lagally. Self-organization in growth of quantum dot superlattices. *Phys. Rev. Lett.*, 76(10):1675, 1996.

[38] G. Capellini, M. De Seta, F. Evangelisti, V. A. Zinovyev, G. Vastola, F. Montalenti, and Leo Miglio. Self-ordering of a ge island single layer induced by si overgrowth. *Phys. Rev. Lett.*, 96(10):106102–1, 2006.

[39] J. H. Lee, Zh. M. Wang, B. L. Liang, W. T. Black, Vas P. Kunets, Yu I. Mazur, and G. J. Salamo. Selective growth of ingaas/gaas quantum dot chains on pre-patterned gaas(100). *Nanotechnology*, 17(9):2275, 2006.

[40] T. I. Kamins, R. Stanley Williams, and D. P. Basile. Self-aligning of self-assembled ge islands on si(001). *Nanotechnology*, 10(2):117, 1999.

[41] G. Jin, J. L. Liu, S. G. Thomas, Y. H. Luo, K. L. Wang, and B. Y. Nguyen. Controlledawq arrangement of self-organized ge islands on patterned si (001) substrates. *Appl. Phys. Lett*, 75(18):2752, 1999.

[42] L. Vescan and T. Stoica. Luminescence of laterally ordered ge islands along ¡100¿ directions. *J. Appl. Phys.*, 91(12):10119, 2002.

[43] R. Leon, S. Chaparro, S. R. Johnson, C. Navarro, X. Jin, Y. H. Zhang, J. Siegert, S. Marcinkevicius, X. Z. Liao, and J. Zou. Dislocation-induced spatial ordering of inas quantum dots: Effects on optical properties. *J. Appl. Phys.*, 91(9):5826, 2002.

[44] J. Brault, S. Tanaka, E. Sarigiannidou, J.L. Rouviere, B. Daudin, G. Feuillet, and H. Nakagawa. Linear alignment of gan quantum dots on aln grown on vicinal sic substrates. *J. Appl. Phys.*, 93(5):3108, 2003.

[45] S. L. Silva and F. M. Leibsle. Room temperature quantum corrals. *Surface Science*, 441(1):L904, 1999.

[46] T. Kitajima, B. Liu, and S. R. Leone. Two-dimensional periodic alignment of self-assembled ge islands on patterned si(001) surfaces. *Appl. Phys. Lett*, 80(3):497, 2002.

[47] J. L. Gray, R. Hull, and J. A. Floro. Control of surface morphology through variation of growth rate in sige/si(100) epitaxial films: Nucleation of quantum fortresses. *Appl. Phys. Lett.*, 81(13):2445, 2002.

[48] R. Songmuang, S. Kiravittaya, and O. G. Schmidt. Formation of lateral quantum dot molecules around self-assembled nanoholes. *Appl. Phys. Lett.*, 82(17):2892, 2003.

[49] R. V. Kukta and D. Kouris. On the mechanisms of epitaxial island alignment on patterned substrates. *J. Appl. Phys.*, 97(3):033527–1, 2005.

[50] N. D. Machtay and R. V. Kukta. Energetics of epitaxial island arrangements on substrate mesas. *J. Appl. Mech.*, 73(2):212, 2006.

[51] O. L. Alerhand, D. Vanderbilt, R.D. Meade, and J. D. Joannopoulos. Spontaneous formation of stress domains on crystal surfaces. *Phys. Rev. Lett.*, 61(17):1973, 1988.

[52] J. Tersoff. Step energies and roughening of strained layers. *Phys. Rev. Lett.*, 74(24):4926, 1995.

[53] J. Tersoff, Y. H. Phang, Z. Zhang, and M. G. Lagally. Step bunching instability of vicinal surfaces under stress. *Phys. Rev. Lett.*, 75(14):2730, 1995.

[54] R. V. Kukta and K. Bhattacharya. A micromechanical model of surface steps. *J. Mech. Phys. Solids*, 50(3):615, 2002.

[55] V. I. Marchenko and A. Ya. Parshin. On the elastic properties of crystal-surfaces. *Sov. Phys. JEPT*, 52(1):129, 1980.

[56] L. M. Brown. Self-stress of dislocations + shape of extended nodes. *Phil. Mag.*, 10(105):441, 1964.

[57] J. Kollar, L. Vitos, B. Johansson, and H. L. Skriver. Metal surfaces: Surface, step and kink formation energies. *Phys. Stat. Sol. (B)*, 217(1):405, 2000.

[58] V. B. Shenoy, C. V. Ciobanu, and L. B. Freund. Strain induced stabilization of stepped si and ge surfaces near (001). *Appl. Phys. Lett.*, 81(2):364, 2002.

[59] A. Li, F. Liu, and M. G. Legally. Equilibrium shape of two-dimensional islands under stress. *Phys. Rev. Lett.*, 85(9):1922, 2000.

[60] T. Mano, R. Nötzel, D. Zhou, G. J. Hamhuis, T. J. Eijkemans, and J. H. Wolter. Complex quantum dot arrays formed by combination of self-

organized anisotropic strain engineering and step engineering on shallow patterned substrates. *Journal of Applied Physics*, 97(1):014304, 2005.

[61] M. Hupalo and M. C. Tringides. Self-organization and geometry control of pb islands grown on anisotropic substrates. *Physical Review B (Condensed Matter and Materials Physics)*, 73(4):041405, 2006.

[62] Zh. M. Wang, H. Churchill, C. E. George, and G. J. Salamo. High anisotropy of lateral alignment in multilayered (in,ga)as/gaas(100) quantum dot structures. *Journal of Applied Physics*, 96(11):6908, 2004.

[63] S. Y. Shiryaev, E. V. Pedersen, F. Jensen, J. W. Petersen, J. L. Hansen, and A. N. Larsen. Dislocation patterning – a new tool for spatial manipulation of ge islands. *Thin Solid Films*, 294(1-2):311, 1997.

[64] L. B. Freund. The mechanics of dislocation in strained-layer semiconductor materials. *Adv. Appl. Mech.*, 30:1, 1994.

[65] N. I. Muskhelishvili. Leyden : Noordhoff International, fourth edition, 1975.

[66] M. Borgström, V. Zela, and W. Seifert. Arrays of ge islands on si(001) grown by means of electron-beam pre-patterning. *Nanotechnology*, 14(2):264, 2003.

[67] Eun Soo Kim, Noritaka Usami, and Yasuhiro Shiraki. Selective epitaxial growth of dot structures on patterned si substrates by gas source molecular beam epitaxy. *Semiconductor Science and Technology*, 14(3):257, 1999.

[68] G. Jin, J. L. Liu, and K. L. Wang. Regimented placement of self-assembled ge dots on selectively grown si mesas. *Applied Physics Letters*, 76(24):3591, 2000.

[69] O. G. Schmidt, N. Y. Jin-Phillipp, C. Lange, U. Denker, K. Eberl, R. Schreiner, H. Grabeldinger, and H. Schweizer. Long-range ordered lines of self-assembled ge islands on a flat si (001) surface. *Applied Physics Letters*, 77(25):4139, 2000.